MECHANICAL PROPERTIES OF REPAIRED CARBON FIBER REINFORCED POLYMER COMPOSITES

A THESIS SUBMITTED TO
THE GRADUATE SCHOOL OF NATURAL AND APPLIED SCIENCES
OF
MIDDLE EAST TECHNICAL UNIVERSITY

BY

E. EVREN SONAT

IN PARTIAL FULFILLMENT OF THE REQUIREMENTS
FOR
THE DEGREE OF DOCTOR OF PHILOSOPHY
IN
MECHANICAL ENGINEERING

DECEMBER 2021

Approval of the thesis:

MECHANICAL PROPERTIES OF REPAIRED CARBON FIBER REINFORCED POLYMER COMPOSITES

submitted by **E. EVREN SONAT** in partial fulfillment of the requirements for the degree of **Doctor of Philosophy** in **Mechanical Engineering**, **Middle East Technical University** by,

Prof. Dr. Halil Kalıpçılar
Dean, Graduate School of **Natural and Applied Sciences** _____

Prof. Dr. M. A. Sahir Arıkan
Head of the Department, **Mechanical Engineering** _____

Assoc. Prof. Dr. Sezer Özerinç
Supervisor, **Mechanical Engineering, METU** _____

Examining Committee Members:

Assoc. Prof. Dr. Merve Erdal
Mechanical Engineering, METU _____

Assoc. Prof. Dr. Sezer Özerinç
Mechanical Engineering, METU _____

Prof. Dr. C. Hakan Gür
Metallurgical and Materials Engineering, METU _____

Assoc. Prof. Dr. Burcu Saner Okan
Integrated Manufacturing Research and Application Center, SU _____

Asst. Prof. Dr. Mete Bakır
Mechanical Engineering, AYBU _____

Date: 10.12.2021

I hereby declare that all information in this document has been obtained and presented in accordance with academic rules and ethical conduct. I also declare that, as required by these rules and conduct, I have fully cited and referenced all material and results that are not original to this work.

Name Last name : E.Evren Sonat

Signature :

ABSTRACT

MECHANICAL PROPERTIES OF REPAIRED CARBON FIBER REINFORCED POLYMER COMPOSITES

Sonat, E.Evren
Doctor of Philosophy, Mechanical Engineering
Supervisor: Assoc.Prof. Dr. Sezer Özerinç

December 2021, 150 pages

Carbon fiber reinforced polymer (CFRP) composites are increasingly used in the aerospace industry due to their high specific strength compared to conventional metallic materials. However, a significant shortcoming of these composites is their increased susceptibility to damage. Structural repair is a common method to restore the load-carrying capacity of a damaged part when the damage size exceeds the pre-defined tolerances. Scarf and stepped bonded repair methods are the primary choice for cases that require high strength recovery and aerodynamic smoothness. So, there is an increasing need to understand the mechanical performance of the repaired zone.

This thesis study investigated the mechanical performance of flush repairs, emphasizing industrial practices and applications. The experimental part of the study quantified the effect of scarf angle on the strength of 2D joints and also determined the strength recovery rates for prepreg and wet lay-up repairs. In addition, the temperature and moisture effect on the repairs have been investigated through the testing of conditioned specimens.

The results show that a small scarf angle has a strong positive influence on the strength of the repaired zone. When the scarf angle is 1.9°, the recovery rate reaches 88.6 % of the intact specimens. In addition, temperature and moisture can adversely affect the strength of the repair, especially in the case of a wet lay-up. An evaluation of the porosity content in the repair area through microscopy and ultrasonic inspection has been performed.

Numerical modeling of the 2D scarf joints and 3D repairs through finite element modeling complemented the experimental results and provided further insight into the failure modes. The model employed the built-in Cohesive Zone Method (CZM) of ABAQUS, and the Hashin failure theorem was implemented through a specially developed script. Fracture toughness tests performed on the adhesives provided accurate modeling of the adhesive response under loading. The simulation results closely predict the experimental behavior both in terms of failure strength and failure modes. Then the verified model was used to predict the effect of porosity on the joint strength of 2D scarf joints as well as the impact of strength and toughness of the adhesive on the repair strength.

The thesis developed a systematic approach to the experimental and numerical analysis of composite repairs. The results provided a deeper understanding of repair zones' mechanical behavior and offered a framework for future study of different CFRP composites and their structure-property relationships.

Keywords: Carbon fiber reinforced polymers, Composites, Bonded joints, Composite repair, Mechanical testing

ÖZ

TAMİR EDİLMİŞ KARBON FİBER TAKVİYELİ POLİMER KOMPOZİTLERİN MEKANİK ÖZELLİKLERİ

Sonat, E.Evren
Doktora, Makina Mühendisliği
Tez Yöneticisi: Assoc.Prof. Dr. Sezer Özerinç

Aralık 2021, 150 sayfa

Karbon fiber takviyeli polimer (CFRP) kompozitler, geleneksel metalik malzemelere kıyasla yüksek özgül mukavemetleri nedeniyle havacılık endüstrisinde giderek daha fazla kullanım alanına sahip olmaktadır. Bir çok avantajının yanı sıra, kompozit malzemelerin en büyük eksikliklerinden biri de hasara karşı dayanımlarının düşük olmasıdır. Kullanım sırasında hasar oluşumu kaçınılmazdır ve hasar boyutu, önceden tanımlanmış hasar limitlerini aştığı takdirde parçanın yük taşıma kapasitesini eski haline getirmek için yapısal onarımlara ihtiyaç duyulur. Bu nedenle, uçak kompozit bileşenlerinin ömrünü uzatmak için etkili tamir teknikleri geliştirmek kaçınılmazdır. Açılı ve kademeli yapıştırma tamir yöntemleri, yüksek mukavemet geri kazanımı ve aerodinamik gereksinimlerin kaçınılmaz olduğu yerlerde,birincil tercih olarak kullanılırlar. Tamir edilen bölgenin mekanik performansının iyi anlaşılmasına ihtiyaç vardır.

Bu tez kapsamında, endüstride uygulanan malzemeler ve yöntemlerle yapılan açılı ve basamaklı yapıştırma tamir metotları incelenmiştir. Bu kapsamda; tamir açısının etkisi 2-D bağlantılarda incelenmiş ve küçük açıların tamir mukavemetine pozitif bir etkisi olduğu saptanmıştır. Açının 1.9° seçildiği durumda, tamir mukavemeti sağlam

numunenin mukavemetinin % 88.6'sına ulaştığı görüşmüştür. Prepreg veya oda sıcaklığında kürlenen ıslak serim malzeme kullanımının yarattığı yapısal dayanım farkı deneysel olarak incelenmiştir. Ayrıca, bu tamirlerin ısıya ve neme karşı dayanıklıkları da incelenmiştir. Sonuç olarak, her 2 tamir yöntemi ile de yüksek dayanım elde edilebileceği fakat oda sıcaklığı tamirlerinin sıcaklık ve nem karşısında dayanımını kaybettiği saptanmıştır. Son olarak, tamir bölgesindeki gözenek oluşumu ultrasonik muayene ve mikroskobik kesit incelemesi yöntemleriyle incelenmiş ve bu yöntemler arasında bir korelasyon çalışması yapılmıştır.

Deneysel çalışmaların yanı sıra, 2 boyutlu açılı birleştirmeler ve 3 boyutlu tamirler hem kompozit parça için hem de yapıştırma bölgesi için sürekli hasar analizi yapılarak numerik olarak modellenmiştir. Kompozit hasar analizi için, Hashin teoremi, yazılan kod yardımıyla ABAQUS programına entegre edilmiştir. Yapıştırma analizi için ise program içeriğinde bulunan kohesiv elemanlar metodu kullanılmıştır. Kohesiv metodu için, gerekli olan yapıştırıcı parametreleri için ayrıca kırılım testleri yapılmış olup modellemelerde de bu veriler kullanılmıştır.

Yapılan çalışma sonucunda, kompozit tamirlerin deneysel ve sayısal analizine sistematik bir yaklaşım geliştirilmiştir. Sonuçlar hem onarım bölgelerinin mekanik davranışının daha derinden anlaşılmasını sağlamış hem de farklı CFRP kompozitlerinin ve bunların yapı-özellik ilişkilerinin gelecekteki analizi için bir altyapı sunmuştur.

Anahtar Kelimeler: Karbon fiber takviyeli polimer, Kompozit, Yapıştırma bağlantılar, Kompozit tamir, Mekanik test

To my family,

ACKNOWLEDGMENTS

First and foremost, I am extremely grateful to my supervisor, Assoc. Prof. Dr. Sezer Özerinç for allowing me to pursue this Ph.D. research. He believed in me from the beginning to the end. His guidance, advice, criticism, and insight throughout the research were terrific.

This research is sponsored by Turkish Aerospace Industry. The support provided by Turkish Aerospace Industry is gratefully acknowledged. I would like to thank Turkish Aerospace "Materials Engineering" and "Composite Repair" departments for their invaluable support during the experimental study.

I also wish to thank all my family for their invaluable support, especially uncle Aral Ege, who believed in me and encouraged me to start this study.

Last but not least, I wish to thank my husband Ferhat and my daughter Irmak for their love, endless support, and encouragement, which greatly helped me finish this work.

TABLE OF CONTENTS

ABSTRACT v

ÖZ vii

ACKNOWLEDGMENTS x

TABLE OF CONTENTS xi

LIST OF TABLES xiv

LIST OF FIGURES xv

CHAPTERS

1 INTRODUCTION 1

1.1 Overview 1

1.2 Bonded Repair of CFRP laminates 4

1.3 Bonded Repair Analysis of CFRP Laminates 8

1.3.1 Failure Analysis for the Composite Adherends 9

1.3.2 Failure Analysis of the Bonded Joints 21

1.4 Repair Parameters of Scarfed Repairs 32

1.4.1 Scarf Angle 32

1.4.2 Surface Treatment 33

1.4.3 Adherend Thickness and Lay-up 36

1.4.4 Effect of Extra Layer 37

1.4.5 Adhesive Properties 38

1.4.6 Cure Processes 40

1.5 Nondestructive Inspection of Repairs 40

1.6 Certification of Repairs 42

1.7 Objectives and Layout of the Thesis 43

2 FAILURE BEHAVIOR OF SCARF-BONDED WOVEN FABRIC CFRP LAMINATES 45
2.1 Introduction 45
2.2 Experimental Details 46
2.3 Experimental Results and Discussion 49
2.4 Modeling Methodology 55
2.4.1 Failure and Damage Progression of the Laminate 56
2.4.2 Failure and Damage Progression of the Adhesive 59
2.5 Modeling Results and Discussion 60
2.6 Defect Evaluation 66
2.7 Conclusions 69
3 FAILURE BEHAVIOR OF ON-SITE REPAIRED WOVEN FABRIC COMPOSITES 71
3.1 Introduction 71
3.2 Experimental Details 71
3.3 Experimental Results and Discussion 77
3.4 Modeling Methodology 85
3.5 Modeling Results and Discussion 88
3.6 Conclusions 97
4 DURABILITY OF REPAIRED WOVEN FABRIC COMPOSITES 99
4.1 Introduction 99
4.2 Experimental Details 100
4.3 Experimental Results and Discussion 102
4.4 Defect Evaluation 105

4.5 Conclusion 111
5 CONCLUSIONS AND FUTURE WORK 113
REFERENCES 119
APPENDICES
A. DCB and ENF Testing 137
B. USDFLD Code 144
C. Selective Test Results 146
D. Prepreg and Wet lay-up Repair Steps 147
CURRICULUM VITAE

LIST OF TABLES

TABLES

Table 2.1. Mechanical properties of the M21/AS4C composite provided by the manufacturer [163]. 47
Table 2.2. Mechanical properties of the FM-300K adhesive [166] 49
Table 2.3. Tensile testing results of the intact and scarf-bonded specimens. 50
Table 2.4.Degradation parameters for the progressive failure of the composite structure. 59
Table 3.1. Mechanical properties of Hexforce G0904 plain weave dry carbon fabric impregnated with HYSOL EA 9396 adhesive, with a 1/3 weight ratio [128]. 74
Table 3.2. Mechanical properties of the HYSOL EA 9396 [173,174] adhesive. 75
Table 3.3. Summary of the tensile testing results. 79
Table 4.1. Test matrix to evaluate the effect of moisture and temperature. 101
Table 4.2 Summary of the tensile testing results for the conditioned and untreated versions of the repaired specimens. 103
Table 4.3. Results of the ultrasonic inspection, microscopic porosity evaluation, and mechanical testing. 110

LIST OF FIGURES

FIGURES

Figure 1.1. Typical repair methods. (a) Single lap repair, (b) Double lap repair, (c) Stepped repair, (d) Scarf repair. Red lines represent the film adhesive for the prepreg repairs. 5
Figure 1.2. Fracture envelope for Puck's IFF failure modes. Figure taken from ref. [13]. 15
Figure 1.3. Comparison of different failure criteria with the WWFE test results. Figure taken from ref. [15] 17
Figure 1.4. Types of ply discount methods in composite laminates. Figure taken from ref. [36]. 19
Figure 1.5. (a) Volkersen model with elastic adherends, (b) Distribution of the shear stress distribution over the bonded area. Figure taken from ref. [56]. 22
Figure 1.6. (a) Goland and Reissner model with elastic adherends. (b) Distribution of the shear stress distribution over the bonded area. Figure taken from ref. [56]. 23
Figure 1.7. Failure modes in adhesive joints. 26
Figure 1.8. Damage progression schematic in an adhesively bonded joint. Figure taken from ref. [83]. 27
Figure 1.9. Graphical representation of the bilinear traction-separation behavior used for the modeling of the adhesive. Figure taken from ref.[35]. 28
Figure 1.10. (a) Peel stress distribution in the adhesive (b) Shear stress distribution in the adhesive. Figure taken from ref. [92]. 34
Figure 1.11. (a) Fiber fracture and fiber pull-out in the composite adherends bonded with 0.5° scarf angle (b) Cohesive failure of the adhesive for a scarf angle of 2.9°. Figure taken from ref. [106]. 35
Figure 1.12. Shear strength distribution of the single lap joints with respect to the sanding direction. Figure taken from ref. [117]. 36
Figure 1.13. Failure stress distribution for a scarf joint with respect to different laser treatments, SC representing solvent cleaned specimen as the reference, each LP

representing different infrared laser treatment parameters. Figure taken from ref. [121]. 37
Figure 1.14. The effect of the number of extra plies on the repair strength. Figure taken from ref. [128]..... 38
Figure 1.15. Influence of overlap dimension of the extra ply for adherend thicknesses of 3.5 mm and 7 mm. Figure taken from ref. [127]..... 38
Figure 1.16. Normalized peak peel and shear stress in the adhesive bond-line (ta: adhesive thickness ranging from 0.13 mm to 0.39 mm; tp: ply thickness 0.13 mm). Figure taken from ref. [105]. 39
Figure 2.1. A schematic of the test specimens. Thickness and scarf angle are exaggerated for clarity. Dimensions are in mm..... 48
Figure 2.2. Load-displacement curves of the intact and scarf-bonded specimens. Inset shows the data for all 2.8° specimens, demonstrating the good repeatability of the tests. The inset has the same axes and units as the main plot. 50
Figure 2.3. Photographs and SEM views of the fracture surfaces of representative test specimens. (a) Cohesive failure of a 5.7° specimen. (b) Cohesive failure + intra-laminar failure of a 2.8° specimen with detail showing the fiber breakages in 0° and 45° fibers (c) pull out fracture of a 1.9° specimen with detail showing the fiber breakages in 0° and 45° fibers. 52
Figure 2.4. Optical microscope side view of a 5.7° specimen. 55
Figure 2.5. (a) Schematic description of the finite element model. (b) Close-up view of the mesh structure around the scarf. 57
Figure 2.6. Experimental and numerical load-displacement curves for the specimens with three different scarf angles. The experimental displacement measurements correspond to the extensometer data. 61
Figure 2.7. Failure load values for intact and scarf specimens, as determined by experiments and as predicted by simulations. 62
Figure 2.8.Schematic describing the definitions of the stress components and the coordinate frame. (b) Normalized shear stress distribution. (c) Normalized peel stress

distribution. (d) Shear stress concentration distribution. (e) Peel stress concentration distribution. 64
Figure 2.9. Color maps of the damage states of the bond area for each scarf angle. All maps correspond to 99% of the ultimate loading. 0 is undamaged and 1 is fully damaged. In SDEG plots, white regions within the bonding area correspond to complete cohesive failure. The top row shows the geometry before loading, where the blue color represents the adhesive..... 65
Figure 2.10. Cross-section photographs of 2.8° specimens, showing example bond-lines with and without defects..... 67
Figure 2.11 Modeling geometry for the investigation of bond defects on the mechanical response. V refers to single-void samples, where the number indicates the size of the void in mm. P refers to the distributed pore scenario with a constant pore diameter of 1 mm. 67
Figure 2.12. Variation of the normalized load of failure with the fraction of defective area in the adhesive. 68
Figure 3.1. (a) Schematic view of the test specimens before repair. Thickness is exaggerated for clarity. (b) Cross-sectional schematic showing the repair geometry. Film adhesive and prepregs are used for prepreg repairs and adhesive impregnated dry fabrics are used for the wet lay-up repairs. Dimensions are in mm. 73
Figure 3.2. Photographs of the test setup for a representative prepreg repaired specimen, (a) front surface, (b) back surface. 76
Figure 3.3. Computed tomography (CT) images of a representative prepreg repair zone before tensile testing. (a) A general view showing the cross-section used for the repair examination. (b) Cross-sectional view of the same CT scan. White contrast regions represent the film adhesive. (c) A close-up view showing the adhesive, parent material, and the repair patch more clearly. 77
Figure 3.4. Force-displacement curves for intact, damaged, stepped, and repaired specimens. The intact coupon's force and displacement data were scaled for a meaningful comparison. 78

Figure 3.5. Photographs of the fracture surfaces of representative test specimens. The values at the bottom right indicate the average strength for each case. (a) damaged specimen, (b) stepped specimen, (c) and (d) prepreg repaired specimens, (e) wet lay-up repaired specimen.. 81
Figure 3.6. Optical micrographs of selected tested specimens. Red regions mark the porosities. (a) Prepreg repaired specimen, (b) Wet lay-up repaired specimen (c) A polarized view of the FM-300K adhesive. 84
Figure 3.7. Normalized tensile strength of the prepreg and wet lay-up repairs for different porosity levels. 85
Figure 3.8. (a) Schematic description of the finite element model. (b) Close-up view of the mesh structure around the steps for wet lay-up repair, and (c) prepreg repair. (d, e) Interface region of the repair; repair patch and parent laminate sides, respectively. Each color represents a separate layer. 87
Figure 3.9. Experimental and numerical load-displacement curves for stepped, damaged, wet lay-up repaired, and prepreg repaired specimens.. 88
Figure 3.10. Failure strength of the specimens as determined by experiments and as predicted by simulations. 89
Figure 3.11. (a) Schematic description of the three paths on the bonding area, defined with respect to the loading direction on the parent laminate side. (b) Damage index distribution with respect to the normalized distance along the bonding area over different paths, shown for the onset of damage. 90
Figure 3.12. Failure map of prepreg repairs corresponding to 99% of the ultimate load. (a) No damage. Grey region indicating the repair patch, blue region is the parent laminate. (b) Fiber damage at the front surface of the parent laminate; no damage is present on the repair zone. (c) Parent laminate on the bonded surface showing no fiber damage. (d) The back surface of the parent laminate showing fiber damage. (e) Photograph of an experimentally tested specimen where parent laminate failure is visible with no damage on the repair zone. 92
Figure 3.13. Failure map of wet lay-up repair corresponding to 99% of the ultimate load. (a) Fiber damage at the front surface. (b) Fiber damage at the back surface. (c)

Adhesive damage on the bonded region. (d) Experimental observation of the front surface exhibiting laminate failure. (e) Experimental observation of the back surface exhibiting laminate failure. (f) Adhesive failure of the bonded region. 93
Figure 3.14. Evolution of the adhesive and fiber damages shown together with the force-displacement curve for the case of wet lay-up. CSDMG represents adhesive damage, and FV1 represents fiber damage. 94
Figure 3.15. Normalized failure load for varying cohesive strength of the adhesive. 95
Figure 3.16. Normalized failure load for different toughness values. 96
Figure 3.17. Normalized von Mises stress distribution over the bonded area of the parent laminate. 96
Figure 4.1 (a) Schematic view of the test specimens before repair. Thickness is exaggerated for clarity. (b) Cross-sectional schematic showing the repair geometry. Film adhesive and prepregs were used for prepreg repairs and adhesive impregnated dry fabrics were used for the wet lay-up repairs. 101
Figure 4.2. Normalized strength values of prepreg and wet lay-up repairs for dry and hot-wet conditions. 103
Figure 4.3. Photographs of the fracture surfaces of representative test specimens. The values at the bottom right indicate the average strength for each case. (a) prepreg repaired specimen in dry condition, (b) prepreg repaired specimen in hot-wet condition, (c) wet lay-up repaired specimen in dry condition, (b) wet lay-up repaired specimen in hot-wet condition 104
Figure 4.4. Optical micrographs of the prepreg repaired specimens. Red regions mark the porosities. 108
Figure 4.5. Optical micrographs of the wet lay-up repaired specimens. Red regions mark the porosities. 109
Figure 4.6. The measured ultrasonic attenuation values for specimens with different porosity levels. 111

CHAPTER 1

INTRODUCTION

1.1 Overview

Composites are a class of materials obtained by combining two or more materials through a specific morphological arrangement. The idea behind the design of composite materials and structures is to combine the desirable properties of the constituents in a way that is not achievable by traditional materials. These enhanced material properties and the tunability of the structural parameters make composites a great alternative to conventional engineering materials.

There are numerous different types of composites ranging from biocomposites to nanocomposites. This thesis focuses on composites used in the aviation industry, mainly reinforcing fibers embedded in a polymer matrix material. Among these, Carbon Fiber Reinforced Polymer (CFRP) is the most popular composite type due to its high specific strength and specific modulus. Therefore, the term composite will refer to carbon fiber reinforced polymer composites for the remainder of the text.

For structural applications in the aviation industry, the main advantage of composite material is its higher specific strength and specific stiffness that enable lighter parts. Composites also offer excellent resistance to corrosion and better fatigue properties than metals. These advantages generated significant demand for the effective utilization of composites in aerospace components. Over the last couple of decades, the analysis, design, and manufacturing of the composites have witnessed significant advances, and the usage of the composites evolved from secondary structures to load-carrying primary structures in airplanes. Boeing was the first company to use composites extensively as primary parts in their 787, corresponding to about 50% of

the aircraft's total weight. Airbus followed A350 XWB, which has a similar fraction with all-composite fuselage and wings [1,2].

There are also some disadvantages of composites, such as high investment costs, susceptibility to moisture, and low damage tolerance. The low damage tolerance of the composite parts makes them prone to manufacturing or in-service defects such as dents, cracks, debonds, delaminations, punctures, and similar.

When the damage results in a reduction in the load-carrying capacity of the part, repair or replacement become necessary. In most cases, the repair is more economical than a replacement. However, to repair a damaged part, first, the extent of the damage should be clarified with an appropriate non-destructive inspection (NDI) method. If the damage is considered negligible from a structural point of view, a cosmetic repair with a proper epoxy is usually sufficient to seal the area and protect it from environmental conditions. On the other extreme, if the damage is considerable and the strength of the part cannot be recovered with any repair method, the part should be removed and replaced. In between these two cases, the recovery of the part with a suitable repair method becomes feasible.

With the more extensive use of composites, the development of time- and cost-effective repair techniques are becoming increasingly important. In addition to the time and cost of the repair, recovery of the original material strength is a crucial issue for the reliable operation of the repaired components in service.

There are numerous methods for repairing the laminated composites, mainly categorized into two main approaches: bolted repairs and bonded repairs. The bolted repairs are based on adding composite or metallic doublers to the damaged area utilizing fasteners. This approach does not require surface preparation, and it is easier in terms of inspection and disassembly processes. On the other hand, the fastener holes create stress concentration points leading to lower strength, and the surface protrusions of the doublers are often not acceptable for aerodynamic surfaces. Because of these disadvantages, recent improvements in adhesive technology have mostly replaced the classical bolted joints with bonded joints. Bonded joints have

desirable features, including smooth surface finish, uniform stress distribution, and higher fatigue strength, making them advantageous for repairing load-bearing components and aerodynamic surfaces.

The efficiency of the repairs depends on many parameters such as repair materials, repair geometry, and processing conditions. All of these parameters should be optimized for each repair task considering the capabilities of the repair facilities. In an ideal repair, the aim is to match the strength, stiffness, strain, and thermal properties of the repair patch with those of the original structure. On the other hand, as most repairs are carried out in-situ, using the original materials and processes is not always possible. In such scenarios, repair patches need to be cured and bonded to the structure without the help of an autoclave but instead vacuum bagging under atmospheric pressure. Further complications can include the inevitable use of low-temperature curing resins and dry fabrics instead of original elevated temperature cure prepregs. High porosity levels in such repairs are very common due to the lack of sufficient pressure and temperature.

Although there have been more than 50 years since the initial use of composites in the aerospace industry, the composite repair is still a challenging task due to various parameters affecting the repair strength and the above-mentioned challenges.

The motivation of the thesis is to establish a reliable repair process and a numerical analysis of the related process for a laminated composite for the on-site repairs. For this purpose, different repair materials and methods are studied. In this manner, the effect of temperature and moisture is also investigated. The main difference from the previous studies is; research has been performed not only on the simplified bonded joints but also on the repaired panels following the exact repair procedures of the aerospace industry. This approach enabled the investigation of the processing and stress distribution in detail.

1.2 Bonded Repair of CFRP laminates

The use of bonded repairs in the aerospace industry is becoming increasingly popular due to the advantages discussed in the previous section. There are numerous bonded repair configurations for the laminated composite parts, such as single lap, double lap, step, and scarf repairs, as shown in Figure 1.1.

Among these, lap repairs have no extra ply removal; and therefore, they are the easiest to apply. In the single lap method, only the damaged area is removed, and the repair layers are laid down on the accessible surface of the part. Although it is a relatively simple repair, the unsymmetrical geometry makes the stress field very complex, and the inevitable bending negatively affects the strength of the joint. Double lap joints exhibiting a symmetric geometry overcome this bending problem; however, this approach requires that both sides of the surfaces are accessible, which often is not the case in aerospace components. For the single lap and double lap repairs, the cavity resulting from the removal of the damaged area can be filled with a proper epoxy mixed with chopped fibers or the plies matching with the dimensions of the emptied area.

The stepped/scarf repairs are the most effective repair techniques, where high strength recovery and aerodynamically smooth surfaces are needed. Since the protrusion from the surface is minimal, the peel stresses acting on the edges of the adhesive are much smaller on these structures, and they do not cause any bending of the adherends. Although they are known as flush repairs, generally, one or two extra plies are laid on the repair section to protect the repair layers from environmental effects and to reinforce the repair. Stepped and scarf techniques differ by the removal geometry of the damaged area, with equal steps or a uniform taper angle, respectively. A composite patch matching the dimensions and the layup of the removed part is then prepared and bonded to the repair zone with an adhesive. Sanding the repair area with predefined step sizes or a smooth angle without damaging the underlying layer is challenging and needs skilled operators.

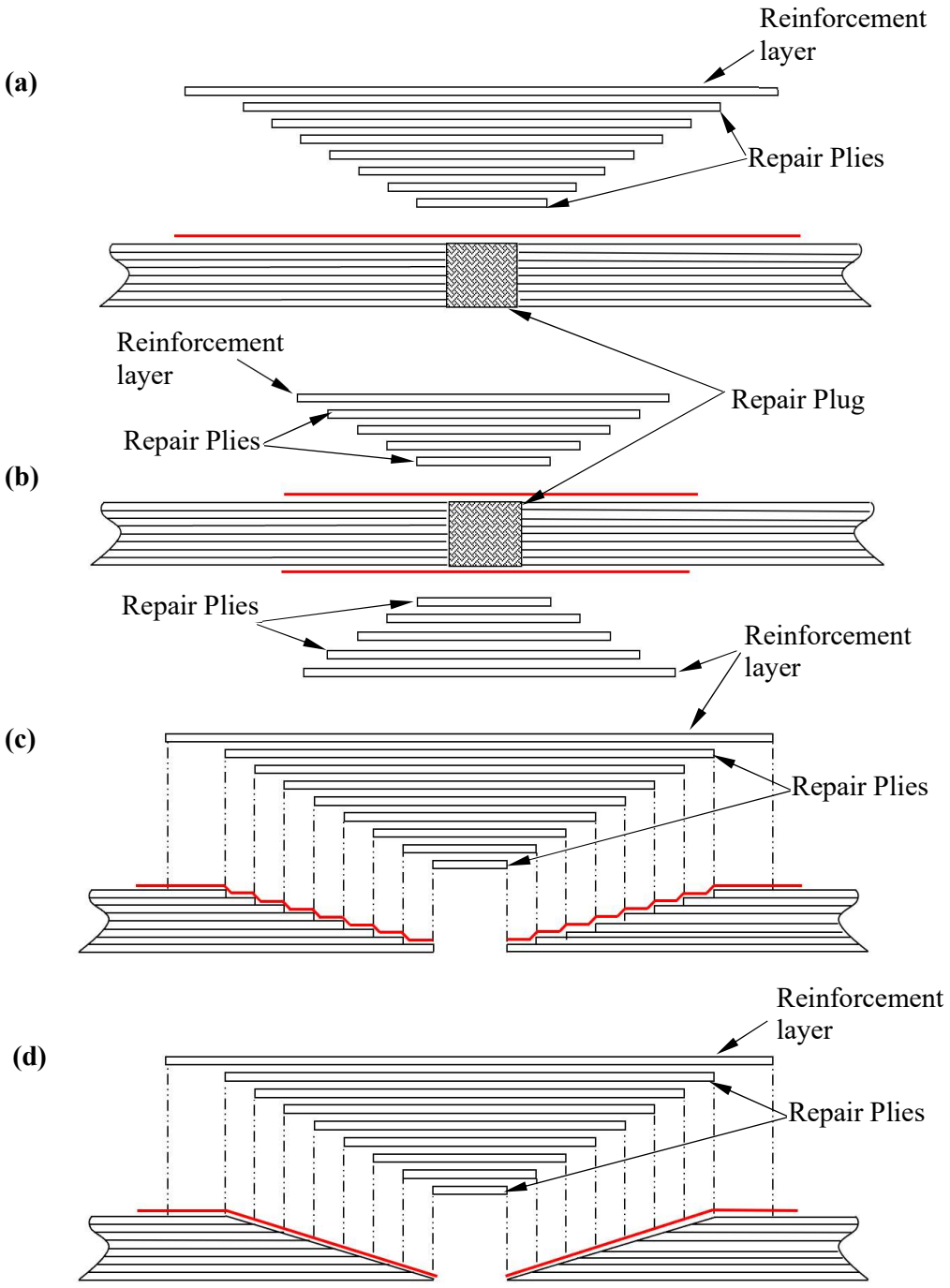

Figure 1.1. Typical repair methods. (a) Single lap repair, (b) Double lap repair, (c) Stepped repair, (d) Scarf repair. Red lines represent the film adhesive for the prepreg repairs.

The basic steps of the structural scarf / stepped repair of a laminated composite are as follows:

1. **Inspection:** Damage assessment is the first step of a repair process. The type of the damage, its position, and dimensions should be determined with an acceptable NDI method to decide the repair method and processing.

2. **Removal of Damage and Surface Preparation:** After assessing the damage, the next step is to remove the paint and external coatings around the damaged area with a proper method. To avoid chemical deterioration of the composite, mechanical methods such as sanding or blasting are preferred instead of chemical strippers for the paint removal. After removing the surface finish and cleaning, the damaged area defined by the NDI method is machined out with a hand grinder, preferably with a circular or oval shape. Then the bonding surface is prepared by sanding with the predefined angle for the scarf method or the step length for the stepped repair. The optimum scarf angle/step length depends on the thickness and the material of the structure, and the type of loading. It is usually defined by the taper ratio (thickness to length ratio of the scarfed region) that ranges between 1:20 to 1:50 in most of the Structural Repair Manuals (SRM) [3,4]. After sanding and verifying the dimensions, the repair area is cleaned using a confirmed solvent and dried before bonding the repair patch. Drying of the part is crucial to avoid debonding due to moisture, especially for the in-service parts.

3. **Selection of Repair Materials and Lay-up of Repair Plies:** The repair materials' selection directly affects the repair processing. Depending on the type of the repair plies, adhesives, and the related cure cycles, repairs may be categorized into two main methods as “prepreg repairs” and “wet lay-up repairs”. The repairs that utilize pre-impregnated fibers are called “prepreg repairs”. The curing temperature for these types of repairs is generally between 120°C to 180°C depending on the properties of the prepreg resin. The repairs where two-part adhesives with cure temperatures below 100°C are used to wet and bond dry fabrics to the repair area are called “wet lay-up repairs”. In wet lay-up repairs, the adhesives

serve as the resin of the composite system. So, adhesive and resin can be used as synonyms for this type of repair. In the wet lay-up repairs, mixing the adhesive system properly is very important to obtain satisfactory results. In addition, the fiber to resin ratio of the repair patch, which directly affects the repair strength, should be adjusted according to the defined repair procedure

The repair patch for both types of repairs can be either pre-cured and secondarily bonded to the repair area or co-bonded. The advantage of the pre-cured patch is that it can be formed in the same manner as the parent laminate in an autoclave. On the other hand, the co-bonded repairs are generally more robust due to both chemical and physical bonds between the surfaces [5].

The repair plies are laid-up on the scarfed area for the co-bonded repairs, matching the removed layers' orientation and dimension. For the prepreg repairs, before the lay-up of the repair plies, generally, one or two layers of film adhesive are used between the repair patch and the parent laminate to enhance bonding. The compatibility of this film adhesive and the prepreg used in the repair patch should be verified, and the cure cycle should be adjusted accordingly to avoid excessive porosity formation. For prepreg and wet lay-up repairs, one or two extra layers overlapping the repair patch are used to recover any deficiency caused by the processing and to protect the repair plies from moisture. During the lay-up of the repair plies, the repair area should be vacuumed at every three or four plies to improve the resin flow and avoid entrapment of the volatiles.

4. **Final Bagging and Cure Process:** After completing the lay-up, final bagging is done, and a full vacuum is applied to the bag. Supplementary materials such as peel ply, bleeder, breather, and solid or perforated release films are used to complete the vacuum bagging process. Several vacuum ports are also attached to the bag to monitor the vacuum value during the curing process. The proper application of the vacuum during the cure cycle is crucial for a satisfactory bond. It helps to consolidate plies, extract moisture, solvents, and volatiles, and enhance resin flow.

Depending on the repair materials and facilities, the heating can employ an autoclave, furnace, heat blanket, or heat lamps. The temperature during the cure cycle is monitored with thermocouples. Proper placement of the thermocouples on the repair area is essential since the temperature can vary across the repair area. The temperature on each part of the repair should be within the desired limits. Also, optimum ramp-up (heating) and ramp-down (cooling) rates eliminate excessive void formation, weak bonds, and distortion of the parts.

5. **Inspection and Restoration of the Surface Finish:** The part is debagged and cleaned from the adhesive residues after curing. Then the repair is verified with a proper NDI method. If any defect is detected on the repair, the repair should be removed and must be repeated. Otherwise, the last step is to restore the removed paint and coating. Then the part is ready for service.

To guarantee the efficiency of the repair, it is vital to follow the predefined process instructions. So, the relationships between bond parameters and the strength of the repaired part should be clearly understood for the material and process optimization. In this context, many theoretical and experimental studies have been carried out in the literature. In the following sections, information about these studies and theoretical infrastructure will be given in detail.

1.3 Bonded Repair Analysis of CFRP Laminates

This section will give a broad information and literature review about the analysis of a bonded repair of a composite laminate in detail.

A composite bonded repair generally consists of three structural elements; parent laminate, repair patch, and bonding adhesive. Thus, the analysis of a bonded repair requires verifying all three components by using the appropriate failure criteria. In the following sections, the failure criteria for the composite adherend and the adhesive are explained.

1.3.1 Failure Analysis for the Composite Adherends

The failure theories for composite materials differ from conventional engineering materials due to their anisotropic and non-homogeneous nature. Furthermore, a universal failure criterion is difficult to establish due to the diversity in the design and the material properties of composites. Therefore, this section will provide an overview of a range of approaches for modeling the failure behavior of composite structures.

Failure analysis of the composite structures can be divided into two main parts; first, a damage initiation criterion for the lamina, known as first ply failure, and second, evaluating the total laminate strength through a progressive failure analysis approach. These models result in complicated expressions; their implementation to a specific geometry usually requires finite element modeling.

1.3.1.1 Lamina Failure Analysis

Over the last three decades, there have been many efforts to develop accurate predictive tools for the failure of composites. In 1991, an expert meeting, World Wide Failure Exercise (WWFE), was held in St Albans (UK) to set the status of the available polymer composite failure theorems [6,7]. In this meeting, leading researchers in the field all over the world compared the failure predictions of their models and theories for the same set of geometry, loading, and material properties [8]. The contributors provided a discussion on the strengths and the weakness of the failure theories. Also, guidelines and suggestions to composite structural designers were presented in these studies [6,7,9,10]. This exercise showed that there are no universal criteria that can fully capture the experimentally observed failure behavior. On the other hand, the meeting results showed that Tsai-Wu criteria [11] along with Cuntze-Freund [12] and Puck-Schurman [13] provided the best results at the lamina level, and Bogetti's theory [14] captured the initial failure load in multidirectional laminates accurately.

After the WWFE meetings, NASA Langley Research Center revised the existing theories to introduce some enhancements. As a result, they introduced LARC03, LARC04, and LARC05 failure theories by extending the approach to three-dimensional stress state [15–18].

To sum up, the most famous failure theorems, which are available in a form that can be readily utilized primarily in the aerospace industry, are Maximum Stress [19], Maximum Strain [19], Tsai-Hill [20], Tsai-Wu [11], Hashin [21] and Yamada-Sun [22], Puck [13] and LARC theorems [15–18].

The main failure modes in the above failure theorems are fiber tension, fiber compression, matrix tension, and matrix compression, all intralaminar-type failures. On the other hand, delamination is an interlaminar failure mode, and it refers to the formation of an interfacial crack or a debond between adjacent lamina. Based on the stress interactions, the failure theories for composite materials can be classified into three groups:

- Non-interactive failure criteria
- Interactive failure criteria
- Separate mode failure criteria

Non-Interactive Failure Criteria

These criteria, also called the limit criteria, compare the lamina stresses or strains with the corresponding allowable values separately. In other words, no interaction is assumed between the stresses (or strains) in different directions. As an example, the Maximum Stress or Maximum Strain criteria fall under this category. Maximum Stress failure envelope defines a rectangle in 2D space. The failure envelope of Maximum Strain is close to that of Maximum Stress but slightly skewed due to the effect of Poisson's ratio. These criteria can be expressed as follows:

Maximum Stress:

$$\frac{|\sigma_{11}|}{|X|} = 1;\ \frac{|\sigma_{22}|}{|Y|} = 1;\ \frac{|\tau_{12}|}{|S|} = 1 \tag{1.1}$$

Maximum Strain:

$$\frac{|\varepsilon_{11}|}{|X_\varepsilon|} = 1;\ \frac{|\varepsilon_{22}|}{|Y_\varepsilon|} = 1;\ \frac{|\gamma_{12}|}{|S_\varepsilon|} = 1 \tag{1.2}$$

Where σ_{11}, σ_{22}, and τ_{12} (ε_{11} , ε_{22}, and γ_{12}) are the stresses (strains) in the fiber direction, matrix direction, and shear direction in a lamina, respectively. X, Y, and S are the corresponding allowable longitudinal, transverse, and shear values. These allowable are tension allowable if the stresses or strains are greater than zero and otherwise compression allowable. Using these criteria, one can separately identify the onset of individual failure in terms of fiber failure, transverse matrix failure, or shear matrix cracking.

Under transverse tensile loading, these criteria do not account for the constraining effect of adjacent orthogonal plies on delaying the initiation and arresting the propagation of matrix cracks. As a result, the transverse failure is dominated by the matrix properties for unidirectional laminas, leading to the laminate strength's underprediction.

Interactive Failure Criteria

These criteria predict the failure load using a quadratic or higher-order polynomial equation involving stress or strain components, obtained by curve fitting to experimental data. Tsai-Hill and Tsai-Wu are the most popular interactive criteria used [6]. However, compared to the Maximum Stress or Maximum Strain criteria, their primary disadvantage is that the interactive type criteria cannot identify the failure mode.

Tsai-Hill criterion is based on Hill's proposed yield criterion [23] for anisotropic materials, describing a smooth elliptical failure envelope. It is expressed as follows:

Tsai-Hill:

$$\left(\frac{\sigma_{11}}{X}\right)^2 + \left(\frac{\sigma_{22}}{Y}\right)^2 - \left(\frac{\sigma_{11}}{X}\right)\left(\frac{\sigma_{22}}{X}\right) + \left(\frac{\tau_{12}}{S}\right)^2 = 1 \tag{1.3}$$

Even though stress interaction is considered in Tsai-Hill, there is no way to distinguish between tension and compression, which is not the case for the majority of the FRP composites.

Unlike Tsai-Hill, Tsai-Wu accounts for tensile and compressive stress through linear terms, which can be expressed as follows:

Tsai-Wu:

$$F_1\sigma_{11} + F_2\sigma_{22} + F_{11}{\sigma_{11}}^2 + F_{22}{\sigma_{22}}^2 + 2F_{12}\sigma_{11}\sigma_{22} + F_{66}{\tau_{12}}^2 = 1 \tag{1.4}$$

$$F_1 = \frac{1}{X_T} - \frac{1}{X_C} \qquad F_{11} = \frac{1}{X_T X_C} \tag{1.5a}$$

$$F_2 = \frac{1}{Y_T} - \frac{1}{Y_C} \qquad F_{22} = \frac{1}{Y_T Y_C} \tag{1.5b}$$

$$F_{12} = -\frac{1}{2\sqrt{F_{11}F_{22}}} \qquad F_{66} = \frac{1}{S^2} \tag{1.5c}$$

Subscripts T and C denote tension and compression, respectively. The interactive stress constant F_{12} should ideally be determined experimentally by a biaxial test. Due to the difficulties in the experimental evaluation of F_{12}, Eqn. (1.5c) can be used as an approximation as proposed by Tsai and Hahn [24].

Separate Mode Failure Criteria

These criteria distinguish the fiber failure criterion from the matrix failure criterion. Stress interaction between different directions depends on the specifics of the

criterion within this group. Yamada-Sun, Hashin, Puck, and LARC failure theorems are some examples of separate mode failure theorems.

Yamada and Sun failure criteria is a fiber failure criterion based on the assumption that laminate failure occurs when the following condition is satisfied in any of the plies.

Yamada and Sun:

$$\left(\frac{\sigma_{11}}{X}\right)^2 + \left(\frac{\tau_{12}}{S_{IS}}\right)^2 = 1 \tag{1.6}$$

Where S_{IS} is the in-situ strength of the ply.

Unlike Yamada and Sun, in 1980, Hashin proposed two distinct failure mechanisms, one associated with the fiber and one associated with the matrix in tension and compression. The two distinct failure modes occur in two different fracture planes, and only relevant stress components on the associated fracture plane of each mode will contribute to the failure criteria for that failure mode. Consequently, the failure envelope described by Hashin failure criteria is only piecewise smooth, with each branch modeling a distinct failure mode. Hashin criteria can be expressed as follows:

Hashin:

Fiber Tension ($\sigma_{11} \geq 0$):

$$\left(\frac{\sigma_{11}}{X_T}\right)^2 + \left(\frac{\tau_{12}}{S}\right)^2 = 1 \tag{1.7}$$

Fiber Compression ($\sigma_{11} \leq 0$):

$$\frac{\sigma_{11}}{X_C} = 1 \tag{1.8}$$

Matrix Tension ($\sigma_{22} \geq 0$):

$$\left(\frac{\sigma_{22}}{Y_T}\right)^2 + \left(\frac{\tau_{12}}{S}\right)^2 = 1 \tag{1.9}$$

Matrix Compression ($\sigma_{22} \leq 0$):

$$\left(\frac{\sigma_{22}}{2S_T}\right)^2 + \left(\frac{Y_C}{2S_T} - 1\right)\frac{\sigma_{22}}{Y_C} + \left(\frac{\tau_{12}}{S}\right)^2 = 1 \tag{1.10}$$

where S is the longitudinal or in-plane shear strength as defined previously and S_T is the transverse or out-of-plane shear strength which is difficult to find experimentally. Hashin criteria provide an improvement for the prediction of intralaminar failures. On the other hand, its prediction for the matrix failure under compression is the shortcoming of the method. This is due to the quadratic failure criteria, which implies that the fracture plane is the maximum transverse shear plane – which cannot be accepted as a general rule. To overcome this shortcoming of Hashin, Puck, and Schurman [13], and more recently Davila et al. [16] introduced matrix failure theorems based on the Mohr-Coulomb failure theory and fracture mechanics.

In the Puck failure theory, a set of inter-fiber failure (IFF) modes, namely, matrix cracking or matrix/fiber debonding, are evaluated besides the fiber failures. Three different failure modes named A, B and C represent different orientations of fracture planes relative to the reinforcing fibers. The fracture plane is shown in Figure 1.2.

Puck:

Mode A failure represents a transverse crack due to tensile transverse stress and shear stress.:

$$\sqrt{\left(\frac{\tau_{12}}{S_{21}}\right)^2 + \left(1 - \rho_{\perp\parallel}^{(+)}\frac{Y_T}{S_{21}}\right)\left(\frac{\sigma_2}{Y_T}\right)^2} + \rho_{\perp\parallel}^{(+)}\frac{\sigma_2}{S_{21}} + \left|\frac{\sigma_1}{\sigma_{1D}}\right| = 1 \qquad \sigma_2 \geq 0 \tag{1.11}$$

Mode B represents a transverse crack due to compressive transverse stress and shear stress:

$$\frac{1}{S_{21}}\left(\sqrt{(\tau_{21})^2 + \left(\rho_{\perp\parallel}^{(-)}\sigma_2\right)^2} + \rho_{\perp\parallel}^{(-)}\sigma_2\right) + \left|\frac{\sigma_1}{\sigma_{1D}}\right| = 1 \quad \sigma_2 < 0 \; and \; 0 \leq \left|\frac{\sigma_2}{\tau_{21}}\right| \leq \frac{R_{\perp\perp}^A}{|\tau_{21C}|} \tag{1.12}$$

Mode C represents a failure in an angled plane due to a dominant compressive transverse stress and shear stress, which causes fibers to become displaced:

$$\left[\left(\frac{\tau_{21}}{2\left(1+\rho_{\perp\perp}^{(-)}S_{21}\right)}\right)^2+\left(\frac{\sigma_2}{Y_C}\right)^2\right]\frac{Y_C}{(-\sigma_2)}+\left|\frac{\sigma_1}{\sigma_{1D}}\right|=1 \quad \sigma_2<0 \; and \; 0\le\left|\frac{\tau_{21}}{\sigma_2}\right|\le\frac{|\tau_{21C}|}{R_{\perp\perp}^A} \tag{1.13}$$

Where $\rho_{\perp\parallel}^{(-)}$ and $\rho_{\perp\parallel}^{(+)}$ are the slopes of (σ_2, τ_{21}) the fracture envelope and are related with the other parameters through the following equations:

$$R_{\perp\perp}^A=\frac{Y_C}{2(1+\rho_{\perp\perp}^{(-)})}=\frac{S_{21}}{2\rho_{\perp\parallel}^{(-)}}\left(\sqrt{1+2\rho_{\perp\parallel}^{(-)}\frac{Y_C}{S_{21}}}-1\right) \tag{1.14}$$

$$\rho_{\perp\perp}^{(-)}=\rho_{\perp\parallel}^{(-)}\frac{R_{\perp\perp}^A}{S_{21}} \tag{1.15}$$

$$\tau_{21C}=S_{21}\sqrt{1+2\rho_{\perp\perp}^{(-)}} \tag{1.16}$$

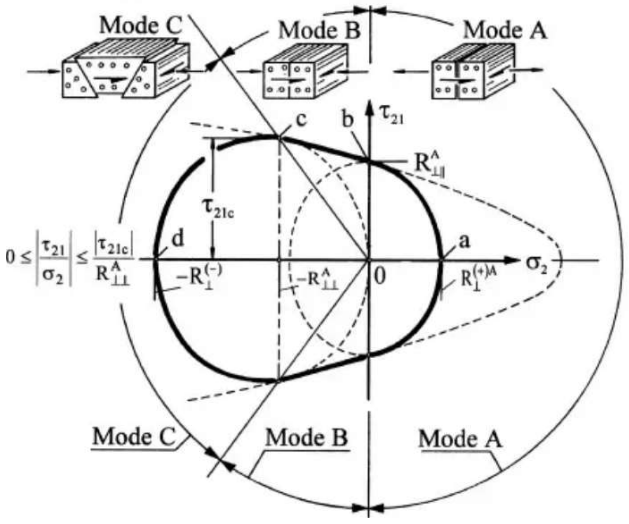

Figure 1.2. Fracture envelope for Puck's IFF failure modes. Figure taken from ref. [13].

Combining Hashin's failure theory and Puck's failure plane concept, Davila introduced a new failure theorem named LARC03 [16]. This theorem is associated with Mohr-Coulomb's theory for matrix failure in compression and Dvorak's

fracture mechanics approach for matrix cracking in tension. LARC03 includes the in-situ effect occurring under the presence of both in-plane shear and transverse tensile stresses. The in-situ effect can be explained as the higher transverse tensile and shear strength of a ply due to the constraining effect of the adjacent plies with different orientations. This enhancement of strength also depends on the number of plies clustered together and the orientation of adjacent plies. These in-situ strengths calculated using fracture mechanics are dependent on fracture toughness values (G_{IC} and G_{IIC}); elastic moduli (E_1, E_2), Poisson's ratio (ϑ_{12}) and the geometry of the plies or the crack. The fiber failure under tension is a non-interacting maximum strain criterion for LARC03. For the fiber compression, a criterion for the fiber kinking is also developed by considering the fiber misalignment under load. The matrix failure criterion is considered in the coordinate frame of this misalignment.

LARC04 [17] and LARC05 [18] are extensions of LARC03 plane stress criteria to account for general three-dimensional loading and in-plane shear non-linearity. LARCO5 differs from LARC03 only for the matrix failure under transverse tensile failure formulation, which includes the contribution of stress normal to the fracture plane. Details of the formulation for the LARC criteria are not given here; the reader can refer to the references for further information [16–18].

A comparison of different failure criteria for a set of WWFE test data [25] for unidirectional composite E-Glass/LY556 is given in Figure 1.3. The selected failure theorems give similar results for the tensile loading conditions except for the Maximum Stress criteria, which is less conservative. The failure theorems have more distinctive properties under compressive loading. LARC03 and Puck can closely predict the failure envelope under compression, whereas Hashin gives conservative results.

Among all the above-mentioned criteria, Hashin's model is widely used in structural applications, especially in the aerospace industry, and laid a basis for, further progress throughout later years. Moreover, due to its simplicity and accuracy, it has also been incorporated into many FEA commercial codes,

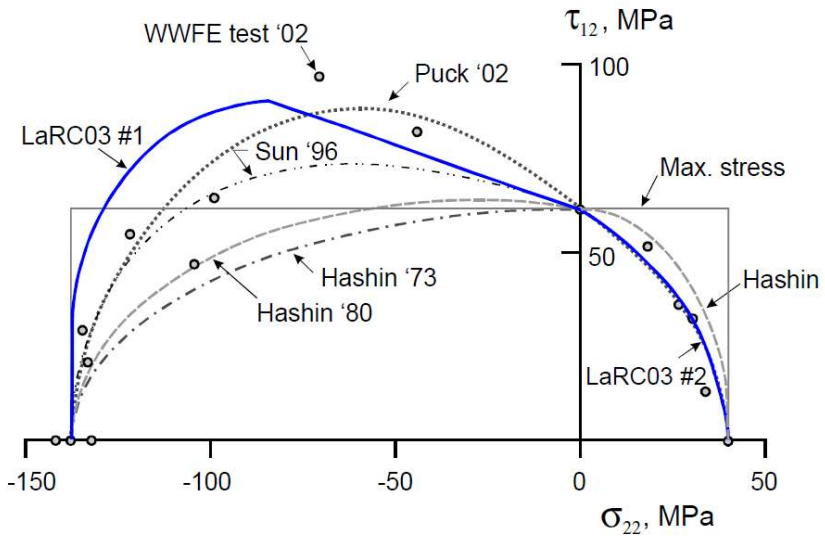

Figure 1.3. Comparison of different failure criteria with the WWFE test results. Figure taken from ref. [25]

1.3.1.2 Laminate Failure Analysis

The previously discussed failure criteria are used to find the onset of damage in a lamina which does not necessarily mean the failure of the composite. To predict the total failure, the progression of the damage to the whole laminate should also be considered, which is a non-trivial task due to the complicated failure mechanisms. Since the interlaminar damage (delamination) is out of the scope of this work, the focus here will be on the methods for the damage progression for the intralaminar damage.

For highly fiber-dominated laminates, progressive failure analysis is usually not necessary. Instead, laminate failure may be taken to coincide with the lamina fiber failure in the load direction. Since no stiffness reduction is included in this method, applying and predicting the laminate failure is straightforward. Therefore, this method is called “First Ply Failure” or “Sudden Failure”. Although this method gives

close predictions for the fiber-dominated laminates, it is too conservative for the majority of the cases involving matrix failures.

Progressive failure analysis models the evolution of the failure starting from the failure of the first ply until the ultimate failure. Once the failure starts, the model implements a material degradation scheme to account for the associated load-bearing capacity reduction. Material degradation models available for laminated composite structures can be categorized into two main groups; continuum damage mechanics (CDM) using internal state variables and ply discounting approaches [26].

Continuum damage mechanics models assume a continuous material regardless of the damage state. The internal damage is defined through elastic stiffness degradation coefficients, which are functions of state variables. Talreja [27–29] and Chang and Chang [30] were the pioneers in implementing the CDM methods to the composites. Later on, many other authors also worked on the CDM modeling of composites [31–33]. Matzenmiller [34] introduced a new model based on CDM coupled with classical thermodynamic theory. Internal variables describe the evolution of the damage and the degradation of the material stiffness. This work is the basis of the in-built composite damage evolution model in Abaqus Finite Element Analysis (FEA) software [35]. The CDM models generally require additional material data to model the damage progression state. As a result, implementing these models requires more test data and more effort than the direct property degradation methods.

Ply discount methods are based on reducing the elastic material stiffness coefficients by a factor in the case of a ply failure. First, the stresses and strains are calculated in each ply, and then a lamina failure check is performed with a selected failure criterion. If failure is detected in any of the plies, then the elastic stiffness values of the lamina are degraded accordingly. Next, the system is reanalyzed with the existing stresses and strains. This cycle continues until no additional load can be sustained, which is the ultimate failure of the laminate.

Many post-failure material property degradation models may be categorized into three main categories: instantaneous unloading, gradual unloading, and constant stress, as shown in Figure 1.4 [36].

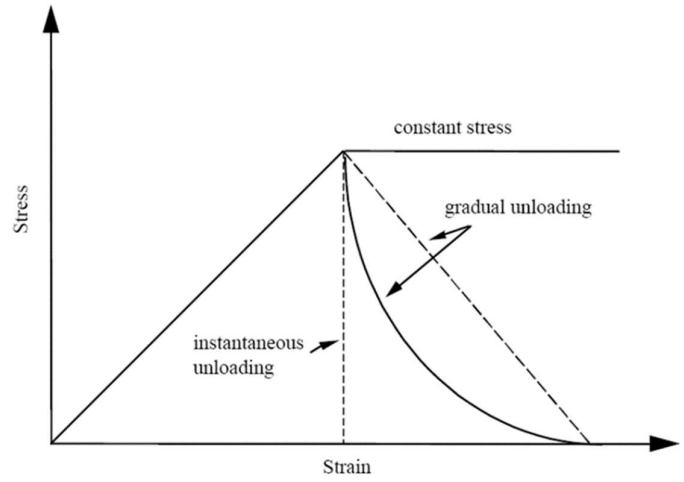

Figure 1.4. Types of ply discount methods in composite laminates. Figure taken from ref. [36].

In the "**Instantaneous (or Sudden) Degradation**" method, the material stiffness coefficients associated with the mode of the failure are degraded to zero abruptly. A very small degradation factor (e.g., 10^{-4}) is common to avoid convergence problems due to ill-conditioned stiffness matrices and singularities. Sleight [36] has performed a study to compare different degradation factors such as 10^{-1}, 10^{-2}, and 10^{-20} for the instantaneous unloading case for a rail-shear specimen. The study showed that the rate of material degradation had little effect on the failure prediction. Many other authors also used sudden degradation progressive failure analysis with very small degradation factors [26,30,37–39].

Gradual Degradation Method: The material elastic properties associated with the relevant mode of failure are recursively reduced until they reach zero. The gradual degradation may be linear or exponential, as shown in Figure 1.4. Selecting the degradation factor is crucial to model the damage accumulation in gradual

degradation modeling correctly. A factor close to zero would resemble the sudden degradation model, resulting in ignorance of the damage aggregation. On the other hand, a factor close to 1 is not preferred as it considerably increases the computational load. Reddy [40] has performed a numerical analysis with different SRC (stiffness reduction coefficient) values between 10^{-6} and 0.6 and found that the curves capture the experimental behavior for larger values of SRC. For an SRC factor of 0.5, the ultimate load prediction was within ±10%. Chang [30] used a gradual degradation scheme according to a Weibull distribution. Petit and Waddoups [41] and Sandhu [42] also worked on gradual unloading based on a nonlinear stress-strain relationship.

Constant Stress Method: The method assumes that a lamina will continue to support its failure load even after failure but no additional loads. There is not much found in the literature for the application of this method, but Tsai's approach can be given as an example of constant stress application [24,43].

In summary, basic steps to perform progressive failure analysis for a composite laminate are as follows:

1. Find the stresses and strains in each lamina.
2. Decide the failure criterion to be used and check the stresses or strains with this criterion.
3. If failure is detected, apply the degradation model (decide the method, degradation parameters, interaction between stresses, which elastic parameters to be degraded) and find the new constitutive matrices.
4. Repeat the steps above until the final failure of the laminate.

The previously mentioned failure methods are for unidirectional tape laminates where matrix failure is a concern for the transverse direction on a lamina. On the other hand, woven fabrics – structures consisting of continuous warp and weft fibers weaved in a pattern are also widely used in practice, especially in impact-prone areas of airplanes. The mechanical properties and damage behavior of fabric laminates are considerably different from unidirectional tape laminates. Therefore, the previous

findings on the unidirectional laminates should be modified accordingly to investigate the fiber failure in both directions [44–53].

1.3.2 Failure Analysis of the Bonded Joints

To find the strength of a repaired composite part, the failure phenomenon of the adhesive should be clearly understood and evaluated. As mentioned before, the aim of a repair is to ensure the failure of the adherend before the failure of the bond. ASTM D5573-99 [54] describes the methods of classifying and characterizing the failure modes in adhesively bonded FRP joints. The bond failure can be classified mainly into two groups: an adhesive failure and cohesive failure.

Adhesive failure is the interfacial failure between the adhesive and the composite adherend due to improper surface preparation on the bonding area. This type of failure can be avoided by following standardized directives for the bonding process.

Cohesive failure is the failure of the adhesive itself, which should be evaluated to find the strength of the bonding. Since the pioneering work of Volkersen [55] in 1938, there have been many studies evaluating the adhesive failure in a bonded joint. These studies can be grouped into two main categories as follows:

- Closed-Form Analysis (Analytical Methods)
- Numerical Analysis

1.3.2.1 Analytical Methods

The earliest analytical method for a single lap joint was the linear shear-lag model developed by Volkersen [55], which assumed that the adhesive deforms only in shear whilst the adherend deforms in tension. The main drawback of this model is the neglection of the eccentricity of the applied load. This simplification causes problems in the case of bending moments in the adherends and shear deformations, which are especially critical for composite adherends having low shear and

transverse moduli and strength. Therefore, the model is more convenient for analyzing double lap joints rather than single lap joints. The representation of the Volkersen model with elastic adherends and the distribution of the shear stress over the bonded area is shown in Figure 1.5 [56].

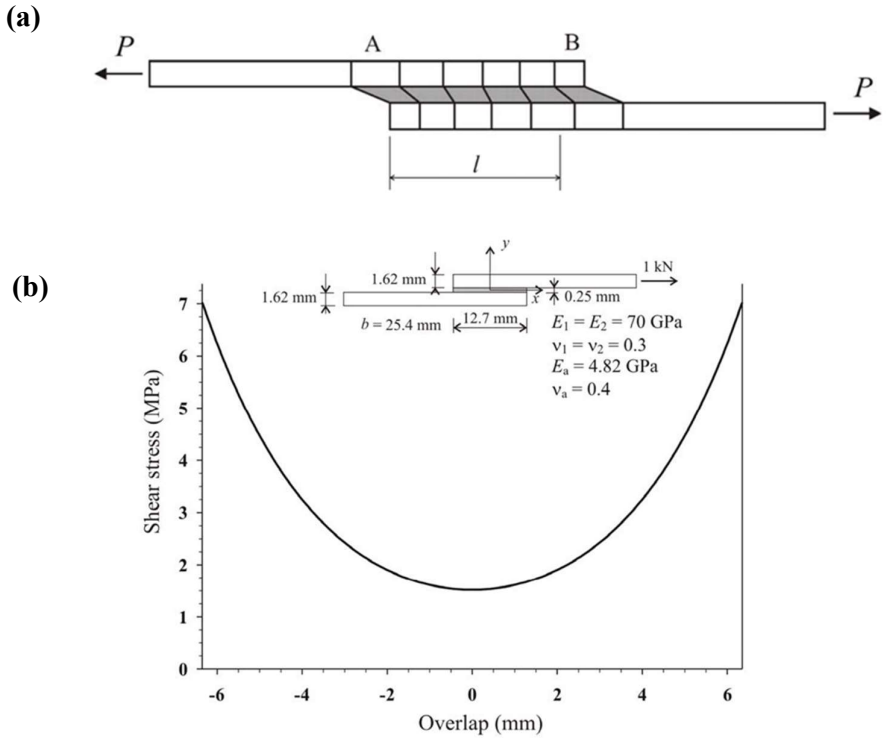

Figure 1.5. (a) Volkersen model with elastic adherends, (b) Distribution of the shear stress distribution over the bonded area. Figure taken from ref. [56].

In 1944, Goland and Reissner [57] improved the Volkersen model by accounting for the adherend bending and adhesive peel stresses. The rotation of the overlap region alters the load path and induces significant peel stresses at the end of the adhesive. The representation of the model and shear and peel stress distribution over the bonded area is shown in Figure 1.6.

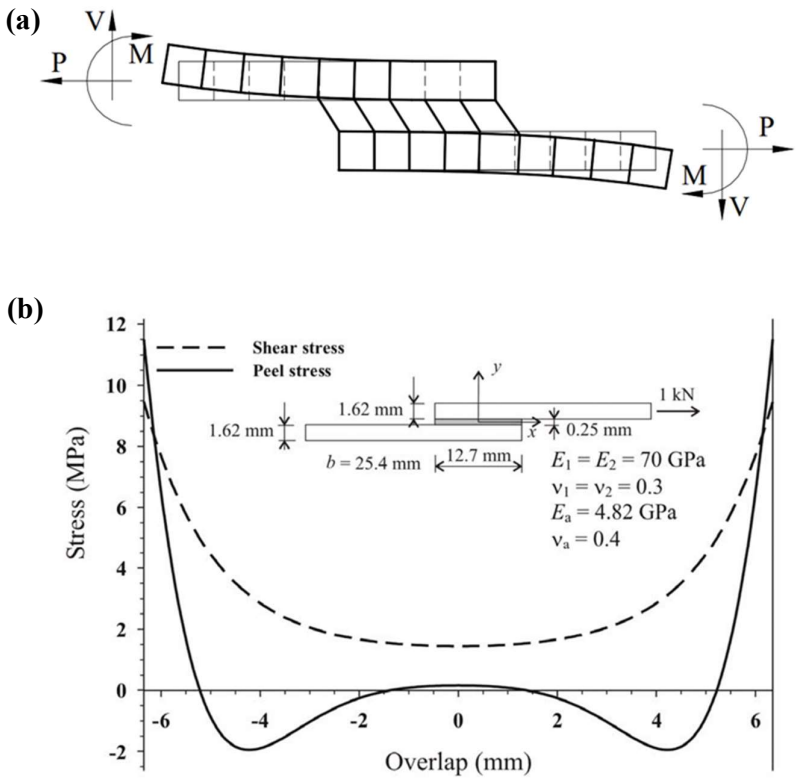

Figure 1.6. (a) Goland and Reissner model with elastic adherends. (b) Distribution of the shear stress distribution over the bonded area. Figure taken from ref. [56].

These models do not account for the adhesive plasticity, whereas Hart-Smith developed several models for various joint configurations considering the elastoplastic properties of the adhesive and the mechanical properties of the composite adherends [58–60]. These studies include models for the single lap, double lap, and scarfed/stepped joints. He also studied the effect of the various factors on bond strength, such as thermal mismatch, adherend thickness, adhesive thickness, adhesive modulus, and lay-up.

Tsai et al. [61] assumed that the shear stress is linear through the adherends and applied a correction factor to the shear lag model. Many other researchers proposed analytical solutions considering linear and non-linear material models for isotropic

and composite adherends. A comprehensive literature review for many of these analytical models can be found in work performed by Da Silva et al. [56]. Most of these models are two-dimensional assuming plane stress or plane strain conditions.

The analytical modeling of isotropic adherends for all bonding types is a highly mature field similar to the case of the single lap and double lap joint configurations for composite adherends. There are few analytical works on the scarf/stepped composite joints, but none considers ply orientations in the adherends [60,62–65].

The analytical modeling of scarf/step joints with composite adherends is more complex due to the stiffness variation along the bond-line [66–68]. Furthermore, the complex geometries and loading conditions of actual repaired parts make the analytical route challenging for the proper design of composite joints and repairs. Therefore, there has been a strong demand for numerical tools that can tackle these problems accurately.

1.3.2.2 Numerical Methods

Finite element analysis (FEA) is the most common approach for the detailed investigation of the joint strength by modeling the interfaces by various approaches such as continuum mechanics, fracture mechanics, and cohesive zone methods.

Continuum mechanics approach assumes the material as a continuous medium regardless of the damage state. The stress, strain, or strain energy values are compared with the allowable values via a failure criterion. The success of the selected failure criterion is mainly relevant to the ductility of the adhesive. The primary maximum principal stress criterion gives accurate results for a brittle adhesive, although the singularity at the corners should be tackled by using finer mesh sizes [69]. Also, shear stress-based failure criteria have been widely used in the literature, which compares the shear stress in the bond-line to the bulk adhesive shear stress [57,70,71].

For ductile adhesives, stress-based limit criteria give conservative results because they do not take the load-carrying capacity after adhesive yielding into account. For these types of adhesives, when plastic deformation is apparent, strain-based failure criteria give more accurate results [60,72,73].

There are also criteria for describing the yield behavior of adhesives, such as Von-Misses and Tresca criteria and Drucker Prager plasticity model [74–76]. While the details of these models and criteria are beyond this thesis's scope, there is a comprehensive literature survey for the continuum mechanics approaches by Campilho et al. [77].

Fracture mechanics approach assumes a pre-defined crack and aims to determine the stress state in front of the crack. In the bonding process, cracks, debonding, porosities, and other imperfections within the adhesive are stress concentration points that act as damage initiation sites. In this method, the size of the defect is compared with the critical defect size, and if the threshold is exceeded, propagation and final failure occur. The fracture mechanics approach can be formulated through stress intensity factor definitions or energy-based concepts.

In the stress intensity factor approach, considering an existing crack, a stress intensity factor, K, is calculated as a function of applied stress, crack size, and part geometry. Also, failure is assumed to happen when this stress intensity factor exceeds the material's fracture toughness, K_c, value. From this point on, the crack will grow rapidly until it fractures. The stress intensity factor also depends on the loading direction. Three primary modes define the orientation of a crack relative to the loading, as shown in Figure 1.7. Mode I is the opening case, and mode II and mode III are the in-plane and out-of-plane shearing modes. There exists a stress intensity factor for each mode, and crack will occur when $K = K_c$ for each case. The crack may be loaded in one mode only or a combination of the modes.

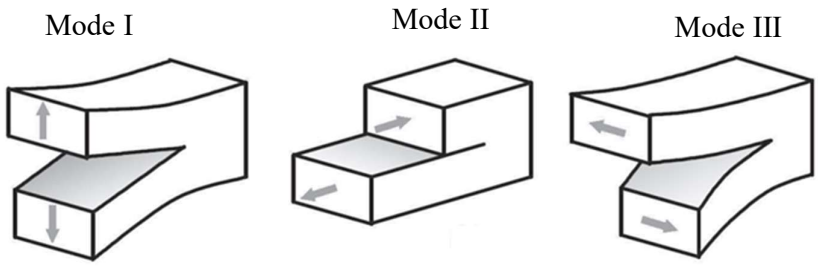

Figure 1.7. Failure modes in adhesive joints.

In the energy-based approach, a defect will propagate when the energy release rate, G, at the crack tip is equal to the critical energy release rate, G_c, for each mode of loading. Similar to the stress intensity factors, G_c is also a mechanical property of the material. In most bonding applications, the adhesive is loaded not only under tension or shear but a combination of both. Therefore, while the crack grows in mode I in an adhesive in bulk form, the crack will propagate in a mixed-mode in a joint due to the constraints coming from the rigid adherends.

Numerous studies have been performed to evaluate bonded joints with fracture mechanics approaches [78–82], but this continues to be an area of research due to the complexities encountered. The shortcomings of the fracture mechanics are eliminated mainly by using the Cohesive Zone Model (CZM), which will be discussed next in the following section.

1.3.2.2.1 Cohesive Zone Model

Among the models for predicting the behavior of adhesive joints with FEA, the cohesive zone model (CZM) provides one of the most effective approaches. CZM enables the prediction of the failure loads and damage onset locations and the progression of damage and failure paths without an initial crack. A relation is set between the traction value and the elongation of the cohesive elements. The point where the traction value reaches the critical value marks the start of the damage. When the maximum fracture toughness value is attained (the area under the traction-

separation curve), the traction is reduced to zero, and new crack surfaces are formed. The schematic representation of damage progression is shown in Figure 1.8.

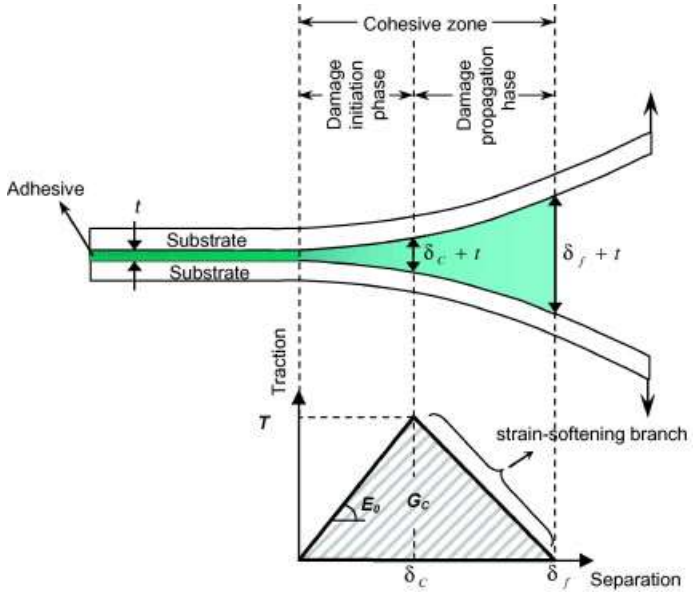

Figure 1.8. Damage progression schematic in an adhesively bonded joint. Figure taken from ref. [83].

The earliest studies on the CZM go back to the publications of Dugdale [80] and Barenblatt [84], who introduced the concept of crack tip plasticity and equilibrium in elastic bodies with cracks. Hillerborg's model [85] was similar to Barenblatt's model with the introduction of an extra tensile strength concept. Hillerborg's model allowed the initiation of new cracks as well as the propagation of the existing ones. Since this pioneering work, numerous studies have been performed to find the adhesive joint strength and delamination propagation in composite parts using CZM [86–99]. The recent advances in the programming of CZM by conventional FEM analysis programs, make this method widely used.

Depending on the joint configuration and the adhesive type (brittle or ductile), different cohesive zone formulations called traction-separation laws can be used. The

commonly used traction-separation laws are bilinear, trapezoidal, and exponential. Bilinear law is preferred in this study due to its simplicity and good accuracy, especially for brittle materials.

Figure 1.9 shows the built-in bilinear traction-separation model in ABAQUS FEA [35], exhibiting linear elastic behavior followed by linear degradation. In the figure, t^0 is the maximum traction, δ^0 is the displacement at damage initiation, δ^f is the displacement at failure, and K indicates the stiffness. Subscripts n, s, and t describe normal, shear, and transverse directions, respectively. The area under the traction-separation curve gives the fracture toughness (G_c).

For a single-mode loading, damage initiation occurs when the traction is equal to the allowable traction in that direction. The traction value is linearly dependent on the separation value, and when the area under the triangle is equal to the fracture toughness value, damage propagates.

The loading in adhesively bonded joints is often not a single load. Instead, it is a mixture of the loadings in 3 different directions, as shown in Figure 1.7. As a result, things are more complex for this type of mixed-mode loading due to the interaction between different modes of fracture.

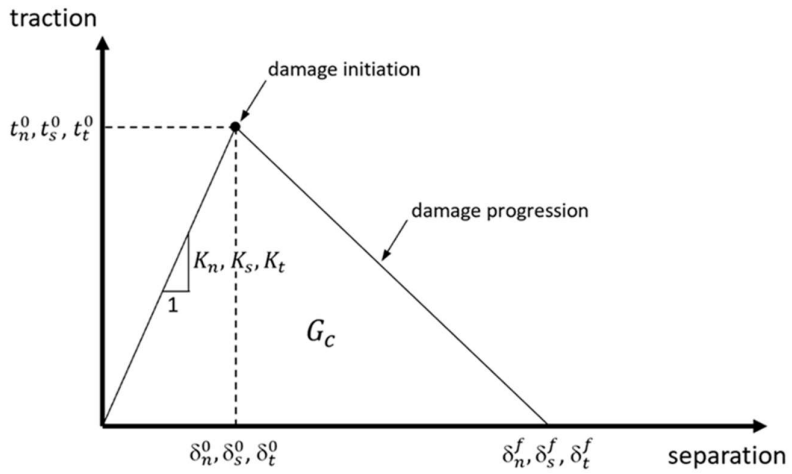

Figure 1.9. Graphical representation of the bilinear traction-separation behavior used for the modeling of the adhesive. Figure taken from ref.[35].

The uncoupled elastic behavior up to the maximum traction value is as follows.

$$\begin{Bmatrix} t_n \\ t_s \\ t_t \end{Bmatrix} = \begin{bmatrix} K_n & 0 & 0 \\ 0 & K_s & 0 \\ 0 & 0 & K_t \end{bmatrix} \begin{Bmatrix} \delta_n \\ \delta_s \\ \delta_t \end{Bmatrix} \tag{1.17}$$

For an adhesive with finite thickness;

$$K_n = \frac{E}{t} \quad \text{and} \quad K_s = K_t = \frac{G}{t} \tag{1.18}$$

In these expressions, E and G are elastic modulus and shear modulus, respectively. t is the thickness of the adhesive.

The model describes the cohesive failure in two stages, namely, initiation and progression of the damage. Damage initiation is the point where the traction reaches its maximum. This point marks the beginning of the degradation of the material properties. The damage initiation criterion can be defined through stress or strain components. This study implemented a stress-based "Quadratic Nominal Stress Criterion," a built-in tool in ABAQUS. The criterion is as follows:

$$\left\{\frac{\langle t_n \rangle}{t_n^0}\right\}^2 + \left\{\frac{t_s}{t_s^0}\right\}^2 + \left\{\frac{t_t}{t_t^0}\right\}^2 = 1 \tag{1.19}$$

where t^0 terms describe the allowable traction values, and t terms indicate current tractions. Subscripts n, s, and t correspond to the normal, shear, and transverse directions, respectively. The angle brackets imply that only positive values are considered, as normal compressive stress cannot initiate damage.

Once the damage initiates through the condition described by Eqn. (1.19), the damage progression starts. The post-damage response of the system defined according to continuum damage mechanics is as follows.

$$t_n = \begin{cases} (1-d)\bar{t_n} & \bar{t_n} \geq 0 \\ \bar{t_n} & \bar{t_n} < 0 \end{cases} \tag{1.20}$$

$$t_s = (1 - d)\bar{t_s}$$

$$t_t = (1 - d)\bar{t_t}$$

where t_n, t_s, t_t are the damaged stress states, $\bar{t_n}, \bar{t_s}, \bar{t_t}$ are the undamaged stress states in normal and shear directions, and d is the scalar damage variable taking values in the range of 0 to 1. d = 0 indicates the undamaged condition, and d = 1 indicates the fully damaged condition. To evaluate the damage progression at the presence of normal and shear deformations combined (mixed mode loading), Camanho et al. [89] defined an equivalent displacement, δ_m, as follows.

$$\delta_m = \sqrt{{\delta_n}^2 + {\delta_s}^2 + {\delta_t}^2} \tag{1.21}$$

The linear softening model defines the damage variable for mixed-mode loading in terms of this equivalent displacement as follows.

$$d = \frac{\delta_m^f \, (\delta_m - \delta_m^0)}{\delta_m \, (\delta_m^f - \delta_m^0)} \tag{1.22}$$

In this equation, δ_m is the equivalent displacement at a point. δ_m^0 and δ_m^f are the equivalent displacements at the stage of damage initiation and failure, respectively.

Eqn. (1.22) requires the calculation of δ_m^0 and δ_m^f. The equivalent damage initiation displacement, δ_m^0, can be calculated by using Eqns. (1.19), (1.21) and (1.23), and by defining a mode mixity ratio, β:

$$\delta_m^0 = \begin{cases} \delta_n^0 \delta_t^0 \sqrt{\dfrac{1 + \beta^2}{(\delta_t^0)^2 + (\beta \delta_n^0)^2}} & \delta_n > 0 \\ \sqrt{(\delta_s^0)^2 + (\delta_t^0)^2} & \delta_n \leq 0 \end{cases} \tag{1.23}$$

where,

$$\beta = \frac{\delta_{shear}}{\delta_n} \quad \text{and} \quad \delta_{shear} = \sqrt{{\delta_s}^2 + {\delta_t}^2} \tag{1.24}$$

δ_n^0, δ_s^0, and δ_t^0 in Eqn. (1.23) are the single-mode displacements at the damage initiation point, which can be written as:

$$\delta_n^0 = \frac{t_n^0}{K_n}, \quad \delta_s^0 = \frac{t_s^0}{K_s}, \quad \delta_t^0 = \frac{t_t^0}{K_t} \tag{1.25}$$

The equivalent displacement at failure, δ_m^f, depends on the softening behavior of the material, which is defined by the total area under the mixed-mode loading curve, corresponding to the equivalent fracture toughness. Benzeggagh and Kenane (B-K) [100] criterion defines the equivalent, mixed-mode fracture toughness as a function of the main modes of fracture toughness through a power-law.

$$G_{mC} = G_{IC} + (G_{IIC} - G_{IC}) \left(\frac{G_{II}+G_{III}}{G_{I}+G_{II}+G_{III}}\right)^{\eta} \tag{1.26}$$

In this equation, G_{IC} , G_{IIC}, and G_{IIIC} are the mode I, II, and III fracture toughness values, respectively. G_{mc} is the equivalent fracture toughness that governs the mixed-mode damage progression. η is the so-called B-K factor, which can be found by curve-fitting the mixed-mode bending test (MMB) data.

G_{IC} and G_{IIC} values for the adhesive can be found by double cantilever beam (DCB) tests according to ASTM D5528-13 [101] or DIN EN 6033 [102] and notched flexure tests (ENF) performed according to ASTM D7905/D7905M [103] or DIN EN 6034[104] respectively with a selected method for data reduction. G_{IIIC} can be taken same as G_{IIC}, following the general approach in the literature.

By using Eqns. (1.23), (1.25), and (1.26), and equating the area under the traction-separation curve to the fracture toughness, the equivalent displacement value at failure is determined as follows.

$$\delta_m^f = \begin{cases} \frac{2}{K\delta_m^0}\left[G_{IC} + (G_{IIC} - G_{IC})\left(\frac{\beta^2}{1+\beta^2}\right)^{\eta}\right] & \delta_n > 0 \\ \sqrt{(\delta_s^f)^2 + \left(\delta_t^f\right)^2} & \delta_n \leq 0 \end{cases} \quad (1.27)$$

The above formulations fully define the problem for the simulation of the mixed-mode behavior of the cohesive zone. The only remaining parameters are the allowable traction values t_n^0, t_s^0 and t_t^0 which can be calculated by applying inverse fitting to the numerical simulations of the DCB and ENF tests. By using the experimentally determined G_{IC} and G_{IIC}, the traction values can be adjusted such that the numerical load-displacement curve exactly matches the respective experimental curves.

1.4 Repair Parameters of Scarfed Repairs

The strength of a scarf-repaired CFRP laminate is highly dependent on the material and process parameters: scarf angle, surface pre-treatment, adherend thickness and lay-up, extra layer configuration, adhesive properties, and thickness cure conditions. These will be investigated in detail in the following sections.

1.4.1 Scarf Angle

One of the significant parameters influencing the strength of a scarf joint is the scarf angle. Many experimental and numerical studies have investigated this parameter over a range of 1.9° to 45°. Some of these studies considered 2D coupon joints [86,92,105–109], while others focused on 3D repaired parts [110–113].

Almost all studies report a common trend of decreasing strength with increasing scarf angle. The strength recovery can be as little as 10% for a scarf angle of 45° [92], whereas it can reach 84% for a scarf angle of 1.9°[111]. An optimal scarf angle satisfies the adherend failure instead of the adhesive failure, which is the desired case for all the repairs to attain the undamaged parent material strength. Although this

angle depends on the properties of the adhesive and the composite material, it is found to be less than 4° [108,112], which is in parallel what most of the SRM suggests [3,4].

Simplified 2-D models assume that all load is transferred through the adhesive bond. As a result, bypass loads passing near the repaired area are neglected. The significant consequence of this simplification tends to be an underestimation of the repair strength [108,114].

Campilho et al. [92] investigated the peel and shear distribution along the bond-line of a scarf joint using CZM methods. They showed that the peak stresses considerably diminish for the lower scarf angles, enabling higher strength values. This distribution of peel and shear stresses is shown in Figure 1.10. It is also seen that the stress concentration is higher in 0° plies which are parallel to the loading direction.

As mentioned before, the failure mode of the bonded parts mainly depends on the scarf angle. Fiber fractures and pull-out are the primary behavior for small scarf angles, whereas cohesive failure occurs within the adhesive for larger angles [92,106]. Kumar [106] showed the dependence of the failure mode to the scarf angle, as shown in Figure 1.11.

1.4.2 Surface Treatment

The preparation of the bonding surfaces plays a significant role in joint efficiency. Adhesive failure of the adhesive, which means the separation of the adhesive from the adherend surface, is a non-desired failure mode leading to low strength values. So, the bonding surfaces should be adequately pretreated to improve the performance of the bonded CFRP joints. Different pretreatment methods exist that can be classified as mechanical [115–117], chemical, plasma-based [118–120], and laser-based [121–123].

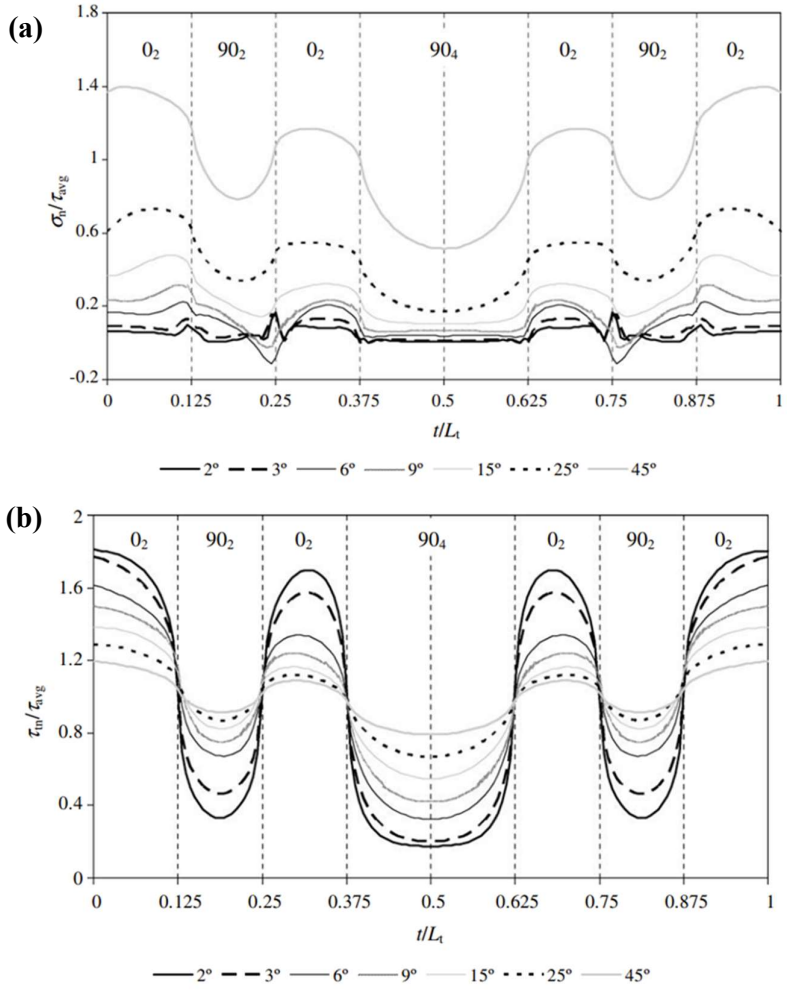

Figure 1.10. (a) Peel stress distribution in the adhesive (b) Shear stress distribution in the adhesive. Figure taken from ref. [92].

In conventional repair and bonding processes in the aeronautical industry, the primary method of surface preparation is solvent cleaning and sanding, followed by peel-ply removal. These processes aim to clean the contaminants from the bonding surface and increase the surface roughness to enhance the bonding area and mechanical interlocking of the adhesive with the substrate. The proper application of this pretreatment process is crucial for a strong and durable joint. In many cases, these processes are manual which should be performed by trained and experienced personnel.

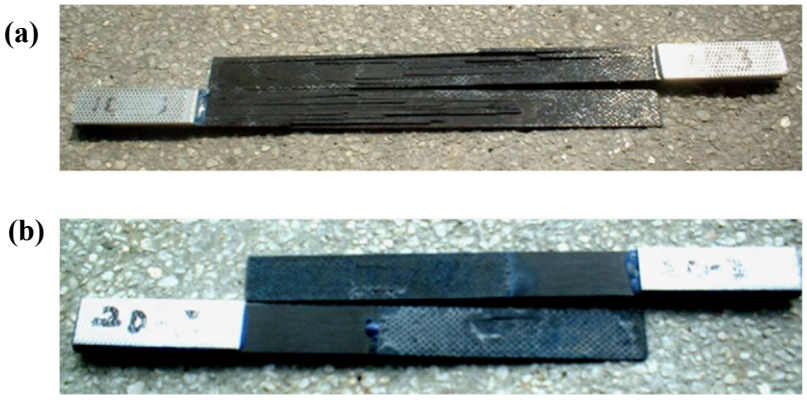

Figure 1.11. (a) Fiber fracture and fiber pull-out in the composite adherends bonded with 0.5° scarf angle (b) Cohesive failure of the adhesive for a scarf angle of 2.9°. Figure taken from ref. [106].

Yang et al. [117] investigated the effect of sanding with different grit sizes ranging between 60 to 200 on the tensile strength of the scarf and single lap joints. They concluded that sanding direction significantly affects joint strength. The randomly sanded specimen has approximately 10% higher shear strength than the unidirectional grinding in both directions, as shown in Figure 1.12.

They also concluded that there is no direct relationship between the surface roughness and the tensile strength, and an optimum value should be selected for the best performance. Kim et al. [124] also investigated the dependence of the joint strength on the surface roughness. The result shows that the mean strength of the joint increases with the increase in grit size despite the considerable variation in the test results for the smaller grit sizes.

Besides conventional mechanical and chemical treatments, many studies about surface preparation with plasma or laser techniques also exist. Infrared laser surface treatment has become of particular interest recently due to the high speed and automation of the process. Harder et al. [121] investigated the effect of laser surface treatment on the surface morphology and the overall tensile strength of the scarf

bonded specimens. The results showed a 5% increase in the bonding strength on the laser-treated specimen concerning the solvent-cleaned specimen, as shown in Figure 1.13.

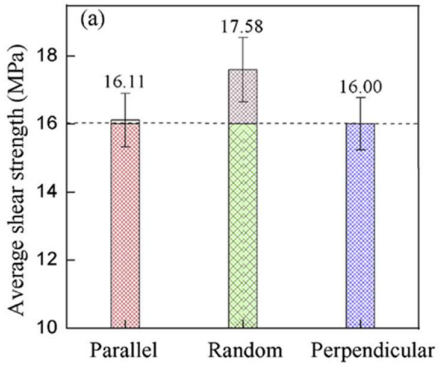

Figure 1.12. Shear strength distribution of the single lap joints with respect to the sanding direction. Figure taken from ref. [117].

1.4.3 Adherend Thickness and Lay-up

For the scarf joints between homogeneous and isotropic materials, the stress distribution along the bond-line can be assumed as uniform [125]. However, for composite adherends, the stiffness difference between the layers causes a nonuniform stress distribution and generates stress concentration sites on the plies in the load direction [66–68]. Stress concentration is especially critical for brittle adhesives, as the maximum adhesive stress rather than the average stress governs the joint strength. For most of the repairs, the aim is to match the lay-ups of the parent laminate and the repair patch to minimize the stress concentrations due to stiffness mismatch of the plies. Breitzman et al. [126] optimized the repair patch orientations to minimize von Misses stresses in the adhesive and achieved significant stress reductions and high strength recovery rates. The joint efficiency seems to be steady for scarf-bonded joints with different thicknesses, provided that they have the same lay-up sequence and curing conditions [107,127].

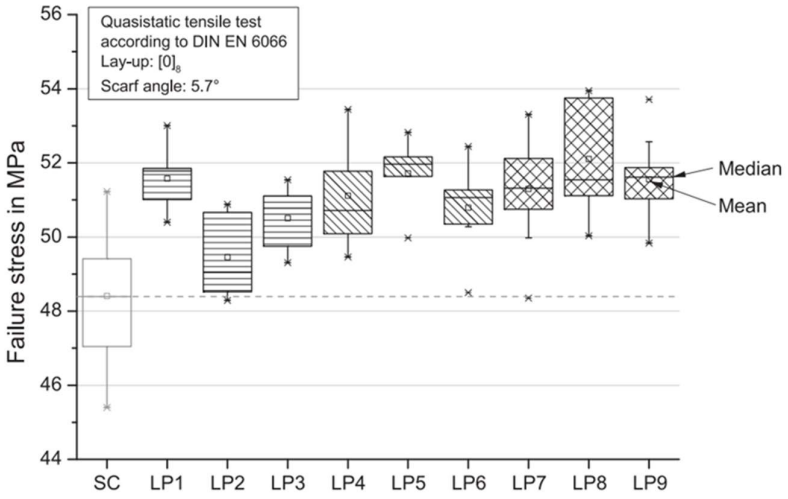

Figure 1.13. Failure stress distribution for a scarf joint with respect to different laser treatments, SC representing solvent cleaned specimen as the reference, each LP representing different infrared laser treatment parameters. Figure taken from ref. [121].

1.4.4 Effect of Extra Layer

Most of the SRMs suggest using one or more extra layers on top of the repair patch. Such practice enhances the repair, protects the patch's tips, and acts as a moisture barrier to the repair. Ahn and Springer [128] showed the influence of an extra ply on the repair strength, especially for the moisturized specimen, as shown in Figure 1.14. Feng et al. [127] investigated the effect of overlap length and the stacking sequence of the extra plies for thin structures.

As shown in Figure 1.15, the reinforcement effect of the over-plies is more evident for the thin laminates and increases as the overlap dimension increases up to a specific limit. Patches bigger than that limit have no further benefit on the repair strength. The same study also showed that the stacking sequence of the extra layers has a significant effect on the repair strength, especially for the thin laminates. [90°/ 90°] over-plies have little effect on the failure strength, whereas [0°/ 0°] over-plies enhance the strength up to 30% for the thick joints.

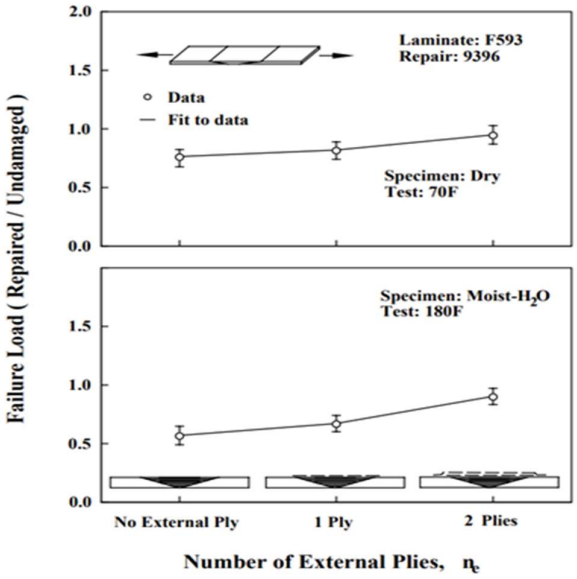

Figure 1.14. The effect of the number of extra plies on the repair strength. Figure taken from ref. [128].

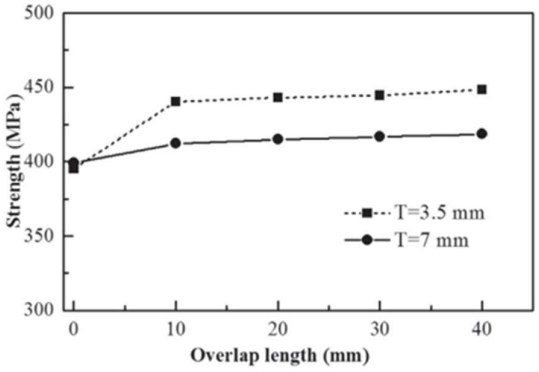

Figure 1.15. Influence of overlap dimension of the extra ply for adherend thicknesses of 3.5 mm and 7 mm. Figure taken from ref. [127].

1.4.5 Adhesive Properties

There exist various types of adhesives used in the repair of composite parts in the aerospace industry. The type and the strength of the adhesive directly affect the

strength of the repairs. Therefore, these parameters should be appropriately selected according to the repair method. The adhesives used in repairing CFRP laminates can be classified as two-part room temperature cure adhesives used in the wet lay-up repairs and film adhesives used in the elevated prepreg repairs. For a co-bonding repair process, the cure cycle of the adhesive should be compatible with the cure cycle of the repair plies to ensure flawless repairs. In addition, the ductility of the adhesive affects the failure behavior and the failure surfaces of the repairs [86].

In addition to the adhesive's strength and toughness, the other primary parameter affecting the strength of the repair is the adhesive thickness. Various studies investigated the effect of adhesive thickness on joint efficiency. Almost all these studies show that an optimum adhesive thickness value exists for the highest joint strength [105,110,129–136]. The optimum thickness of the adhesive can be selected between 0.1 and 0.5 mm for the conventional aerospace repair adhesives. However, for more ductile adhesives, the thickness might be slightly higher. For the scarf joints, as the adhesive thickness increases, the peak peel and shear stress on the bond-line also increase, leading to the premature failure of the joint, as shown in Figure 1.16 [105].

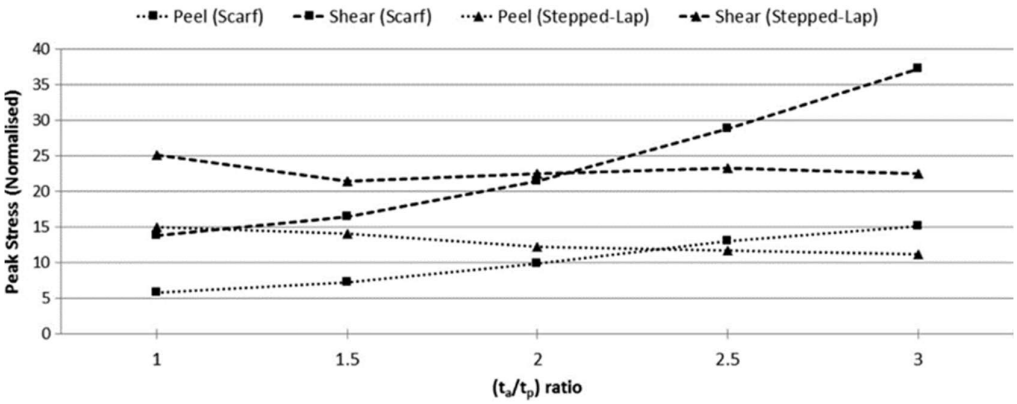

Figure 1.16. Normalized peak peel and shear stress in the adhesive bond-line (ta: adhesive thickness ranging from 0.13 mm to 0.39 mm; tp: ply thickness 0.13 mm). Figure taken from ref. [105].

1.4.6 Cure Processes

In an ideal repair, the aim is to match the repair patch's strength, stiffness, strain, and thermal properties with the original structure. However, since most of the repairs are carried out in-situ, it might not be possible to use the original materials and processes. In such cases, repair patches must be cured and bonded to the structure out of autoclave, with a vacuum bag under atmospheric pressure. For these repairs, the lack of pressure and moisture ingress due to the uncontrolled environment leads to higher porosity levels reaching 10% on the repair patch and the adhesive [137–143]. These increased porosity levels cause lower strength, especially for the interlaminar shear and compressive loadings.

Tang et al. performed mechanical tests and found that the interlaminar shear strength is affected above void contents of 4% [140]. Préau and Hubert found that every 1% increase in the bond-line porosity causes a decrease of 4.5% in tensile strength recovery [141].

1.5 Nondestructive Inspection of Repairs

Improper application of the repair processes for a CFRP laminate can lead to defects such as delamination between repair plies, de-bond on the adhesive laminate interface, porosity, excessive resin accumulation, lack of resin, and similar. So, the integrity of the repairs should be verified by proven Non-destructive Inspection (NDI) methods. The standard methods for the inspection of the repaired laminates are:

- Visual Inspection
- Tap Inspection
- Ultrasonic Inspection
- Thermography

Visual Inspection: The first step of the NDI inspection of a repair is a visual inspection all over the work area. With a careful visual inspection, one can detect surface defects such as surface cracks, surface porosities, extra bleed out of the adhesive, resin starvation on the outermost plies, wrinkling, incorrect number of plies, incorrect overlap or orientation of the extra ply, and similar. Next, further inspection methods should be selected for the internal defects.

Tap Inspection: This method can be used to detect relatively larger de-bonds or delaminations near the surface. A hammer is tapped to the surface manually or automatically. A proper bond will sound clear, whereas a defective area will sound dull. Although it is a relatively easy and cheap method, it can only detect large defects within the first few layers next to the surface, and it is highly subjective. Also, it is impractical to inspect large areas.

Ultrasonic Inspection: Ultrasonic inspection is the most common method to inspect repaired laminates. With this method, an ultrasonic signal is sent to the repaired part, and by using the refraction /reflection and attenuation properties of the sound, defects are detected. The main two techniques of ultrasonic inspection are pulse echo with a single transducer or through transmission with dual transducers. Automatic through transmission is the preferred method for inspecting the repaired parts at production facilities. The through transmission can inspect a wide area and map the existing defects within a short period; however, further characterization and depth sensing of the defects requires pulse-echo techniques. Pulse echo is the primary method to inspect the repaired parts on-site as there is no need to remove the part from the aircraft. The most distinct advantage of the ultrasonic inspection method is the capability and ability to detect porosities and sub-surface defects. The disadvantage of the ultrasonic method is that it needs high investment costs for the equipment, inspection reference panels, calibration blocks, and experienced inspectors.

Thermography: In this method, the surface temperature of the part is monitored with an infrared camera, and defects can be detected with anomalies in the temperature or phase distribution. There are different techniques of thermography

like pulse or lock-in thermography. With this method, large areas can be inspected in a short period, and numerous types of defects, including moisture ingress, can be detected. However, the shortcoming of this method is the high equipment costs, the need for skilled operators, and the method's dependence on climatic conditions.

As NDI is not the main focus of the thesis, each technique is explained very briefly. For further information, the reader can refer to the references [144–147].

All these conventional NDI methods require direct access to the structures implying grounding the aircraft. A new approach in the field is to permanently install the NDT systems to the parts, which enables online monitoring, named Structural Health Monitoring (SHM). SHM methods include different approaches discussed in detail in the literature [148–151].

1.6 Certification of Repairs

Effectivity of the bonded repairs is highly dependent on the design, processing, and workmanship. Poor repair designs or processing errors such as undesirable environmental conditions, inadequate surface preparation, improper cure conditions, degraded material properties due to bad storing conditions can lead to bond-line defects. If these defects are larger than the detectability size and can be detected with NDI methods, the repair can be rejected and reworked. However, a problem arises if the bond-line strength is reduced due to undetectable defects. These defects are more common in in-service repairs due to the less controlled environmental conditions, which cause high material property variations.

Currently, the limitations of non-destructive inspection techniques in detecting these weak bonds or the so-called kissing bonds limit composite repairs. These undetected flaws can result in inadequate bond-line strengths and unpredictable strength degradation due to environmental conditions during service. Therefore, the possible degradation of bonding strength due to weak bonds and environmental aging should also be considered in the substantiation of the repairs.

Due to mentioned shortcomings of the bonded repairs, the size of a repaired area is limited by the aviation authorities. Therefore, EASA (European Aviation Safety Agency) and FAA (Federal Aviation Administration) recommends the Fail-Safe Approach for the bonded repairs. This approach is "bonded repairs may be acceptable if sized to maintain limit load in case of repair fail" [152–154].

1.7 Objectives and Layout of the Thesis

The thesis study aims to investigate the effect of repairs on mechanical performance considering different repair materials and processes, including special on-site applications. Experimental and numerical methods followed the exact repair procedures of the aerospace industry. This approach has enabled a realistic investigation of the effect of processing and repair parameters on mechanical performance. The analysis included two types of CFRP repair processing routes: prepreg and wet lay-up, and investigated their long-term moisture and temperature durability. In addition, the study identified the correlations between the porosity levels and the repair strength.

Numerical analysis of the problem aimed to establish a reliable model that can predict the experimental behavior, which can be used for correlations for future repair scenarios with limited experimental work.

The main objectives of the thesis can be summarized as follows:

- To evaluate the effect of scarf angle on the mechanical properties of the bonded joints,
- To investigate and compare the mechanical properties and failure modes of prepreg and wet lay-up repaired CFRP laminates,
- To investigate the long-term durability of prepreg and wet lay-up repaired CFRP laminates,
- To investigate the porosity levels of the repairs with ultrasonic inspection and microscopic evaluation,

- To develop a numerical analysis methodology for predicting the mechanical performance of repairs, which then can be used to establish “knock-down” factors for design activities.

The thesis consists of 5 chapters as follows:

Chapter 1 provides a comprehensive literature review and basic information about bonded repair of composite laminates.

Chapter 2 investigates the failure behavior of scarf-bonded woven fabric composite laminates for different scarf angles. The effect of the scarf angle on the tensile strength and failure morphology is evaluated both experimentally and numerically. Also, a numerical study is performed to see the effect of porosity on the bond strength.

Chapter 3 investigates the failure behavior of stepped repaired woven fabric composite laminates for prepreg and wet lay-up repairs. Both repair methods' strength recovery and failure morphology are evaluated both experimentally and numerically. In addition, an experimental porosity evaluation is presented for selected specimens.

Chapter 4 presents the durability analysis of the prepreg and wet lay-up repairs for scarf repaired woven fabric composite laminates. The strength recovery and the failure morphology for both repair methods for the as-received and conditioned cases are evaluated experimentally. In addition, ultrasonic inspections and microscopic evaluations have provided a detailed porosity evaluation of each case.

Lastly, Chapter 5 summarizes the results and outlines future research directions.

The Appendices include the detailed experimental procedure for the fracture toughness tests, the subroutine used in the ABAQUS analysis, selective mechanical testing data, and a detailed description of the repair procedures.

CHAPTER 2

FAILURE BEHAVIOR OF SCARF-BONDED WOVEN FABRIC CFRP LAMINATES

This chapter is based on the following publication of the author: E. Sonat, S. Özerinç, Failure behavior of scarf-bonded woven fabric CFRP laminates, Composite Structures 258, 113205, 2021.

2.1 Introduction

One of the most critical parameters affecting the repair strength is the scarf angle. Most studies in the literature focusing on the scarf angle mentioned in Chapter 1 have considered unidirectional tape laminate joints. On the other hand, woven fabric structures consisting of continuous warp and weft fibers weaved in a pattern are also widely used in practice, especially in impact-prone areas of airplanes. The mechanical properties and damage behavior of fabric laminates are considerably different from unidirectional tape laminates. Therefore, the previous findings on the unidirectional laminates cannot be directly generalized to the case of fabrics, and there is a need to investigate the mechanical response of scarf-repaired woven-fabric laminates. Many researchers have reported on the micro-, meso-, and macro-scale modeling of woven-fabric materials [46,53,155,156]; however, only a few studies exist on the repair of the fabric laminates [111,157,158].

Another critical aspect of the problem is the effect of bond-line defects on the strength of the joint. Previous studies investigated this problem, emphasizing 2D defects such as delamination and debond [159–162]. However, 3D defects such as voids also considerably impact joint strength, which has remained unexplored so far.

In this part of the study, the strength of scarf-bonded woven fabric laminates under uniaxial tension is investigated, emphasizing filling the above-mentioned gaps in the literature. The effect of scarf angle on mechanical behavior is the main focus. Unlike most previous lab-scale studies, the composite manufacturing and repairs took place in an actual industrial facility and followed the aerospace industry standards in this study. This approach provided a more realistic investigation of the problem. The detailed mechanical and post-failure analyses provided insight into the relationship between the deformation modes and the scarf angle. Finite element analyses clarified the role of shear and peel stress variations over the bond area and probed the effect of bond-line defects on the strength of repaired parts.

2.2 Experimental Details

The fabrication process of the composite and its repair followed the standardized procedures for the manufacturing and repair of real aircraft panels. M21/AS4C/40RC/T2/285/6K 2×2 twill carbon/epoxy fabric prepregs with a cured ply thickness of 0.285 mm (HEXCEL PRIMETEX, Connecticut, USA) [163]were used to manufacture the composite panel with dimensions of 750 mm × 600 mm × 2.4 mm. M21 is a new generation, high-performance, very tough epoxy matrix, and its combination with the continuous, high strength, high strain AS4C carbon fabric provides excellent performance in primary aerospace structures.

The hand lay-up process employed $[45/0/-45/90]_s$, resulting in a quasi-isotropic symmetric structure. After the lay-up process, the panels were cured in an autoclave at 180°C & 7.1 bar for 9 hours (including heating and cooling periods) according to the manufacturer's requirements. After completing the cure cycle, MATEC ultrasonic tester (MA, USA) inspected the panels to verify their integrity using the Automatic Ultrasonics Through Transmission Method (AUTT). Table 2.1 gives the material properties of the composite provided by the manufacturer [163].

Table 2.1. Mechanical properties of the M21/AS4C composite provided by the manufacturer [163].

Property	Symbol	Value
Elastic Modulus (GPa)	E_{11}	61.0
	E_{22}	61.0
	E_{33}	8.9
Shear Modulus (GPa)	G_{12}	4.2
	G_{13}, G_{23}	3.8
Tensile Strength (MPa)	X_t	930
	Y_t	940
Compressive Strength (MPa)	X_c	818
	Y_c	799
Shear Strength (MPa)	S_{12}	96
	S_{13}, S_{23}	64
Poisson's ratio	ν_{12}	0.05
	ν_{13}, ν_{23}	0.3

A sawing machine cut the panels into specimens of 245 mm length and 22 mm width. Subsequent perpendicular cuts by the machine followed by manual abrasion generated the scarf joint surfaces. Figure 2.1 shows the overall geometry and dimensions of the test specimens. ASTM Standard for Tensile Testing of Polymer Matrix Composites (D3039/3039M) defined the specimen geometry [164].

Three different scarf angles (scarf ratios) are considered, namely, 1.9° (1/30), 2.8° (1/20), and 5.7° (1/10). 1.9° and 2.8° are the most common repair scarf angles in the aerospace industry.

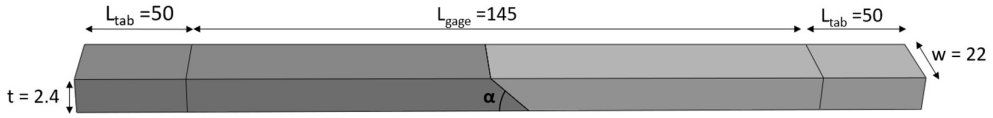

Figure 2.1. A schematic of the test specimens. Thickness and scarf angle are exaggerated for clarity. Dimensions are in mm.

The bonding steps also followed the standardized procedures for the repair of real aircraft components. First, a 120-grit diamond sander sanded the repair surfaces, followed by a water break test [165] to verify the uniformity of the sanding process. Then the parts were dried for 1 hour at 80°C in an oven to remove the water. Finally, the surfaces were wiped with acetone just before bonding.

FM-300K (Solvay, Belgium) [166], a high-strength film adhesive widely used in the aerospace industry, bonded the scarf joints. Table 2.2 shows the properties of the adhesive film provided by the manufacturer. The cohesive material parameters of the adhesive are discussed in further detail in Section 2.4 and Appendix A. A single layer of adhesive having the exact lateral dimensions as the bonding surface was applied at a thickness of 0.2 mm. An autoclave at 180°C and 3.1 bar cured the specimens according to the manufacturer's cure cycle requirements for 2 hours, including the heating and cooling periods. Upon curing, AUTT examined the bonding surface for the verification of the bond defects.

An Instron 8803 Extended Grip Servo Hydraulic Mechanical Testing Machine (MA, USA) performed the mechanical characterization of the specimens according to the ASTM Standard for Tensile Testing of Polymer Matrix Composites (D3039/3039M) [164]. The measurements employed displacement control at a rate of 1 mm/min. A mechanical extensometer provided more accurate measurements of the strain and the elastic modulus.

Table 2.2. Mechanical properties of the FM-300K adhesive [166]

Property	Symbol	Value
Tensile Modulus (GPa)	E	3.12
Shear Modulus (GPa)	G	0.9
Tensile Strength (MPa)	t_n^0	72
Shear Strength (MPa)	t_s^0 , t_t^0	42
Tensile Stiffness (N/mm3)	K_n	15600
Shear Stiffness (N/mm3)	K_s, K_t	4500
Toughness in Tension (N/mm)	G_{IC}	1.1
Toughness in Shear (N/mm)	G_{IIC}, G_{IIIC}	3.8

2.3 Experimental Results and Discussion

Figure 2.2 shows typical load-displacement curves for intact and scarf-bonded specimens with different scarf angles. The inset shows the data for all 2.8° specimens, demonstrating the repeatability of the measurements. The load-displacement curves exhibit nearly linear elastic behavior up to the point of fracture, and then the load suddenly drops, a typical feature of brittle failure. In addition, there was a cracking sound just before the fracture, indicative of the fiber failure in all tests.

Table 2.3 summarizes the average tensile strength, coefficient of variation (CoV) which is the ratio of the standard deviation to the average value, and recovery rate values for each specimen type. The tensile strength values correspond to the maximum load divided by the initial cross-sectional area of each specimen. The recovery rate is defined as follows.

$$\text{Recovery rate} = \frac{\text{tensile strength of the repaired specimen}}{\text{tensile strength of the intact specimen}} \times 100\% \qquad (2.1)$$

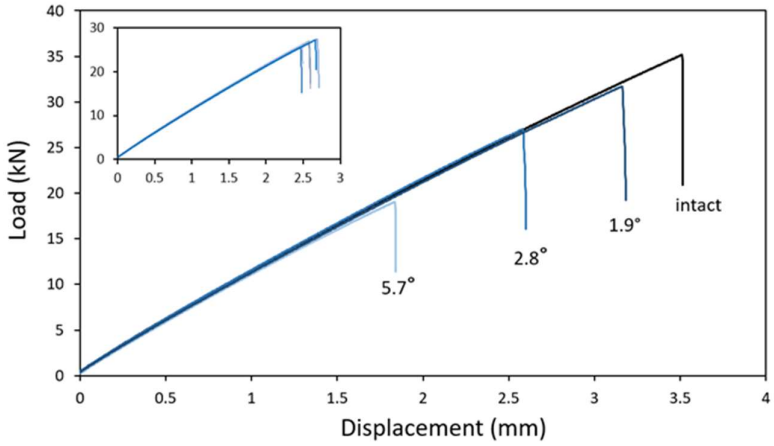

Figure 2.2. Load-displacement curves of the intact and scarf-bonded specimens. Inset shows the data for all 2.8° specimens, demonstrating the good repeatability of the tests. The inset has the same axes and units as the main plot.

Table 2.3. Tensile testing results of the intact and scarf-bonded specimens.

Scarf Angle	**Tensile Strength (MPa)**	**CoV (%)**	**Recovery Rate (%)**
Intact	662	2.4	-
1.9°	587	4.3	88.6
2.8°	530	3.3	80.0
5.7°	340	5.3	51.3

Low CoV values demonstrate the high repeatability of the results. Tensile strength monotonically increases with decreasing scarf angle. 5.7° specimens recover only about 51.3% of their intact strength, whereas 2.9° and 1.9° specimens exhibit 80.0% and 88.6% strength recovery, respectively.

Figure 2.3 shows photographs and SEM views of fractured specimens, demonstrating the typical failure types of the repaired specimens for each scarf angle.

As the scarf angle decreases, the failure type switches from joint failure to laminate failure. Three distinct failure types are present, as follows.

Type A failure: 5.7° specimens exhibit this type, where the failure is cohesive; that is, the fracture takes place within the adhesive. As the adhesive layer mediates the fracture, the failure takes place at the joint. The SEM image of the joint area in Figure 2.3 (a) shows no fiber failure, further confirming the type of failure.

Type B failure: 2.8° specimens exhibit this type, where the failure is a combination of laminate failure and cohesive failure. The laminate failure took place at the joint area. The SEM image in Figure 2.3 (b) shows the failure of the 0° and 45° fibers in detail.

Type C failure: 1.9° specimens exhibit this type, where failure has the appearance of a pull-out fracture, a typical failure type for intact laminates. The failure occurred near the end of the joint, with the fracture surface mainly being perpendicular to the loading axis. No adhesive failure is present on the failure surface.

Commercial aircraft manufacturers recommend a maximum scarf angle of 2.8° for composite laminate repair[3,4]. The experimental findings provide insight into this recommendation; for larger angles, the strength of the repaired composite dramatically decreases. The average shear stress over the bonding area can be written as follows [125]:

$$\tau_{bond,ave} = \frac{1}{2}\sigma^{\infty} \sin 2\alpha \tag{2.2}$$

where σ^{∞} is the far-field tensile stress, and α is the scarf angle. One can substitute the experimentally measured tensile strength values of Table 2.3 in Eqn. (2.2) and determine the shear stress over the bond area at the point of failure. This calculation provides stress values of 33.6 MPa, 25.8 MPa, and 19.5 MPa for scarf angles of 5.7°, 2.8°, and 1.9°, respectively.

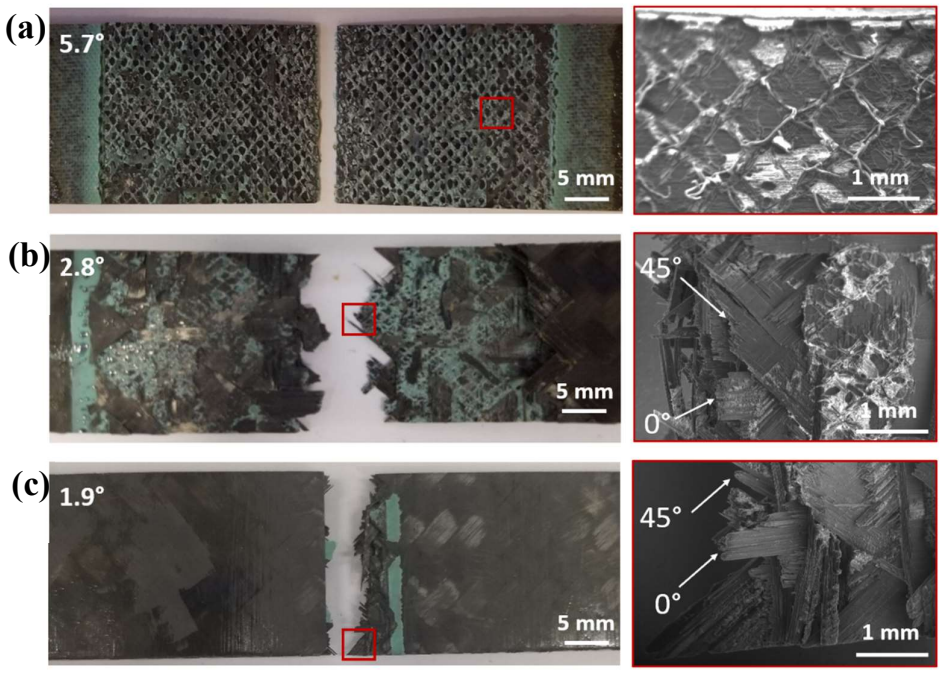

Figure 2.3. Photographs and SEM views of the fracture surfaces of representative test specimens. (a) Cohesive failure of a 5.7° specimen. (b) Cohesive failure + intra-laminar failure of a 2.8° specimen with detail showing the fiber breakages in 0° and 45° fibers (c) pull out fracture of a 1.9° specimen with detail showing the fiber breakages in 0° and 45° fibers. Specimen pieces on the right-hand side are flipped to reveal the failure surfaces more clearly.

5.7° specimens exhibit cohesive failure, and as a result, the corresponding $\tau_{bond,ave}$ (33.6 MPa) is closer to the manufacturer-specified shear strength of the adhesive (τ_y = 42 MPa). The shear stresses in the 2.8° and 1.9° specimens at the point of failure, on the other hand, are considerably lower than the shear strength of the adhesive, in agreement with the involvement of composite failure observed for these angles.

The ideal tensile strength of the repaired specimen may be defined as the strength limited by the cohesive failure of the adhesive. Then the ideal strength is a function

of the adhesive yield strength, τ_y and by assuming uniform stress distribution over the joint:

$$\sigma_{f,ideal} = \frac{2\tau_y}{\sin 2\alpha} \tag{2.3}$$

The uniform stress distribution assumption is valid for scarf joints between homogeneous and isotropic materials [5,108,125]. However, for composite adherends, the stiffness difference between the layers causes a nonuniform stress distribution and generates stress concentration sites[66–68]. Stress concentration is especially critical for brittle adhesives, as the maximum adhesive stress governs the joint strength, not the average stress. Therefore, Eqn. (2.3) may be revised to take the effect of stress concentration into account:

$$\sigma_{f,actual} = \frac{2\tau_y}{K_{s,max}\sin 2\alpha} \tag{2.4}$$

where $K_{s,max}$ is the maximum shear stress concentration factor over the bonding area.

For a scarf angle of 5.7° Eqn. (2.4) indicates a maximum stress concentration factor of 1.25 based on experimentally measured σ_f and τ_y. Stress concentration factors are usually reported in the literature for unidirectional (UD) laminates and can reach values as high as 2.8 due to the strong anisotropy in these composites [108,167].

The stress concentration factor depends on the material, stacking sequence, and laminate thickness [67]. Baker [150] suggests the following first-order approximation for predicting the stress concentration factor, neglecting the shear-lag effect of the adhesive and the stacking sequence & thickness.

$$K_s = \frac{n_{total}}{n_0 + n_{\mp 45}\frac{E_{\mp 45}}{E_0} + n_{90}\frac{E_{90}}{E_0}} \tag{2.5}$$

Where n is the number of plies, and E is the elastic modulus. The subscripts refer to the property of the laminate in the associated direction. For the used quasi-isotropic

woven laminate, Eqn. (2.5) predicts a stress concentration factor of 1.6. The discrepancy between this prediction and the experimental prediction of 1.25 above is probably because Baker's approach does not consider any plasticity, which overestimates the severity of stress concentration. In the numerical section, stress concentration factors will be investigated further in detail through finite element modeling.

The results show that a sufficiently small scarf angle can ensure that the bonding region is stronger than the composite under pure tension. However, such small scarf angles require a large amount of material removal from the undamaged regions of the part. The associated bonding area also becomes large, leading to undesirable weakening of the structure, especially under complicated loading scenarios. In addition, for very small scarf angles, the tip regions of the adherends tend to break off, which limits the overall strength of the repair. Therefore, the scarf angle should be small enough to minimize the peel & shear stresses acting on the bonding area and should be large enough to avoid the problems mentioned above. The geometrical restrictions in actual repair processes might add further limitations to the minimum scarf angle. For example, 1.9° repairs have approximately 50% larger bonding area than the 2.8° case. The corresponding strength recovery is only 9% higher, which indicates the need for careful optimization of the scarf angle.

The investigation of the fracture types can guide the optimization of the problem. For large scarf angles, the adhesive carries a significant portion of the tensile load, leading to premature failure through the joint, regardless of the strength of the parent material. On the other hand, for small angles, the failure is governed by the strength of the parent material, and further reductions in the angle have only a minor influence on the overall strength of the repaired part. By rearranging Eqns. (2.3) and (2.4) the optimum scarf angle α can be written as:

$$\propto_{\mathrm{opt}} = \frac{1}{2}\sin^{-1}\left(\frac{2\tau_{\mathrm{y}}}{K_s\sigma_{\mathrm{f}}}\right) \tag{2.6}$$

where (σ_{f}) is the tensile strength of the intact specimen.

Using the experimentally determined K_s and σ_f values, $\propto_{opt} = 2.9°$ is found for the composite and the adhesive under investigation. This angle represents the optimum scarf angle at which the adherend and the adhesive load-carrying capacity are the same for the tensile testing conditions. Fracture types demonstrated in Figure 2.3 support the validity of this simple calculation. 2.8° specimens exhibit simultaneous cohesive failure and fiber breakage whereas 1.9° specimens exhibit pull-out fracture. The latter indicates that the adequate strength of the repair surface exceeds that of the intact laminate. Finally, adhesive thickness is also critical for achieving the desired joint strength, as mentioned in Chapter 1. Figure 2.4 shows a polished side-view of a 5.7° specimen. The thickness of the adhesive varies between 0.15 – 0.20 mm in this joint, which is within recommended limits.

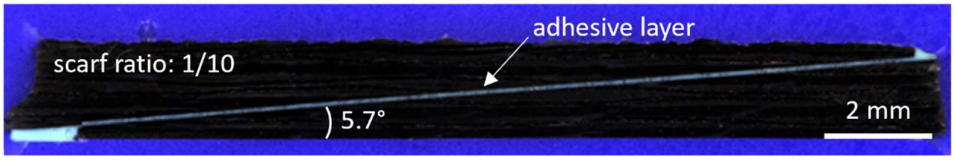

Figure 2.4. Optical microscope side view of a 5.7° specimen.

2.4 Modeling Methodology

The tensile testing of the scarf-bonded specimens is modeled by finite element method using ABAQUS 6.14 Standard. Figure 2.5(a) shows a schematic side view of the model and its boundary conditions. A fixed boundary condition at one end and a linear displacement boundary condition at the other end provided the tensile test conditions. The model's size was the same as that of the actual specimens; the only difference was the omission of the grip regions of the actual specimens to reduce the computational load. It is verified that modeling with and without these grip regions yields virtually identical results. The material properties used for the composite adherend and the adhesive are summarized in Table 2.1 and Table 2.2. The two parts of the composite have an offset in the z-direction, corresponding to the thickness of

the adhesive. This geometry enables the representation of an offset present in the actual specimens occurring due to the nature of the repair process (see Figure 2.4).

Figure 2.5 (b) shows the details of the mesh structure. 3D solid elements discretized the composite adherends. These were 8-node hexahedral C3D8R elements, except 6-node triangular prism (C3D6) elements used for the scarf tips. The $[45/0/-45/90]_s$ lay-up was implemented in the model by identifying each layer's material, thickness, and orientation. Eight-node 3D cohesive elements (COH3D8) discretized the adhesive layer. After performing a mesh sensitivity study for the composite adherend, it is verified that 0.6 mm is a sufficiently small element size to avoid snap-back in the damage modeling. The resulting optimized mesh starts with a size of 1.5 mm far away from the joint and gradually becomes 0.6 mm near the joint region to capture the damage progression behavior. Therefore, next to the joint, the elements of the adherends are selected as 0.6 mm x 0.6 mm x 0.3 mm. For the cohesive elements, element sizes in the range of 0.2 – 0.8 mm are considered, and selected the optimum cohesive element size as 0.3 mm × 0.3 mm × 0.2 mm. Tie constraints connected the mismatching nodes at the adherend-adhesive interface, assuming perfect bonding.

2.4.1 Failure and Damage Progression of the Laminate

Under tension, inter-laminar failure is less likely as there is no out-of-plane loading on the layer interfaces, so only intra-laminar damage is evaluated in this thesis. A progressive failure model that simulates the ply-by-ply gradual failure of the composite is implemented with the ABAQUS user subroutine, USDFLD, given in Appendix B. The damage initiation and progression models will be explained in detail here.

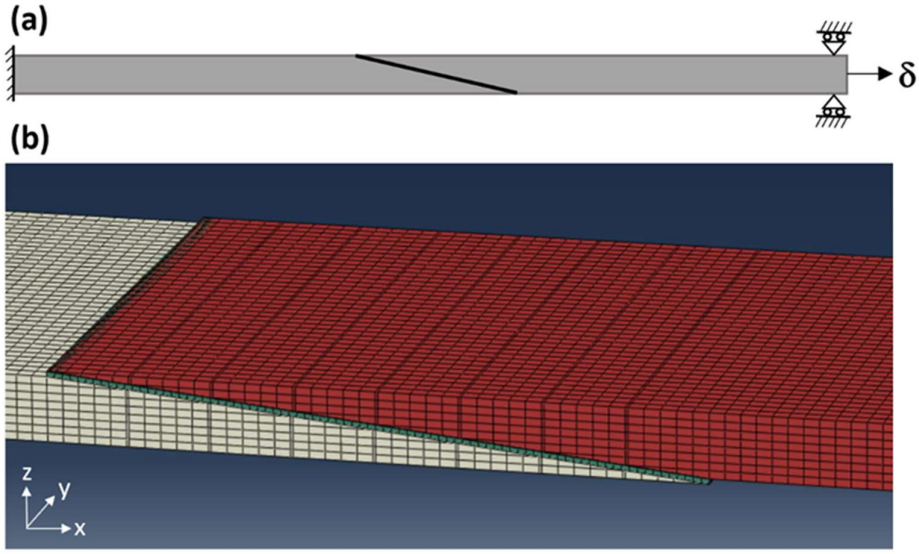

Figure 2.5. (a) Schematic description of the finite element model. (b) Close-up view of the mesh structure around the scarf.

Damage initiation: Damage initiation models are explained in detail in Chapter 1. Hashin Failure theorem is used to model the damage initiation. Since woven fabric where the fibers support the load in two orthogonal directions (0° and 90°) is used in this study, the formulation differs from Eqn. (1.7) to (1.10). Matrix damage is not a primary failure mode in woven fabric composites, and therefore, the user-defined code only considers fiber failure in warp and weft directions. Due to the symmetrical nature of the fabric, the criteria for the warp and weft directions are identical. This modified form of the 3D Hashin model is as follows.

Fiber Tension Failure Mode in Warp Direction ($\sigma_{11} > 0$):

$$\left(\frac{\sigma_{11}}{X_t}\right)^2 + \left(\frac{\tau_{12}}{S_{12}}\right)^2 + \left(\frac{\tau_{13}}{S_{13}}\right)^2 \geq 1 \tag{2.7}$$

Fiber Compression Failure Mode in Warp Direction ($\sigma_{11} < 0$):

$$\left(\frac{\sigma_{11}}{X_c}\right)^2 \geq 1 \tag{2.8}$$

Fiber Tension Failure Mode in Weft Direction ($\sigma_{22} > 0$):

$$\left(\frac{\sigma_{22}}{Y_t}\right)^2 + \left(\frac{\tau_{12}}{S_{12}}\right)^2 + \left(\frac{\tau_{23}}{S_{23}}\right)^2 \geq 1 \tag{2.9}$$

Fiber Compression Failure Mode in Weft Direction ($\sigma_{22} < 0$):

$$\left(\frac{\sigma_{22}}{Y_c}\right)^2 \geq 1 \tag{2.10}$$

In these equations, 1 is the warp direction, 2 is the weft direction, and 3 is the out-of-plane direction. Therefore, σ_{11} and σ_{22} are the stress components along the warp and the weft directions, respectively, and τ_{12}, τ_{23}, and τ_{13} are the corresponding shear stresses. X and Y denote the composite material allowable strength in the warp and weft directions, respectively. The subscripts in these terms, t and c, represent the tension and compression, respectively. Finally, S_{12}, S_{23}, and S_{13} denote the allowable shear strengths in the three planes.

Damage progression: In this study, the instantaneous degradation model is used for damage progression. The selection of a non-zero degradation factor ($\alpha = 10^{-4}$) prevented numerical convergence problems caused by the instantaneous local changes in the stiffness. Table 2.4 summarizes the details of the degradation scheme for each failure mode, where subscript d shows the resultant material property after degradation takes place.

Table 2.4.Degradation parameters for the progressive failure of the composite structure.

Degraded Parameter	E_{11d}	E_{22d}	G_{12d}	G_{13d}	G_{23d}	ν_{12d}	ν_{13d}	ν_{23d}
Fiber Failure in Warp Direction	αE_{11}	E_{22}	αG_{12}	αG_{13}	G_{23}	$\alpha\nu_{12}$	$\alpha\nu_{13}$	ν_{23}
Fiber Failure in Weft Direction	E_{11}	αE_{22}	αG_{12}	G_{13}	αG_{23}	$\alpha\nu_{12}$	ν_{13}	$\alpha\nu_{23}$

2.4.2 Failure and Damage Progression of the Adhesive

A bilinear traction-separation mixed-mode cohesive law, which the details are given in Chapter 1, modeled the mechanical behavior of the bond. The model used cohesive elements instead of surface interaction. This choice has two main advantages:

1. Provides direct control on the mesh size and adhesive properties.
2. Enables a detailed and realistic model of the adhesive by taking its finite thickness into account.

The selection of the appropriate element size for the CZM is critical for capturing the damage progression correctly and ensuring the convergence of the numerical solution. The key parameter here is the minimum number of elements along the length of the cohesive zone, N_e, required to capture the continuum field of the crack.

$$N_e = \frac{l_{cz}}{l_e} \tag{2.11}$$

Where l_{cz} is the length of the cohesive zone, defined as the distance from the crack tip to the point of maximum traction, and l_e is the element size. l_{cz} can be estimated as follows [168].

$$l_{cz} = ME\frac{G_c}{(t^0)^2} \quad (2.12)$$

where E is the modulus, and G_c is the fracture toughness of the adhesive in the relevant mode. t^0 is the traction for each mode, and M is a parameter that depends on the model. M is taken as one by following the approach of Turon [168] and Hillerborg [85] and take N_e as 3, as suggested by Davila and Camanho [90]. Substituting for the remaining parameters of the adhesive, the minimum cohesive zone length (l_{cz}) is found as of 1.2 mm considering each mode. Then the maximum mesh size, l_e is 0.4. In the model, a cohesive element length of 0.3 mm is used to capture the damage progression and facilitate the convergence.

The fracture toughness values G_{IC} and G_{IIC}Data obtained from DCB and ENF tests (details in Appendix A) are taken from Table 2.2. G_{IIIC} is taken the same as G_{IIC}, following the general approach in the literature.

Using bulk adhesive properties gives approximate results for the traction (strength) values used in CZM modeling. This is due to the difference in the adhesive's crack formation and propagation behavior, whether it is thin and constrained between stiffer adherends or the bulk form. In this study, an inverse fitting technique is used to find the traction values of the adhesives. The experimentally found G_{IC} and G_{IIC} values are used to iteratively find the traction values in a numerical model of these fracture tests. The traction values are adjusted such that the numerical and experimental load-displacement curves match. As a starting point, the lap shear strength data in the material datasheet of FM-300K is taken as the allowable traction value. Benzeggagh and Kenane (B-K) factor η, given in Eqn. 1.26 is taken as 2.3, the value used for FM-300M, a similar type of adhesive[169,170].

2.5 Modeling Results and Discussion

Figure 2.6 shows a comparison of the experimental and numerical load-displacement curves for each scarf angle. The results show that the finite element model can closely predict the actual load-displacement behavior. The simulation also captures

the sudden failure behavior well. Figure 2.7 compares the simulation predictions with the experimental results in terms of the failure load. The differences between the experimental and the modeling results are within 10%. Simulations slightly overpredict the failure load, and the overprediction is higher for smaller scarf angles. The trend in the overprediction suggests that the differences are due to the increasing likelihood of defects and surface irregularities in the manufacturing of small-angle scarfs. As the number of defects and surface irregularities increase, the experimentally measured strength decreases.

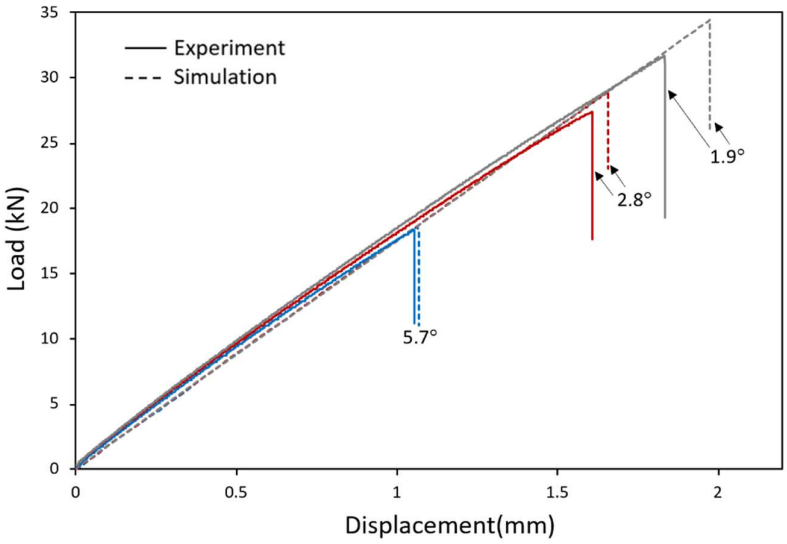

Figure 2.6. Experimental and numerical load-displacement curves for the specimens with three different scarf angles. The experimental displacement measurements correspond to the extensometer data.

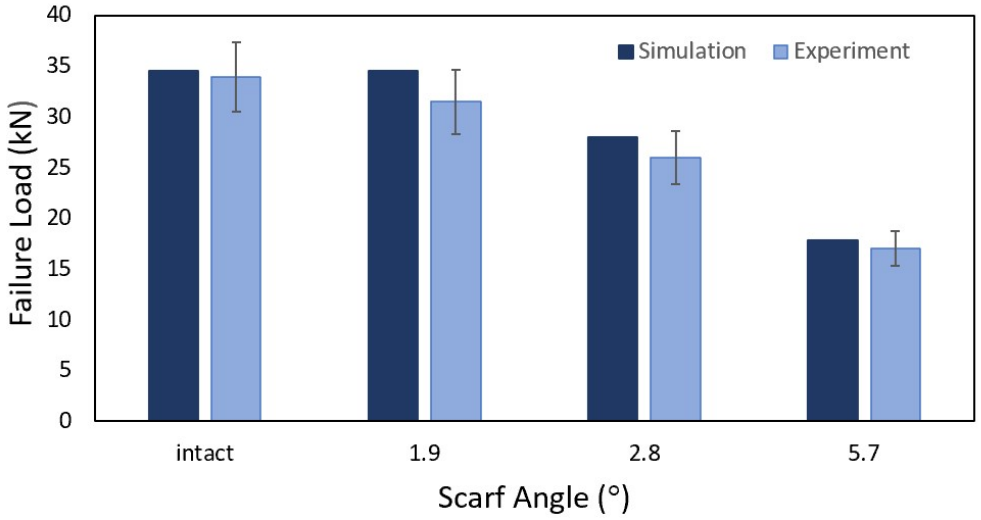

Figure 2.7. Failure load values for intact and scarf specimens, as determined by experiments and as predicted by simulations.

One can obtain further insight into the problem by investigating the stress variations in the joint region. Figure 2.8 shows the normalized shear & peel stresses and associated local stress concentration factors, K_s and K_n, over the bonding area for different scarf angles. The far-field tensile stress (σ_∞) is 270 MPa in each case, corresponding to an undamaged condition of the specimen. The stress distributions do not vary significantly over the specimen width except for variations at the edges. Therefore, the plateau values around the center of the specimen are used for plotting purposes.

Figure 2.8 (b) and (c) shows the variation of shear stress and peel stress, both normalized by σ_∞. The normalized stresses considerably increase with scarf angle. In addition, the stress distributions exhibit significant variations through the thickness of each layer. The normalized peel stress rises sharply towards the edges. This rise is due to the additional bending of the adherend induced by the load eccentricity in the scarf geometry described at the beginning of Section 2.4. Although normalized stress becomes quite large towards the edges, the absolute peel stress remains below the strength of the adhesive due to the small scarf angles employed.

Figure 2.8 (d) shows the variation of the shear stress concentration factor, K_s, over the length of the scarf. The behavior is virtually independent of the scarf angle and exhibits symmetry around the 0° – 0° interface due to the symmetric nature of the lay-up. The maximum stress concentration factor is 1.5, which occurs within the 0°-plies. This result is in relatively good agreement with the experimentally determined values around 1.3 (see Section 2.3), considering all the approximations and uncertainties in the experiments and the modeling.

Figure 2.8 (e) shows the peel stress concentration factor, $K_{n,}$ over the length of the scarf. While this factor is of secondary importance compared to K_s in affecting the fracture behavior, it still provides insight into the problem. Similar to K_s, the variation of K_n exhibits symmetry, and it is mostly independent of the scarf angle. Due to the previously discussed bending effects, K_n rises towards the edges, reaching almost 7.

The high-stress concentration within the 0°-plies is a manifestation of the anisotropic nature of the composite. The laminate's stiffness depends on the lay-up and varies along the scarf length, whereas the adhesive stiffness is uniform. Consequently, 0° plies are the ones experiencing the highest adherent-adhesive stiffness mismatch, which is the primary source of stress concentration.

Figure 2.9 presents the damage condition of the bonding area in terms of adhesive and fiber damage for each scarf angle, which highlights the dominant modes of failure. The damage parameters presented are adhesive damage (SDEG), fiber damage in the warp direction (FV1), and fiber damage in the weft direction (FV2). The color maps show the results corresponding to 99% of the ultimate load for each scarf angle. A value of zero corresponds to the undamaged state, and 1 indicates complete failure. FV1 and FV2 can only take 0 or 1, whereas SDEG can have intermediate values due to the progressive nature of its modeling.

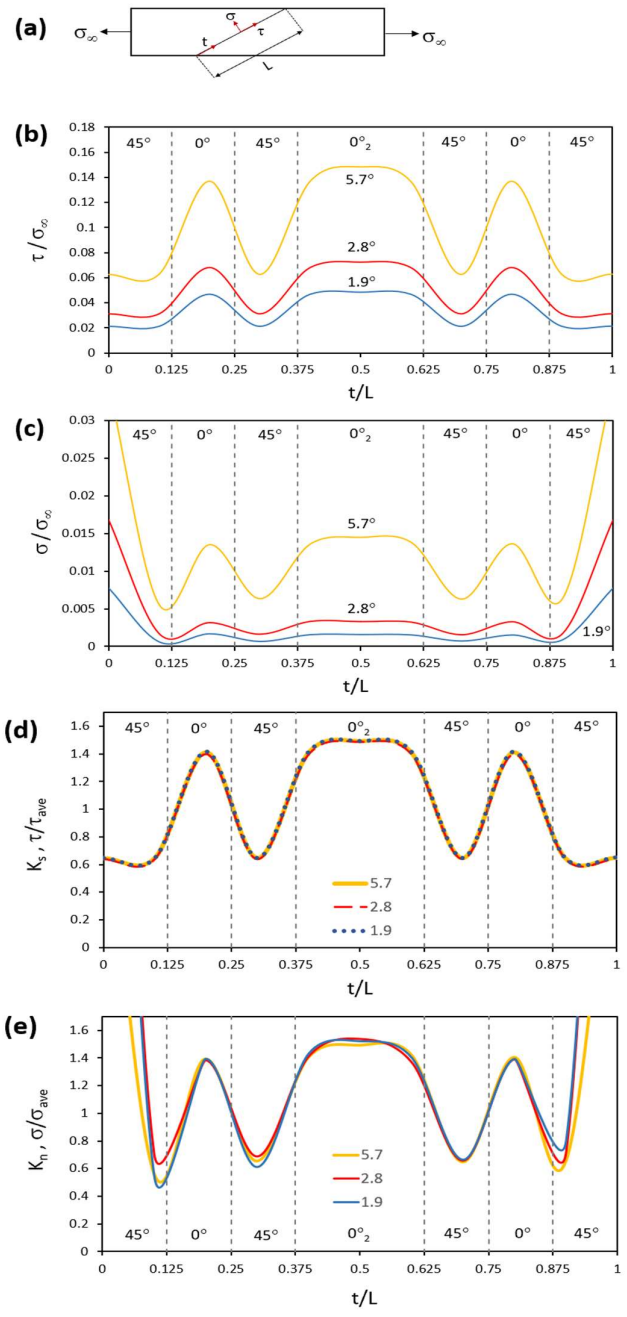

Figure 2.8.Schematic describing the definitions of the stress components and the coordinate frame. (b) Normalized shear stress distribution. (c) Normalized peel stress distribution. (d) Shear stress concentration distribution. (e) Peel stress concentration distribution.

2.8° specimen exhibits cohesive failure accompanied with some fiber failure in both warp and weft directions, in other words, a mixed-mode failure. SDEG color plot shows that the cohesive failure begins from the side edges of the 0°-plies, similar to that of 5.7° specimens. However, unlike the 5.7° case, fiber failure starts before the cohesive failure spreads to the whole bond area, as seen in the associated FV1 and FV2 plots. The fiber failure in the warp direction starts within the 0°-plies, whereas in the weft direction, the fiber failure starts in the neighboring 45° layers. The presence of fiber failure before complete failure is consistent with the cracking sounds just before the failure during the experimental tests.

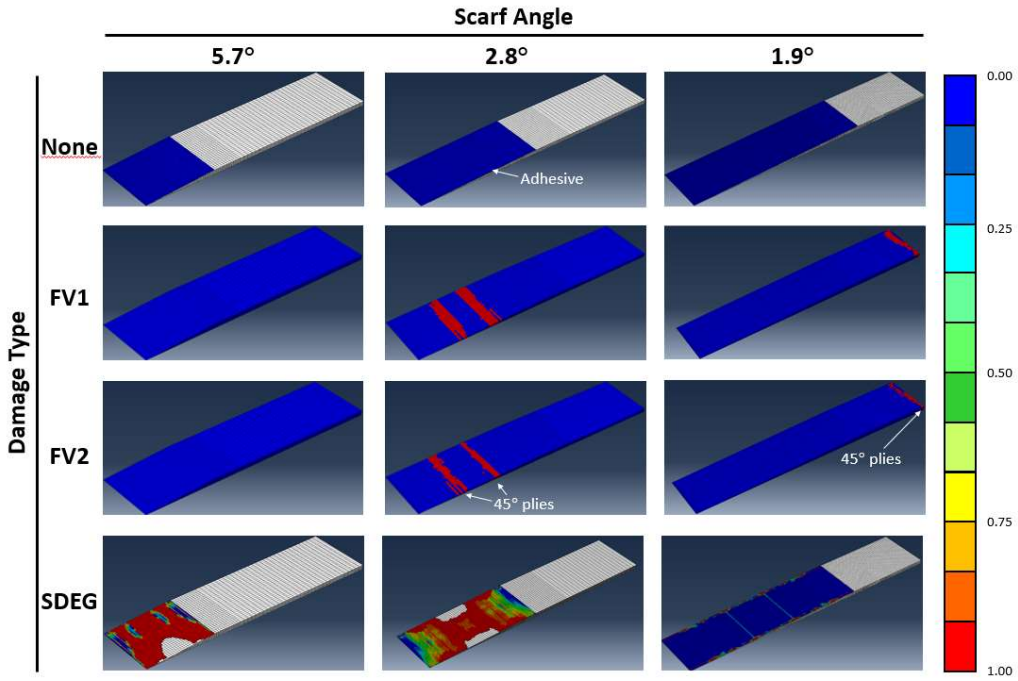

Figure 2.9. Color maps of the damage states of the bond area for each scarf angle. All maps correspond to 99% of the ultimate loading. 0 is undamaged, and 1 is fully damaged. In SDEG plots, white regions within the bonding area correspond to complete cohesive failure. The top row shows the geometry before loading, where the blue color represents the adhesive. FV1: Fiber failure in the warp direction, FV2: Fiber failure in the weft direction, SDEG: Adhesive failure.

1.9° specimens show intralaminar fiber failure without any cohesive failure, consistent with the experimental findings. Slight degradation of the adhesive is present at the edges of the joint area; however, fiber failure takes place outside the bonding region before any considerable cohesive damage occurs. All layers except 45° ones fail in the warp direction, whereas 45° layers show failure in both directions. The failure took place next to the bond-line in the experiments. In the simulations, failure occurred at the edge of the domain, corresponding to the grip region in the experiments. In the experiments, the bond-line defects or minor geometrical deviations might be responsible for the observed behavior. On the other hand, in the simulations, the stress concentrations at the edges of the domain are likely to promote failure.

2.6 Defect Evaluation

Two separate batches for the 2.8° scarf angle case have been prepared and tested due to unexpectedly high porosity levels in the first batch. These two batches allowed us to assess the effect of bonding defects on mechanical strength. Figure 2.10 shows the cross-sections of representative specimens from each batch. The specimen from the first batch has various bond-line defects with dimensions in the range of 0.1 – 0.5 mm. A simple calculation based on the image suggests an overall porosity of about 10% over the bond area. In addition, the average failure load for this batch (24 kN) is 13% lower than that of the second batch with no defects (28 kN), which agrees with the predicted porosity.

A numerical analysis is performed to obtain a more systematic understanding of the effect of defects on the static strength of the scarf joints. The details of the modeling approach are the same as those described in Section 2.4. 5.7° scarf angle is focused on, in which the failure of the adhesive dominates the response. The analysis investigated two prominent cases, namely, isolated large defects (single-void) and distribution of small defects (porous structure). Figure 2.11 shows a total of 8 different defect scenarios – four cases of different void sizes and four cases of

different porosity levels. In each case, the defects are modeled by merely removing the adhesive from the associated regions.

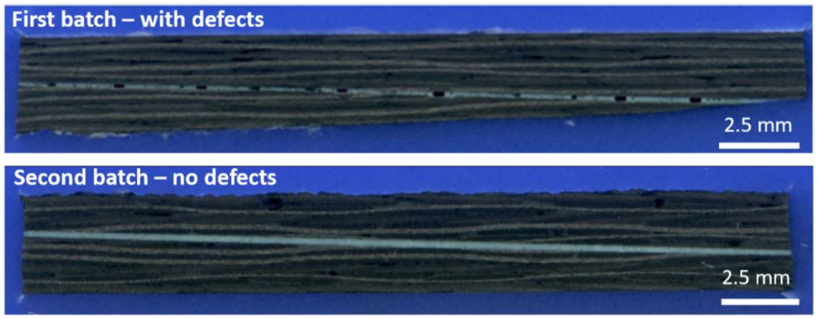

Figure 2.10. Cross-section photographs of 2.8° specimens, showing example bond-lines with and without defects.

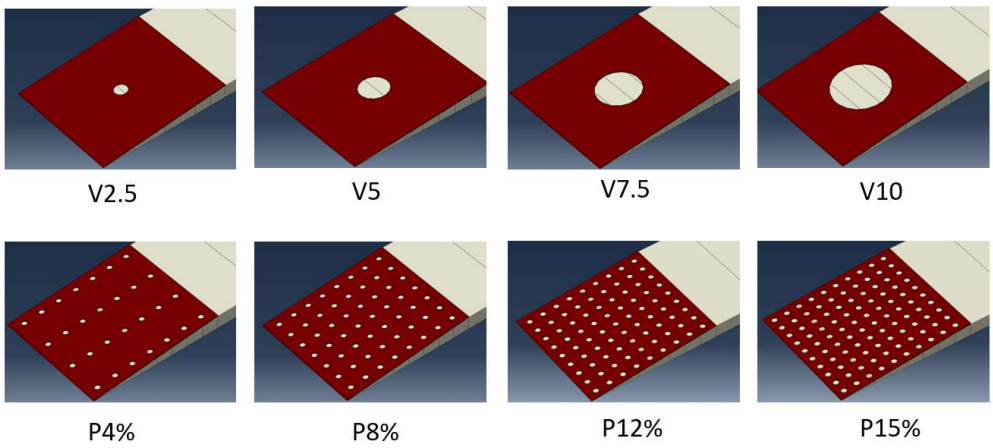

Figure 2.11 Modeling geometry for the investigation of bond defects on the mechanical response. V refers to single-void samples, where the number indicates the size of the void in mm. P refers to the distributed pore scenario with a constant pore diameter of 1 mm. The percentage indicates the total percent area loss due to the presence of the pores.

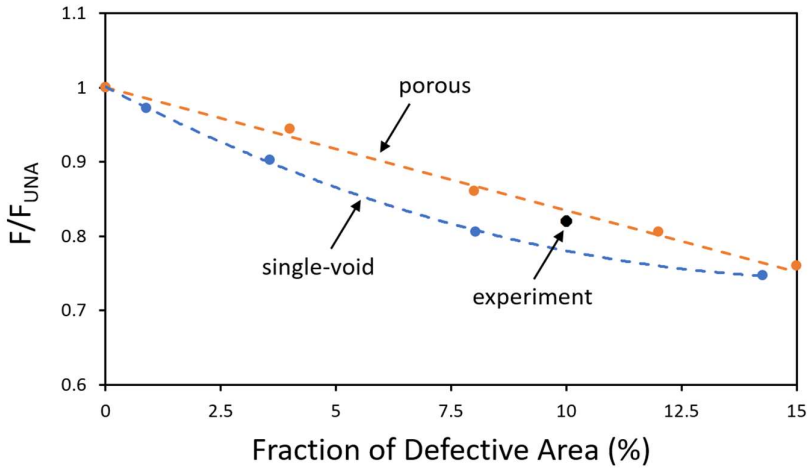

Figure 2.12. Variation of the normalized load of failure with the fraction of defective area in the adhesive. The colored markers indicate simulation results, and the single black marker indicates the experimental data. Dashed lines are provided as a guide to the eye.

Figure 2.12 summarizes the results in terms of the normalized failure load vs. defect area percentage. The data show a monotonic decrease in the load-carrying capacity with increasing defect area for both the single-void and porous structure cases. The porous structure shows a slightly higher load-carrying capacity for a given amount of defective area fraction than the single-void case. Experimental data with an estimated defect fraction of 10% agree well with the simulation predictions, where the failure load is normalized by the experimentally measured failure load of the defect-free specimens.

In airplanes, a total porosity of 4% is usually the repair limit [4,73]. The simulation results show that the associated reduction in the load-carrying capacity is less than 10%. On the other hand, when the defect fraction is 8%, the associated load drop can reach 20%, which starts to present a significant risk on the reliable operation of the structural component

2.7 Conclusions

The experimental measurements on scarf-bonded specimens with different scarf angles showed that the repair strength increases as the scarf angle decreases, and there exist three failure types of mechanical response. For the scarf angle of 5.7°, cohesive failure occurs within the adhesive, whereas for 1.9°, the laminate structure fails without considerable damage in the bond area. The scarf angle of 2.8° exhibited a mixed response – a combination of laminate failure and cohesive failure. The finite element analysis provided further insight into the problem and showed that stress concentration plays a vital role in the failure behavior of the specimens. The most critical region of the bond area corresponds to the 0°-plies, where the adhesive-adherent stiffness mismatch is highest. Analysis of the bond-line defects showed that a defect density of about 10% reduces the tensile strength by almost 20%, demonstrating the importance of the repair quality in achieving desirable mechanical performance.

.

CHAPTER 3

FAILURE BEHAVIOR OF ON-SITE REPAIRED WOVEN FABRIC COMPOSITES

3.1 Introduction

On-site repair processes can become challenging due to various limitations. First of all, an autoclave cannot be used, and as a result, pressurized curing is no longer an option. Secondly, in some cases, the curing temperature becomes limited by adjacent components that can get damaged at high temperatures. These limitations implement satisfactory repairs challenging, and the resulting repaired zones often have lower strength than ideal repairs.

The primary motivation of the study presented in this section was to fill the gap in the literature about the effects of on-site repair conditions on mechanical performance. Towards this objective, the strength of stepped repaired composite laminates was investigated. The study considered two different repair processes, namely, wet lay-up and prepreg. For prepreg repairs, the curing was performed out of autoclave intentionally to investigate the efficiency of on-site repairs. On the wet lay-up repairs, a low-temperature curing paste adhesive was used to bond the repair patch, which simulated conditions where high temperatures could not be utilized.

3.2 Experimental Details

The parent composite panels were fabricated from M21/AS4C carbon/epoxy fabric prepregs, as described in detail in Chapter 2. A sawing machine cut the panels into specimens of 350 mm length and 150 mm width. To simulate the damage, 18 mm diameter holes were drilled at the center of the panels. Three of these drilled panels were tested without any repair to quantify the strength of the damaged laminate.

Figure 3.1 shows a schematic of the repair geometry. A three-axis milling machine prepared the step geometry with 6.25 mm steps on the parent laminate to minimize the experimental scatter that can be a manual operation. Before the bonding process, 120 grit sandpaper abraded the surfaces. Water break tests on the bonding surfaces, followed by drying for 1 hour at 80°C, verified the uniformity of the sanding according to ASTM F22-13 Standard Test Method for Hydrophobic Surface Films [165]. Three of the stepped panels were tested to determine the tensile strength before repair. The prepreg and wet lay-up repair applications followed the general procedures given in the structural repair manuals, as follows [3,4].

Wet lay-up repair: Hexforce G0904 D 1070 TCT plain weave dry carbon fabric was wetted with low-temperature cure laminating adhesive HYSOL EA 9396. The dry carbon fabric, impregnated with the adhesive with a 1/3 weight ratio, was then cut into circular patches matching the dimensions of the repair area. The prepared patches were bonded to the laminate one by one by aligning each patch's lay-up direction with the underlying ply. An extra ply having the same orientation with the outermost layer covered the whole repair area as shown in Figure 3.1, reinforcing the repair as suggested by the Structural Repair Manuals [3,4]. The following steps were vacuum bagging the repaired specimens and curing at 66°C (+/- 5°C) with a heat blanket for 1 hour. Vacuum pressure throughout the cure cycle was 650 mmHg. Table 3.1 shows the material properties of the adhesive impregnated dry fabric [128]. Properties in the out-of-plane direction were estimated from literature for similar material systems [111,171]. Table 3.2 lists the mechanical properties of the HYSOL EA 9396 adhesive, whose cohesive properties are further discussed in Section 3.4 and Appendix A.

Prepreg repair: This approach employed the original M21/AS4C prepreg and followed the same procedures given above, except that a single layer of FM-300K film adhesive with a cured thickness of 0.2 mm bonded the repair patch to the parent laminate. Repaired laminates were vacuum-bagged and cured with a heat blanket

according to the manufacturer's cure cycle requirements; 180°C (+/- 5°C) for 9 hours [166].

Appendix D shows the photographs of each repair process.

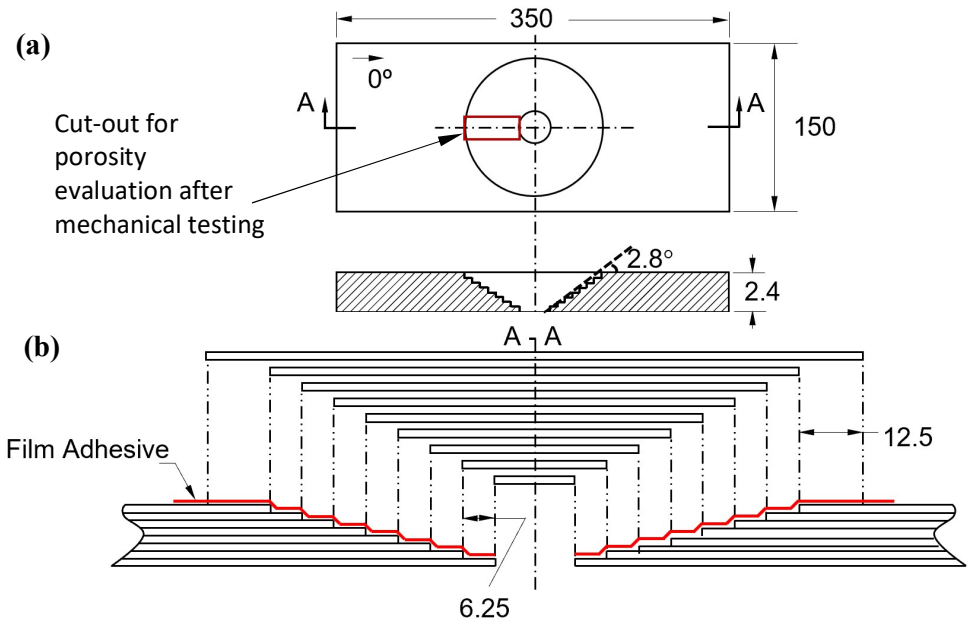

Figure 3.1. (a) Schematic view of the test specimens before repair. Thickness is exaggerated for clarity. (b) Cross-sectional schematic showing the repair geometry. Film adhesive and prepregs are used for prepreg repairs, and adhesive impregnated dry fabrics are used for the wet lay-up repairs. Dimensions are in mm.

Non-destructive Inspection: The repaired panels were inspected by Automatic Ultrasonic Through Transmission (AUTT) methods and Manual Ultrasonic Pulse-Echo Inspection (MUPE). First, defects were detected and located via AUTT. Afterward, found defects were evaluated and characterized by MUPE. The evaluation criteria for de-bonds and delamination were intermediate echo with 25 % screen height in case the sensitivity calibration was based on back wall echo with 80

% height of the sound material. Considering this, no delamination or debond was detected on the parts. Porosity evaluation was also performed by comparing the attenuation levels between the sound part and the repair. The porosity evaluation criteria were the 6 dB attenuation difference (ΔdB) between the repaired sections and sound material, the general acceptance criteria in monolithic CFRP structures. In addition, an NSI X5000 computed tomography system [172] equipped with a 4096 x 4096 detector at 16-bit resolution imaged a selected prepreg specimen before mechanical testing to obtain information about the repair geometry and its integrity. The repaired part was scanned at 120 kV and 350 μA with 1440 projections for 2 hours.

Table 3.1. Mechanical properties of Hexforce G0904 plain weave dry carbon fabric impregnated with HYSOL EA 9396 adhesive, with a 1/3 weight ratio [128].

Property	**Symbol**	**Value**
Elastic Modulus (GPa)	E_{11}	49.6
	E_{22}	49.6
	E_{33}	8.0
Shear Modulus (GPa)	G_{12}	3.3
	G_{13}, G_{23}	2.8
Tensile Strength (MPa)	X_t	517
	Y_t	517
Shear Strength (MPa)	S_{12}	60
	S_{13}, S_{23}	34
Poisson's Ratio	ν_{12}	0.045
	ν_{13}, ν_{23}	0.28

Table 3.2. Mechanical properties of the HYSOL EA 9396 [173,174] adhesive.

Property	Symbol	Value
Tensile Modulus (GPa)	E	2.7
Shear Modulus (GPa)	G	0.7
Tensile Strength (MPa)	t_n^0	55
Shear Strength (MPa)	t_s^0 , t_t^0	26
Tensile Stiffness (N/mm^3)	K_n	10^6
Shear Stiffness (N/mm^3)	K_s, K_t	10^6
Toughness in Tension (N/mm)	G_{IC}	0.3
Toughness in Shear (N/mm)	G_{IIC}, G_{IIIC}	0.5

Mechanical Testing: An Instron 5985 Extended Grip Electro-mechanic Testing Machine (Massachusetts, USA) performed the mechanical characterization of the specimens according to the ASTM Standard for Tensile Testing of Polymer Matrix Composites (D3039/3039M) [164]. The measurements employed displacement control at a rate of 0.5 mm/min. The loading axis was parallel to the 0° plies. Figure 3.2 shows photographs of the test setup with strain gauges on various locations, facilitating the measurement of local strains. The placement of two gauges at the exact location on opposite sides of the specimen (marked as 1 and 2 in Figure 3.2) enabled monitoring any undesirable localized bending behavior during testing. In addition to large repair panels, six standard test coupons (22 mm × 350 mm) with no damage were tested under the same conditions to determine the strength of the intact laminate. For these measurements, the full-sized intact specimens are not used as they tend to fail at the tabs leading to inconsistent results

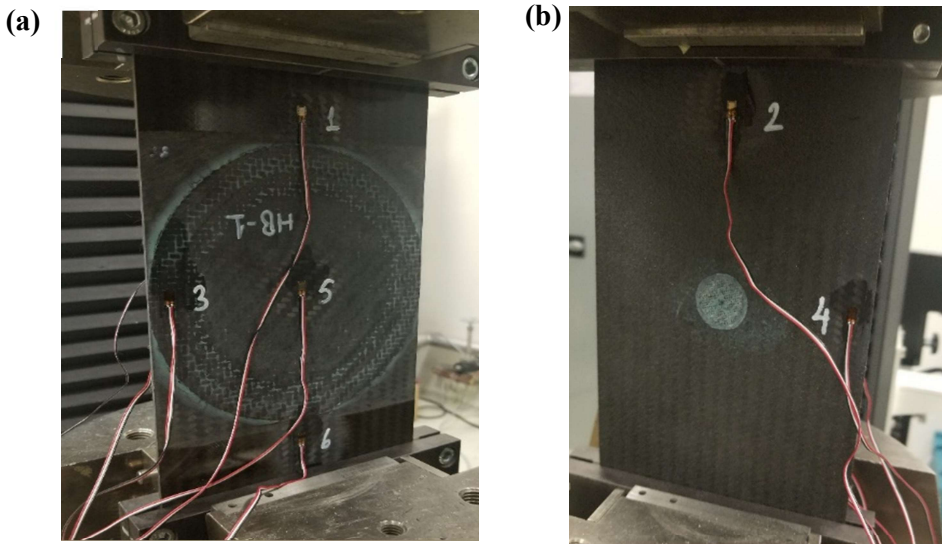

Figure 3.2. Photographs of the test setup for a representative prepreg repaired specimen, (a) front surface, (b) back surface.

Porosity Evaluation: After the mechanical tests, 35 mm X 15 mm slices were cut from the repair zone as shown in Figure 3.1, and microscope examinations according to ASTM E3-11 [175] evaluated the extent of porosity in the repair zones. The cross-sections of these slices are microscopically examined for three prepreg and three wet lay-up repaired specimens. After a diamond-coated cutting blade cut the specimen, the surfaces were cleaned thoroughly. Then the samples were mounted in cold-curing epoxy resin and ground with different grit SiC papers to remove the scratches and surface defects. Then the surfaces were polished with 3 μm and 1 μm diamond paste. An Olympus GX53 Inverted Microscope imaged the cross-sections, and the Olympus Stream Essentials software package [176] measured the patch porosity through image processing.

3.3 Experimental Results and Discussion

Before the mechanical testing of the parts, a representative specimen was imaged with CT to gain further information about the geometry of the repair section. Figure 3.3 shows a section of the CT scan around the repair zone. The white contrast regions correspond to the FM-300K adhesive layer. The thickness of the adhesive layer was measured as ~0.2 mm, consistent with the manufacturer's data [166]. The stepped geometry and dimensions were consistent with the target geometry schematically shown in Figure 3.1. The image shows clear signs of porosity, which will be further discussed in the following sections.

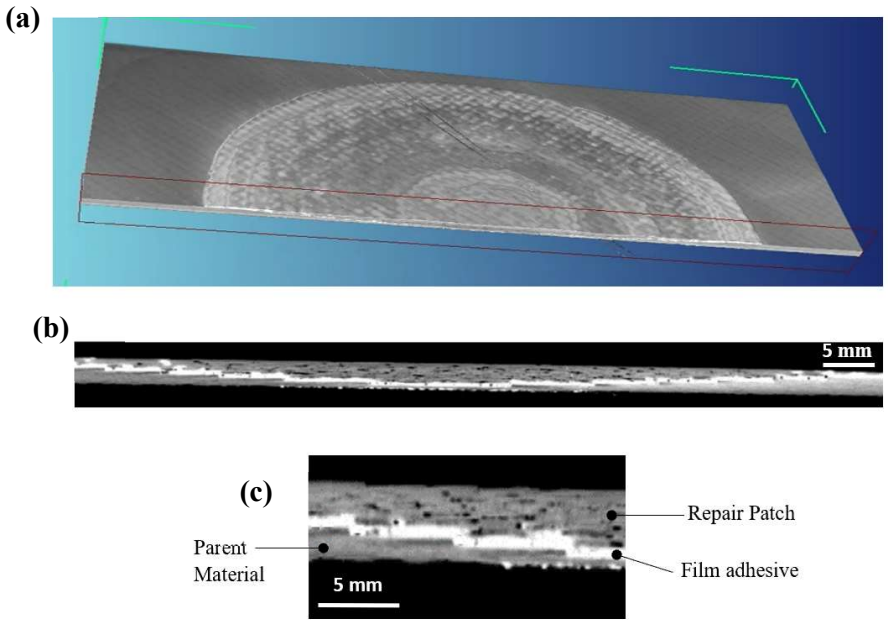

Figure 3.3. Computed tomography (CT) images of a representative prepreg repair zone before tensile testing. (a) A general view showing the cross-section used for the repair examination. (b) Cross-sectional view of the same CT scan. White contrast regions represent the film adhesive. (c) A close-up view showing the adhesive, parent material, and the repair patch more clearly.

Figure 3.4 shows the representative experimental tensile force vs. displacement curves for the stepped, damaged, repaired, and intact specimens. The intact panels were coupon-sized specimens smaller than the other cases, and the associated force-displacement curve was scaled based on the cross-sectional area and length for a meaningful comparison.

The data of the intact specimen exhibits a linear elastic response. On the other hand, repaired specimens exhibit a decrease in the load-displacement slope for the later stages of the data, indicative of adhesive failure. This slope change becomes more evident for the wet lay-up repaired specimens, where adhesive failure accompanies the laminate failure. The minor deviations from linearity in the earlier stages are due to the minor slippage in the testing machine grips. The ultimate failure takes place abruptly without any significant plasticity for all specimens. There was a fiber breakage sound just before failure, in agreement with this observation.

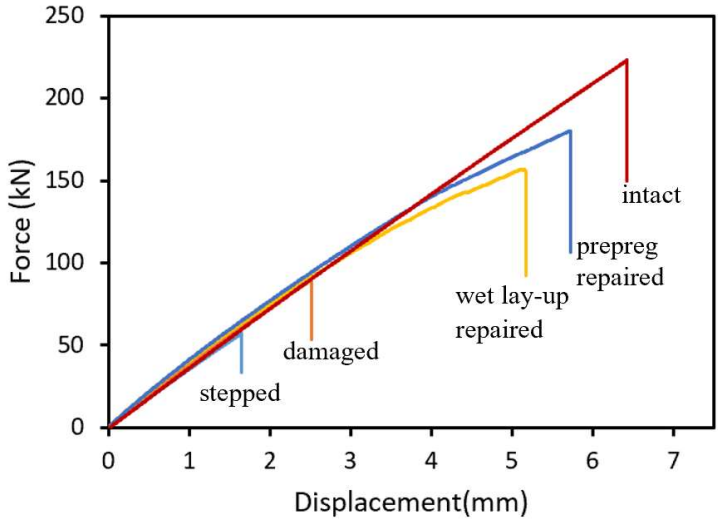

Figure 3.4. Force-displacement curves for intact, damaged, stepped, and repaired specimens. The intact coupon's force and displacement data were scaled for a meaningful comparison.

Table 3.3 summarizes the results of the mechanical testing for each case. The strength values correspond to the maximum load divided by the initial cross-sectional area of each specimen. The coefficient of variance (CoV) values is below 6% for each case, demonstrating the high repeatability of the results. The recovery rate is a measure of the success of the repair process in recovering the original strength of the undamaged part. It is defined as the ratio of the strengths of the repaired part and the undamaged part given in Eq. (2.1). The damaged specimens with 18 mm diameter holes exhibit a strength reduction of 60% compared to the intact laminate. The strength of the stepped specimens is even lower (24.8% of the intact laminate strength) due to the additional material removal. When it comes to the repaired specimens, the wet lay-up provides a recovery rate of 66%, whereas the recovery rate for the prepreg repair reaches 76%.

Table 3.3. Summary of the tensile testing results.

Specimen Type	**# Of Specimens Tested**	**Average Tensile Strength (MPa)**	**Maximum Tensile Strength (MPa)**	**CoV (%)**	**Recovery Rate (%)**
Damaged	3	244	255	3.0	40.0
Stepped	3	149	152	2.5	24.8
Wet Lay-up Repaired	5	398	416	4.0	66.0
Prepreg Repaired	6	455	480	5.4	76.0
Intact	6	600	614	2.0	-

Figure 3.5 shows photographs of representative specimens upon fracture, providing insight into the mechanisms of failure. The fracture plane is perpendicular to the loading axis for the damaged and stepped specimens, and the fracture initiates from the hole. This is an expected result caused by the stress concentration near the holes and the stepped regions.

For the repaired specimens, on the other hand, the fracture type and path depend on the load-carrying capacity of the repair. When the load-carrying capacity is low, cohesive failure is a dominant failure, as observed in the case of wet lay-up in Figure 3.5 (c). Wet lay-up repairs' fracture path also exhibits a relatively more irregular appearance. This is due to the lack of distinct adhesive layers and more extensive manual processing that increases the geometrical deviations. In the presence of cohesive failure, the fracture begins from the bonded surface and then spreads into the parent laminate. The failure on the repair patch is along the edge of the outermost step, where the reinforcement layer bonds to the part. There is no debond detected between the extra reinforcement layer of the repair patch and the parent laminate since they are in the same direction, having similar stiffness values.

When it comes to prepreg specimens, the higher strength of the repair results in either limited or no cohesive failure, as exemplified in Figure 3.5(d) and (e). The stronger repair moves the fracture plane away from the hole. In fact, in Figure 3.5(e), the failure takes place outside the repair region.

Figure 3.5(d) specimen exhibits a cohesive and laminate failure combination, with green regions corresponding to the FM-300K film adhesive. This specimen's lower strength and adhesive failure are probably due to an undetected defect on the bonding region that caused a stress concentration. Except for a few low-strength repairs excluded from the test data due to detected defects, most prepreg repair surface failures are cohesive, indicating satisfactory surface preparation before bonding.

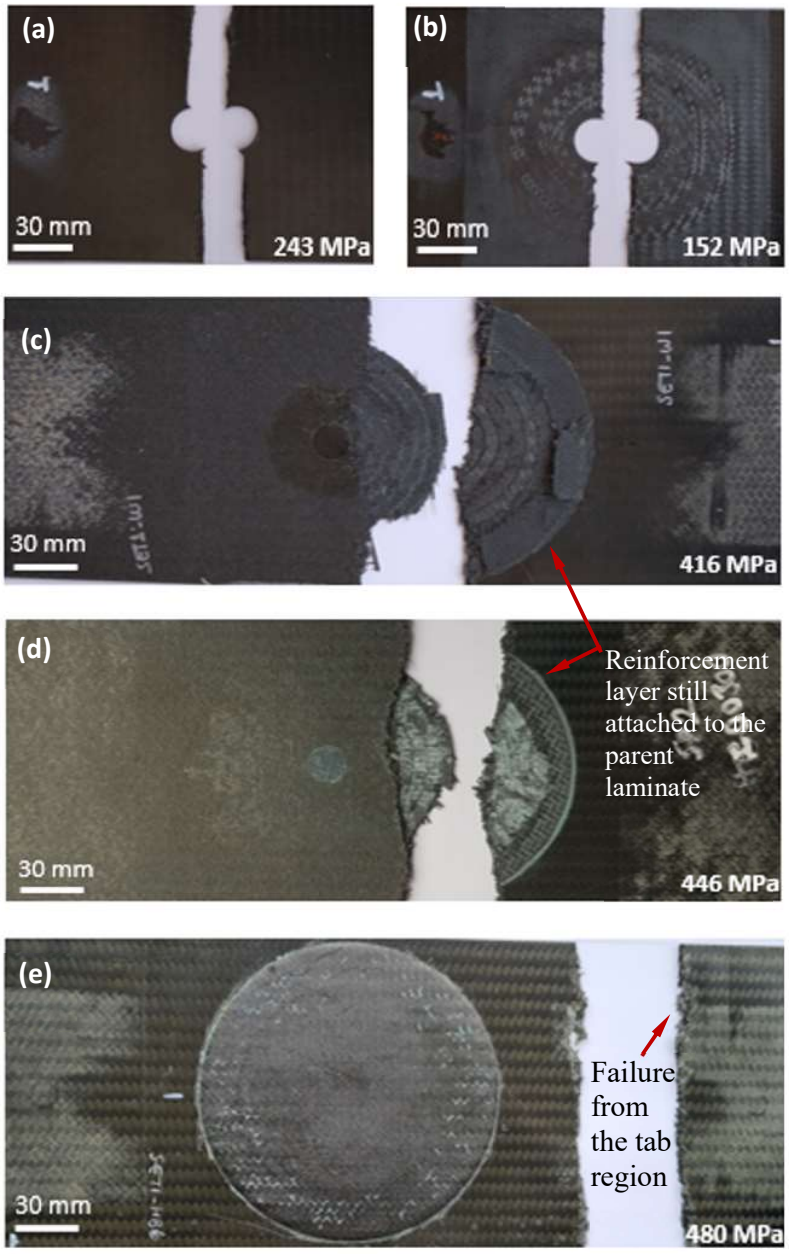

Figure 3.5. Photographs of the fracture surfaces of representative test specimens. The values at the bottom right indicate the average strength for each case. (a) damaged specimen, (b) stepped specimen, (c) wet lay-up repaired specimen, (d) and (e) prepreg repaired specimens. In (d) and (e), the right-hand side parts are flipped to reveal the failure surfaces more clearly.

The results of the prepreg specimens show that 2.8° (6.25 mm) scarfed/stepped repairs are ideal for the studied composite and adhesive system, providing repair strengths reaching that of the intact laminates.

One can compare this experimental result with the theory as follows. By re-arranging Eqn. (2.6), minimum adhesive shear strength to satisfy intact laminate strength can be predicted as:

$$\tau_{ymin} = \frac{K_s \sigma_f}{2} \sin\left(2 \propto_{opt}\right) \tag{3.1}$$

Using a scarf angle of 2.8°, a stress concentration factor of 1.25, and an intact laminate strength of 614 MPa for the quasi-isotropic woven fabric laminate under consideration [177]; the minimum adhesive shear strength should be 37.5 MPa to reach the strength of the undamaged material.

FM-300K adhesive, having 42 MPa shear strength, is, therefore, an appropriate adhesive for the 2.8° scarf angle (6.25 mm step length) prepreg repairs. However, since its strength value is close to the minimum adhesive shear strength predicted above, any degradation on the adhesive or any defect that remains undetected will lead to lower strength values, as observed in the case depicted in Figure 3.5(d).

When it comes to the HYSOL EA 9396 utilized in wet repairs, Eqn. (2.6) predicts a scarf angle less than 1.9° (a minimum of 10 mm step length) to satisfy parent laminate strength under ideal conditions. This prediction is parallel with the SRM recommendations of 1.9° scarf angle and 12.5 mm step length for repairs [3,4]. These observations explain the lower strength values and the adhesive failure of the wet lay-up specimens, which employed step lengths of 6.25 mm corresponding to a scarf angle of 2.8°.

Figure 3.6 shows representative views of the cross-sections of each repair technique. The parent laminate is free of porosity, whereas the repair patch and the adhesive include various porosities, as observed in the CT scans presented in Figure3.3.

The porosity levels were quantified by examining three specimens for both prepreg and wet lay-up repaired specimens. By using the 2-D micrographs, the porosity content (PC) in the repair can be defined as:

$$PC_{Repair} = \frac{A_{Total\ area\ of\ the\ porosities}}{A_{Total\ area}} \tag{3.2}$$

The analysis excluded the delaminations and cracked areas, as these were caused by the tensile testing.

The porosities are mainly due to the lack of sufficient pressure in the curing process. The porous zones are primarily located in adhesive-rich zones and inter-fiber regions of the repair patch. As the thickness of the repair patch increases, more volatiles become trapped on the repair zone, which causes more pronounced porosity formation at the center of the repairs for both wet lay-up and prepreg. Wet lay-up exhibits the additional intra-fiber porosities due to the manual wetting process of the dry fabrics. Figure 3.7 shows the effect of porosity on the tensile repair strength. The tensile strength is normalized by the maximum strength attained for the prepreg repairs (480 MPa). The results show that tensile strength decreases as porosity increases for the higher porosity levels. There is no significant reduction for the porosity levels less than 3 %, which coincides with the Chapter 2 results. The repair strength is not just only related to the porosity content but also the larger porosities, namely voids, creating stress concentration sites that may reduce the strength dramatically.

Porosity primarily affects the matrix-dominated strength values such as compression and interlaminar shear strength in intact composite parts and does not directly influence the fiber-dominated tensile properties. On the other hand, any porosity in the adhesive directly affects the bonding strength of the repair. Furthermore, a high porosity content can make the structure more susceptible to environmental degradation and reduce fatigue. These long-term effects are critical for the effectiveness of the repair, which will be detailed in Chapter 4.

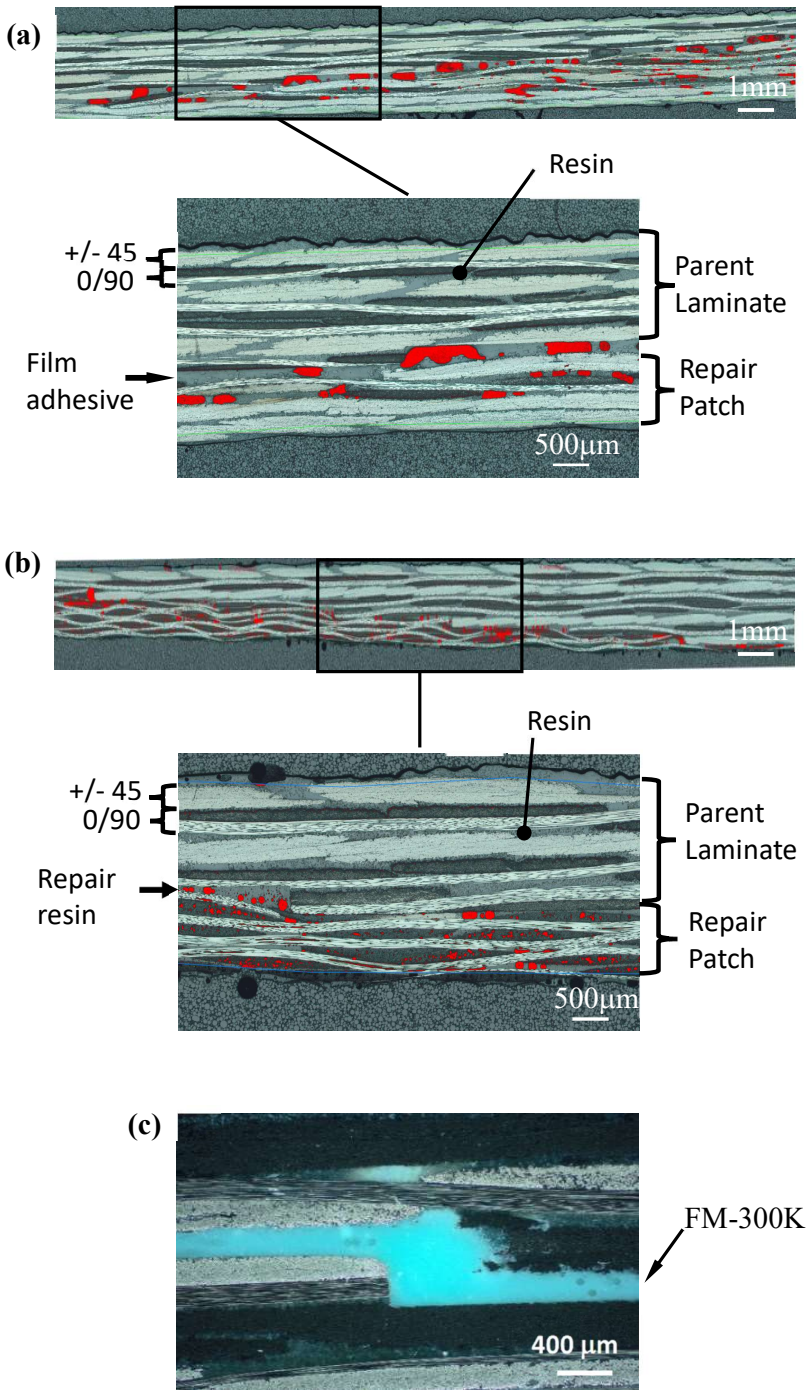

Figure 3.6. Optical micrographs of selected tested specimens. Red regions mark the porosities. (a) Prepreg repaired specimen, (b) Wet lay-up repaired specimen, (c) A polarized view of the FM-300K adhesive.

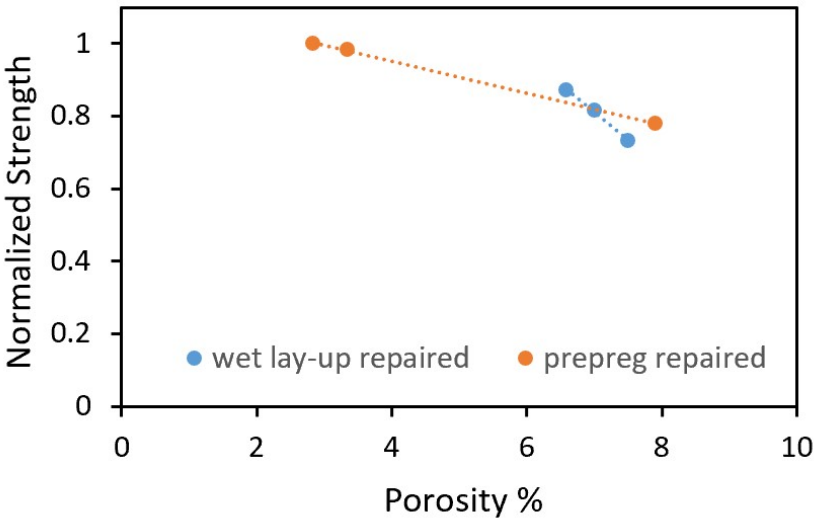

Figure 3.7. Normalized tensile strength of the prepreg and wet lay-up repairs for different porosity levels.

3.4 Modeling Methodology

To gain insight into the experimentally observed mechanical behavior of the repaired composites, finite element analyses were performed. This section presents the modeling methodology, followed by the results in the next section.

The tensile testing of the stepped repaired specimens was modeled by finite element method using ABAQUS 6.14 Standard. Figure 3.8 shows schematic views of the model and the boundary conditions. The model considered a quarter of the test specimen and excluded the clamped regions for reducing the computational load. Modeling using a full-sized specimen verified that the quarter-model's results are virtually identical to that of full-sized. Symmetry boundary conditions over the two edges of the quarter-specimen and a linear displacement boundary condition at the edge next to the clamped regions provided the tensile testing conditions. The material properties for the composite parent material, repair patch, and adhesive were based on the data presented in Table 2.2**,** Table 2.3**,** Table 3.1**,** and Table 3.2 respectively.

3D solid elements discretized the parent and the patch material. These were 8-node hexahedral C3D8R elements. For the parent material, the optimized mesh was 1 mm far away from the bonding region. It gradually became smaller, down to 0.15 mm towards the edge, which was implemented by edge seeding. For the patch, mesh size varied between 0.1 and 1.0 mm.

Figure 3.8(b) shows modeling details of the bonding region for the wet lay-up repairs. There was no extra adhesive layer bonding the patch and the parent material; instead, adhesive-impregnated layers maintained the bonding. Therefore, the model neglected the thickness of Hysol EA 9396 and considered it as an interaction property, which helped to reduce the simulation time. The model used a high interface stiffness of 10^6 N/mm^3 for the three directions of Hysol EA 9396. Such high interface stiffness values are required to prevent any disruption to the general compliance of the system before the damage starts [178]. When the interface stiffness is in the range of 10^5 – 10^6 N/mm^3, the cohesive elements do not affect the system's overall load-displacement behavior [168,178], while higher stiffness values can cause numerical convergence issues.

Figure 3.8 (c) shows modeling details of the bonding region for the prepreg repairs, which were modeled by the cohesive element tool of ABAQUS. The model took the thickness of FM-300K into account, with $\mathrm{K_n}$, $\mathrm{K_t}$, and K_s being calculated from Eq. 1.18. 23140 eight-node 3D cohesive elements (COH3D8) discretized the adhesive domain. The element size varied in the range of 0.1 – 0.5 mm. To model with the cohesive elements, tie constraints connected the mismatching nodes at the adherend-adhesive interface, assuming perfect bonding.

Hashin failure theorem and Cohesive Zone Modeling (CZM) defined the composite laminate and the adhesive failure, respectively. Chapter 1 and Chapter 2 provide full details of these approaches.

Lastly, the Benzeggagh and Kenane (B-K) factor, η (Eqn. 1.26), was taken as 2.3 following the same approach utilized in Chapter 2. Consideration of η values between 1 and 2.5 did not yield any significant difference in the peak loads and the displacements.

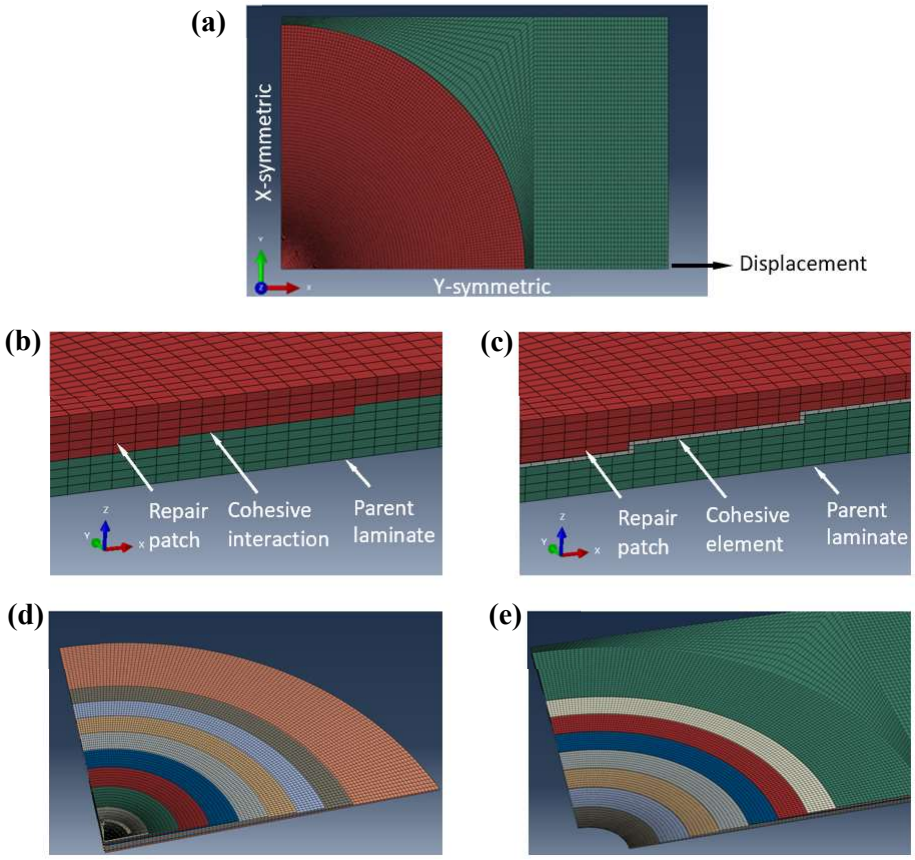

Figure 3.8. (a) Schematic description of the finite element model. (b) Close-up view of the mesh structure around the steps for wet lay-up repair and (c) prepreg repair. (d, e) Interface region of the repair; repair patch and parent laminate sides, respectively. Each color represents a separate layer.

3.5 Modeling Results and Discussion

Figure 3.9 shows load-displacement predictions of the finite element analysis for stepped, damaged, wet lay-up repaired, and prepreg repaired specimens. The figure also shows the strain gauge-based experimental data for comparison. The results show that the finite element model can closely predict the experimentally observed load-displacement behavior. The slight discrepancy between the analysis predictions and experimental data is mainly due to the minor slippage in the testing machine grips, which becomes more evident for higher loads.

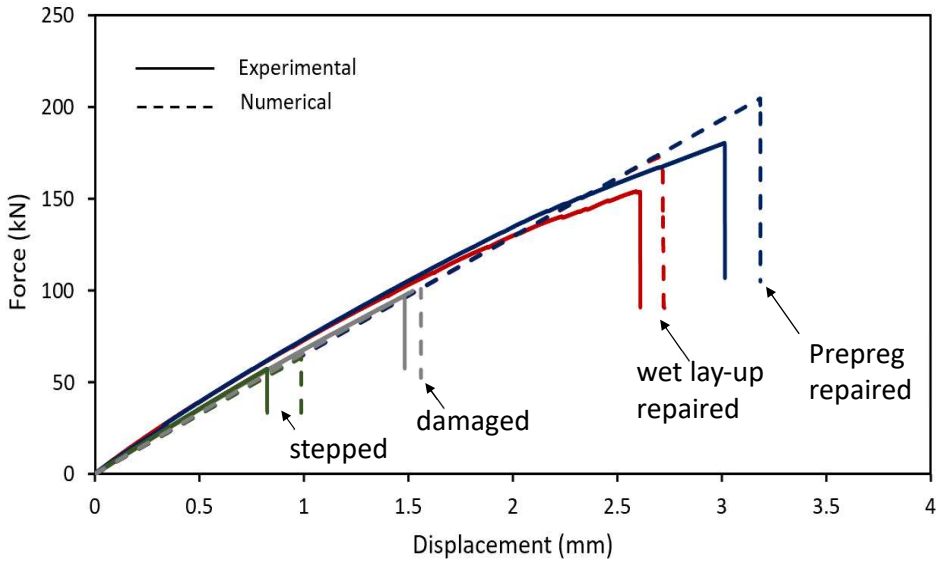

Figure 3.9. Experimental and numerical load-displacement curves for stepped, damaged, wet lay-up repaired, and prepreg repaired specimens. The experimental displacement data are based on strain gauge measurements.

Figure 3.10 compares the simulation predictions with the experimental results regarding the failure strength, which is calculated by dividing the maximum force to the initial cross-sectional area. The differences between the experimental data and the simulation predictions are within 10%. Simulations slightly overpredict the failure load.

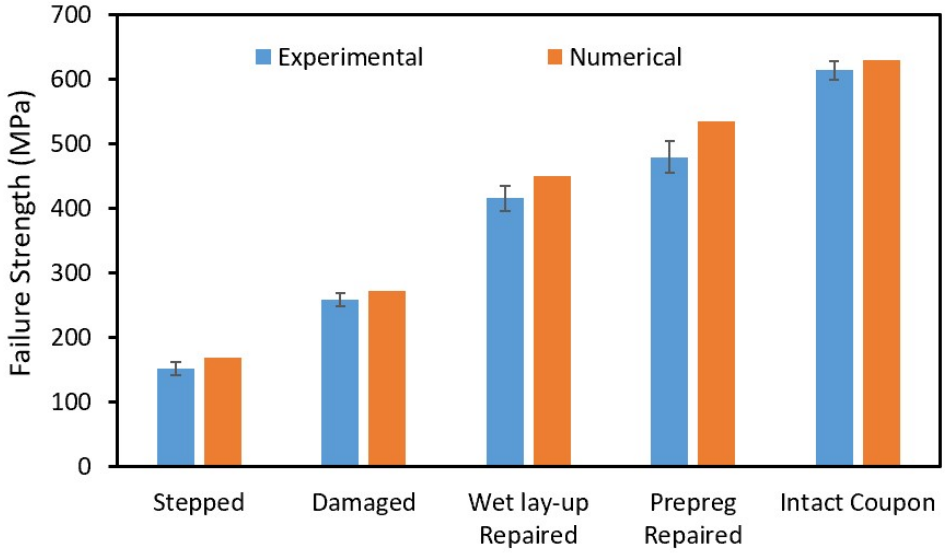

Figure 3.10. Failure strength of the specimens as determined by experiments and as predicted by simulations.

An investigation of the scalar damage variable for cohesive surfaces in general contact (CSDMG), as defined in Eqn. (1.22) provided further insight into the damage evolution in the joint region. Figure 3.11 shows the damage variable (damage index) for wet lay-up repair over the bonding area at the onset of damage. The data is presented for directions having 0°, 45°, and 90° angles with respect to the loading direction, through the middle of the steps to eliminate the edge effects caused by thickness changes.

The results show that the damage index strongly depends on the direction. The damage index is highest for the 0° path and gradually decreases for 45° and 90° paths, respectively such that it is nearly zero for the case of 90°. The damage index also exhibits oscillations that depend on the ply orientation for each direction. Specifically, plies having an orientation of 0° exhibits a larger damage index than 45°-oriented plies. This dependency of ply orientation on the damage index is due to the anisotropic nature of the composite [66,68,92]. The anisotropy causes variations in the laminate's stiffness over the scarf length as opposed to the uniform stiffness of

the adhesive. The resulting adhesive-adherent stiffness mismatch is highest for the 0° plies, resulting in higher stress concentrations and earlier failure. On the other hand, the damage is nearly zero on the extra layer bonding zone due to the similarity (stiffness and orientation) of the reinforcement layer and the outermost layer of the parent laminate. In addition to the variations over the scarf length, the damage index is also higher at the edges due to the step geometry creating peel stresses [92,179].

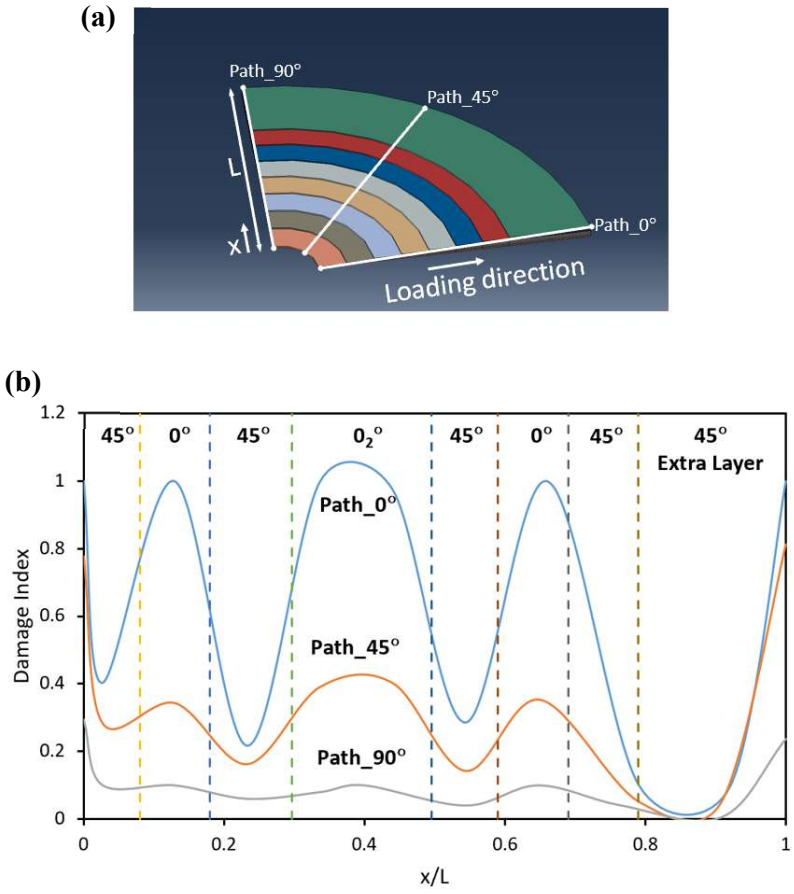

Figure 3.11. (a) Schematic description of the three paths on the bonding area, defined with respect to the loading direction on the parent laminate side. (b) Damage index distribution with respect to the normalized distance along the bonding area over different paths, shown for the onset of damage.

Figure 3.12 and Figure 3.13 presents the damage condition of the repaired parts for 99% of the ultimate failure load. The damage parameters under consideration are scalar damage variable of cohesive elements (SDEG) for prepreg repairs, the scalar damage variable of cohesive surfaces in general contact (CSDMG) for wet lay-up repairs, fiber damage in warp direction (FV1), and fiber damage in weft direction (FV2). Since FV1 and FV2 exhibit similar trends, the figures only show the FV1 data. FV1 is observed both 0° and 45° plies whereas FV2 is only for 45° plies. A value of zero corresponds to the undamaged state, and 1 indicates complete failure. FV1 and FV2 can only take 0 or 1, whereas SDEG and CSDMG can have intermediate values due to the built-in cohesive modeling.

For the prepreg repairs shown in Figure 3.12, the primary failure mode is fiber failure in both directions leading to the total laminate failure near the tab region. There is no cohesive failure on the adhesive predicted by the simulation except for a slight degradation at the edges of the adhesive due to the peel stresses. These simulation predictions are in agreement with the experimental result shown in Figure 3.12 (e). The analysis shows no adhesive failure is expected for FM-300K adhesive-bonded with 6.25 mm step length (2.8° scarf angle). As a result, the repair strength is close to the intact laminate's strength.

Figure 3.13 shows similar information for the case of wet lay-up repairs. In this scenario, cohesive failure is accompanied by fiber failure in both warp and weft directions. The fracture begins from the bonded surface, and when the load-carrying capacity of the adhesive is exceeded, it spreads to the parent laminate. Figure 3.13 shows the photo of an experimentally observed failure, where there is no debonding between the extra layer and the uppermost layer of the parent laminate, in agreement with the simulation predictions.

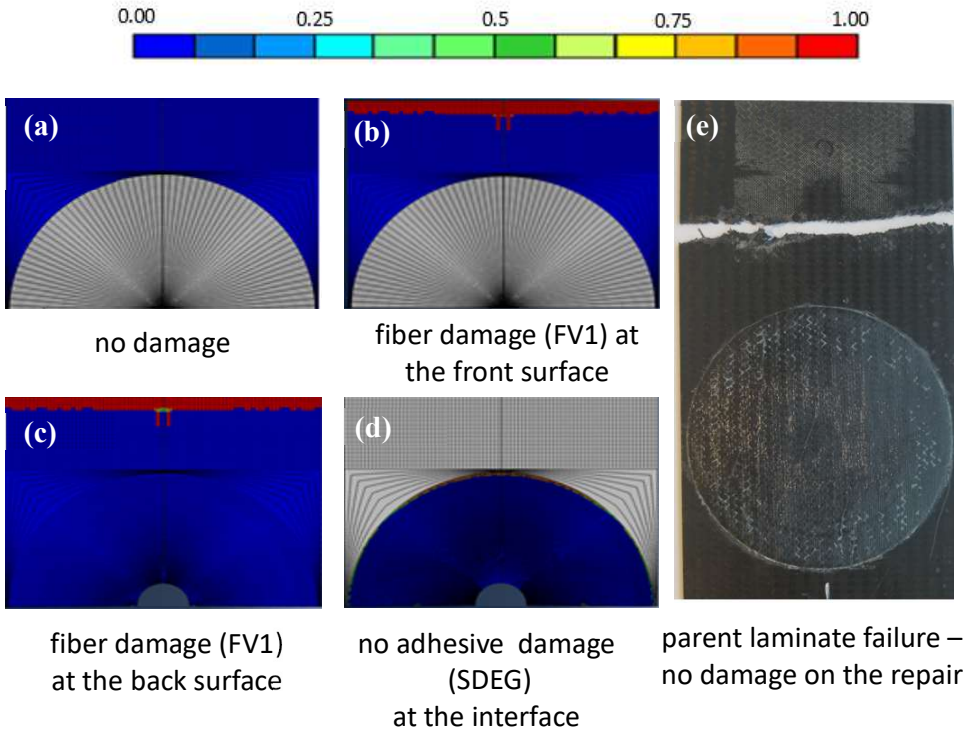

Figure 3.12. Failure map of prepreg repairs corresponding to 99% of the ultimate load. The simulation results are mirrored with respect to the symmetry axis for ease of visualization. (a) No damage. Grey region indicating the repair patch, blue region is the parent laminate. (b) Fiber damage at the front surface of the parent laminate; no damage is present on the repair zone. (c) Fiber damage at the back surface of the parent laminate; no damage is present on the repair zone. Parent laminate on the bonded surface, showing no fiber damage. (d) Adhesive damage on the repair region; no damage is present on the repair zone. (e) Photograph of an experimentally tested specimen where parent laminate failure is visible with no damage on the repair zone.

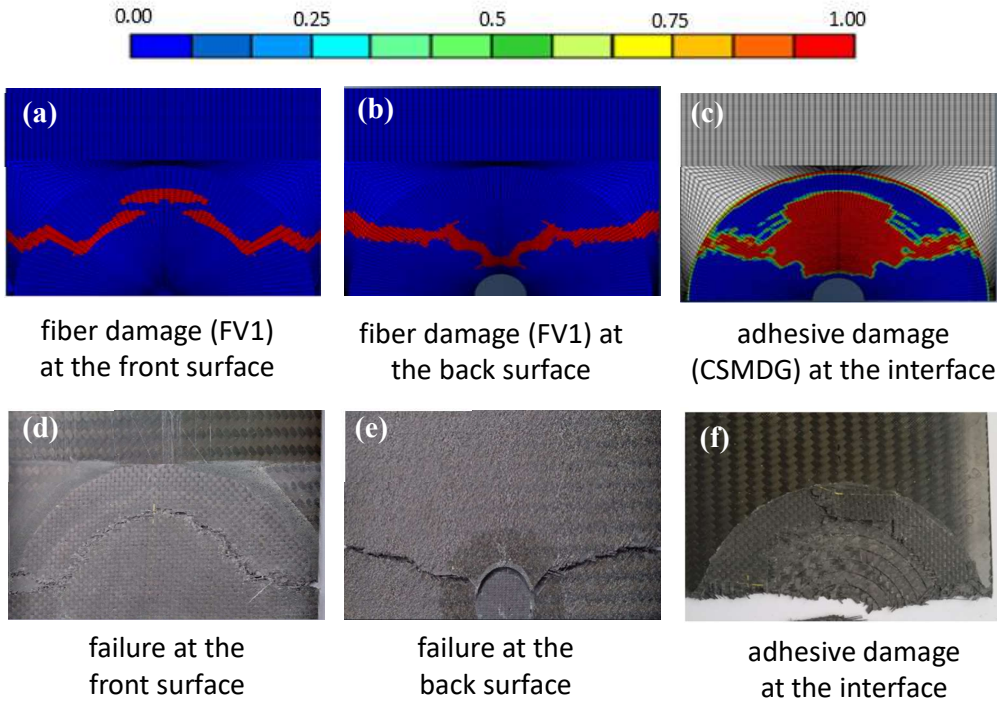

Figure 3.13. Failure map of wet lay-up repair corresponding to 99% of the ultimate load. The simulation results are mirrored with respect to the symmetry axis for ease of visualization. (a) Fiber damage at the front surface. (b) Fiber damage at the back surface. (c) Adhesive damage on the bonded region. (d) Experimental observation of the front surface exhibiting laminate failure. (e) Experimental observation of the back surface exhibiting laminate failure. (f) Adhesive failure of the bonded region.

Figure 3.14 shows snapshots of the damage evolution on a representative force-displacement curve for the wet lay-up repairs. At point (a), the loading is within the elastic limits. Therefore, there is no damage neither on the adhesive nor on the composite part. Point (b) shows the initial damage in the adhesive region of the 0° overlapping plies, which progresses both circumferentially and towards the 45° layers. Upon the failure of approximately half the adhesive area, the fracture spreads to the parent laminate, and fiber failure begins near the edge of the hole. This can be inferred from the snapshot of point (c). At this stage, the damage evolution is very

rapid, and complete failure occurs as the fiber failure follows the adhesive failure path and reaches the edge of the part, as demonstrated in the snapshot of point (d).

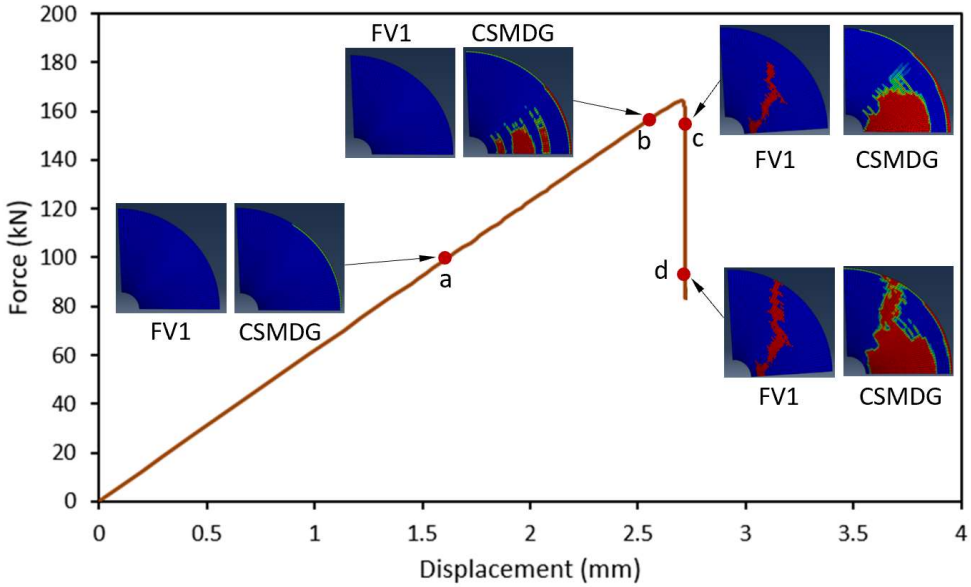

Figure 3.14. Evolution of the adhesive and fiber damages shown together with the force-displacement curve for the case of wet lay-up. CSDMG represents adhesive damage, and FV1 represents fiber damage.

Adhesive shear strength, t_s^0 is a critical parameter that directly affects the failure load of the repaired zone. An additional analysis focusing on this parameter provided further insight into the problem. In the analysis, the strength of the adhesive was assumed as isotropic, and the fracture toughness values were taken as zero for enabling a direct comparison and reducing the computational load.

Figure 3.15 shows the results of the failure load of the repaired specimen normalized by the parent laminate's failure load. For adhesive strengths up to 35 MPa, the failure load increases as adhesive strength increases. This dependence is caused by the fact that the failure initiates from the adhesive region and leads to the fracture of the repaired area. Beyond 35 MPa, the failure load reaches the undamaged parent

laminate, and the fracture occurs near the tab area. The 35 MPa adhesive strength that defines the transition from repair failure to laminate failure is in close agreement with the analytical prediction of 37.5 MPa discussed in Section 3.3.

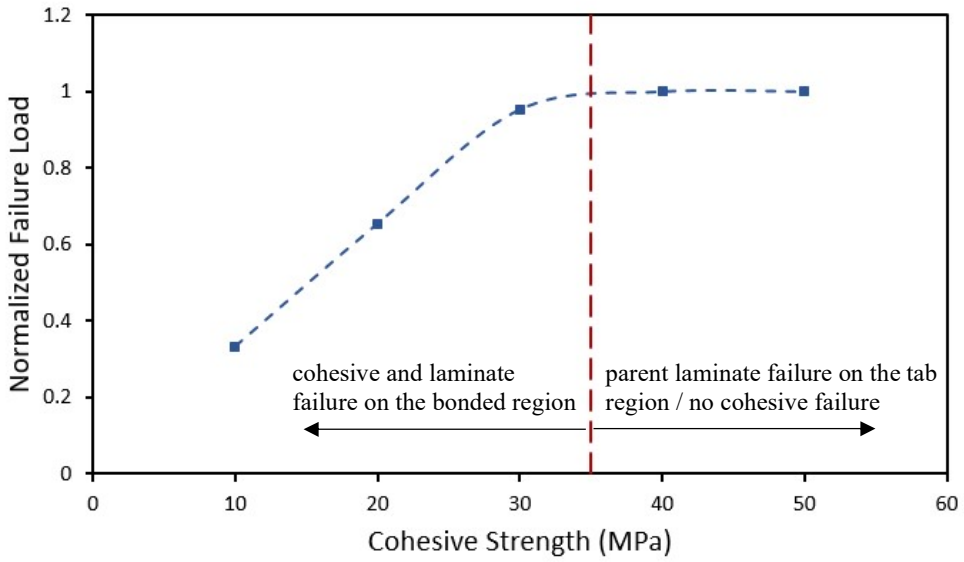

Figure 3.15. Normalized failure load for varying cohesive strength of the adhesive.

Next, Figure 3.16 demonstrates the effect of fracture toughness on the failure load of the repairs. The analysis performed in this part assumed an isotropic adhesive shear strength value of 25 MPa in all directions. The fracture toughness was also assumed to be isotropic for simplicity. The results show that the fracture toughness has little effect on the failure load under these circumstances.

Lastly, the effect of the extra layer and its orientation on the repair strength was investigated. Figure 3.17 shows the normalized von-Misses stress over the parent laminate bonding surface for repairs with no extra layer, and with extra layers having lay-ups of [45] and [0], and two extra layers with [0/0] lay-up. Again, the normalization was done with respect to the maximum far-field stress.

As the stiffness of the repair patch increases, it carries more load, so the stress passing the parent laminate decreases. 0° oriented extra layers decrease the stress

concentration on the parent laminate and so the adhesive. Choosing the orientation of the extra layer different from the uppermost layer of the parent laminate creates undesired peel stresses on the edge of the bonding region, decreasing the failure strength if any adhesive or patch failure is involved.

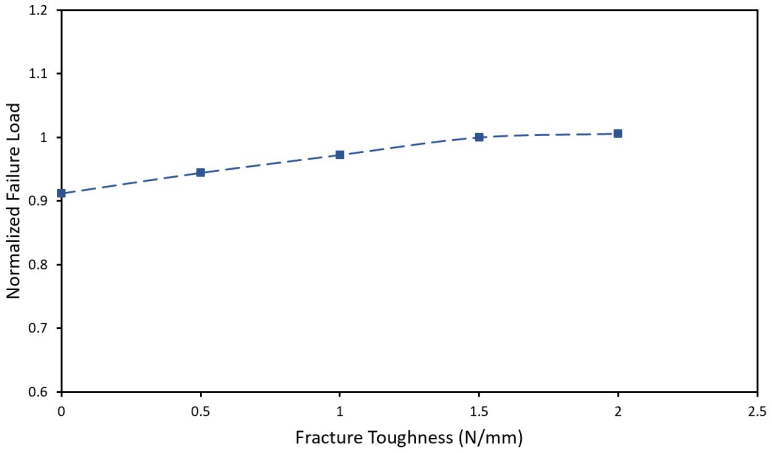

Figure 3.16. Normalized failure load for different toughness values.

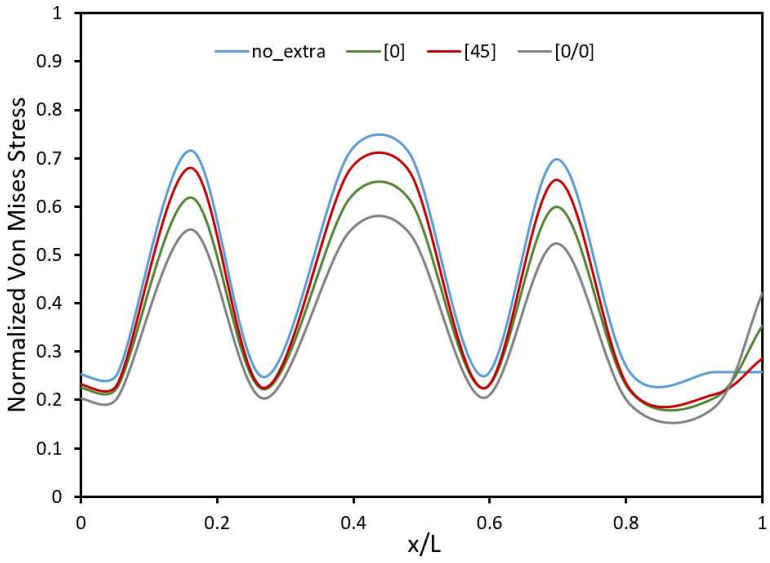

Figure 3.17. Normalized von Mises stress distribution over the bonded area of the parent laminate.

3.6 Conclusions

This chapter considered experimental measurements on stepped repaired laminates with 6.25 mm step lengths. The study employed curing out of autoclave, aiming to simulate the on-site repair scenarios. The strength recovery reached 76% for prepreg repairs and 66% for wet lay-up repairs. For the prepreg repairs, the laminate structure fails without considerable damage in the bond area. In contrast, both cohesive failure within the adhesive and the parent laminate failure was observed for the wet lay-up repairs. The average porosity levels were higher for the wet lay-up repairs compared to the prepreg repairs. Increasing porosity decreased the repair strength in either case for the high porosity ratios.

Finite element analysis closely predicted the experimentally measured repair strength and provided further insight into the failure behavior of the repaired panels. Like the 2-D scarf bonded joints, stress concentration plays an essential role in the failure behavior of the repaired panel specimens. The results showed that the most critical regions in the bond area are the 0° plies, where the adhesive-adherent stiffness mismatch is highest in the loading direction.

Upon verifying the modeling accuracy, the effect of several parameters on the repair strength was investigated for the case of prepreg repairs. First, as the shear strength of the adhesive increases, the failure load increases until the bond strength reaches the strength of the laminate. Beyond this limit, a further increase in the shear strength has no benefit on the repair strength. On the other hand, the adhesive's fracture toughness value had only a minor effect on the repair strength, for the case of a 25 MPa adhesive shear strength value. Lastly, having an extra reinforcement layer decreases the peak stress on the adhesive as long as the fiber orientation of the extra layer matches that of the adjacent layer.

Overall, the findings of this chapter have identified the key parameters that influence the repair strength and provided quantitative data that can be used for optimizing repair performance in practical applications.

CHAPTER 4

DURABILITY OF REPAIRED WOVEN FABRIC COMPOSITES

4.1 Introduction

The durability of the repairs under severe environmental conditions such as moisture and temperature is critical for the reliable long-term operation of the components. Therefore, there is a need to clearly understand the combined effects of temperature and moisture on the strength of the repairs, especially in the case of on-site repairs.

Adhesives and composites used in the aerospace industry should withstand both cryogenic and elevated temperatures in the range of -55°C – 200°C. The glass transition temperature (T_g) is the most critical parameter of the composite resin or the adhesive in this respect, as it marks the transition from a brittle and hard stage to a rubbery and soft stage. Therefore, the design of bonded repairs should consider the reduction in the mechanical properties of the adhesive and the repair composite above the T_g value. For example, at elevated temperatures above the glass transition temperatures, adhesives can exhibit strength reductions reaching 50% [180,181], which can considerably reduce the load-bearing performance of the associated components.

Moisture can generate an additional challenge in the materials requirements as it lowers the T_g of epoxy resins. In addition, the moisture absorption tends to be higher for adhesives than the composite laminate in a bonded joint, often rendering the adhesive as the limiting factor.

The undesired moisture might be due to pre-bond or post-bond factors. Pre-bond moisture leads to high porosity levels and is usually caused by storage, manufacturing, or surface treatment issues of adhesives and prepregs. Numerous studies investigated the pre-bond moisture effect on the bond strength [182–184].

On the other hand, the post-bond moisture depends on the operational conditions of the cured parts, such as temperature, water, humidity, thermal cycling, and exposure time, which in turn affects the strength of the structure, as reported in the literature [185–188]. Especially the low-temperature curing adhesives used in on-site repairs are more vulnerable to moisture effects than the high-temperature cure film adhesives.

The durability of the repaired parts should be guaranteed under the most severe conditions of moisture and temperature. Therefore, this part of the study investigates the effects of temperature and moisture on the repair strength for prepreg and wet lay-up repairs. In addition, the porosity evaluation was performed with both ultrasonic and microscopic inspections to establish correlations between environmental effects and defect format.

4.2 Experimental Details

The repair and inspection procedures have followed the same details described in Section 3.2. The main exception was the sanding of the repair surface to maintain a scarf angle of 3.8° (1/15 taper ratio). Figure 4.1 shows a schematic view of the repair

Table 4.1 shows the specimen types considered to investigate the effect of post-bond moisture on the repair strength. Both prepreg and wet lay-up repaired specimens were moisturized before testing by immersing them in a 70°C water bath for 14 days until 1.1% moisture content was reached. The bath's elevated temperature helped to accelerate the moisture intake of the parts. These conditioned specimens are named "hot-wet" specimens, whereas the untreated specimens are "dry". After 14-day conditioning, the specimens were preserved in sealed bags and within 3 hours, they were tested at 70°C. The dry specimens, on the other hand, were tested at 25°C. An Instron 5985 Testing Machine tested the hot-wet and dry panels according to the ASTM D3039/3039M Standard for Tensile Testing of Polymer Matrix Composites. . The measurements employed displacement control at a rate of 0.5 mm/min.

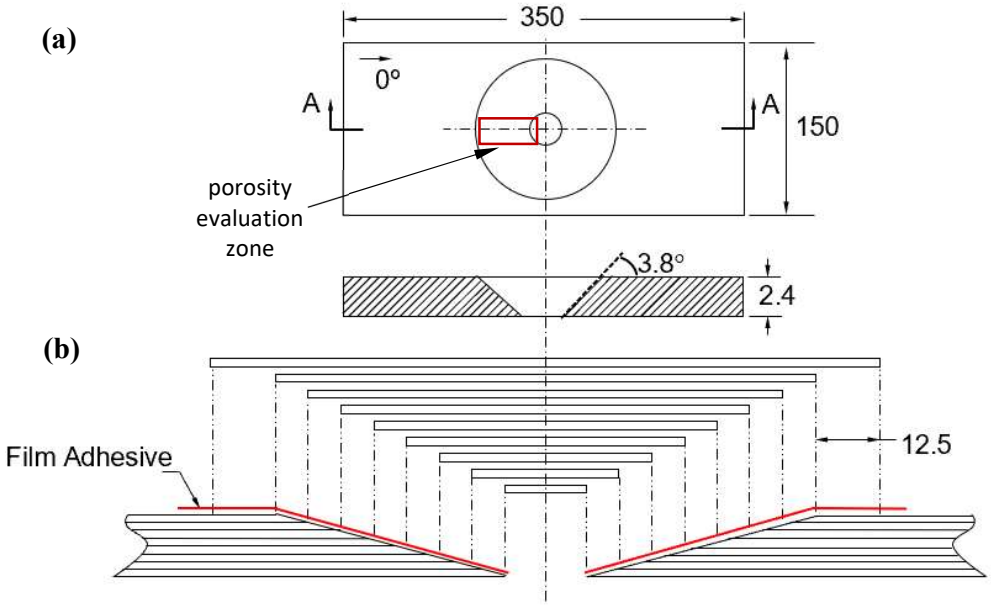

Figure 4.1 (a) Schematic view of the test specimens before repair. Thickness is exaggerated for clarity. (b) Cross-sectional schematic showing the repair geometry. Film adhesive and prepregs were used for prepreg repairs, and adhesive impregnated dry fabrics were used for the wet lay-up repairs.

Table 4.1. Test matrix to evaluate the effect of moisture and temperature.

Repair Type	Condition	Treatment	Test Temperature	# of Specimens Tested
Prepreg Repaired	Dry	None	25	5
	Hot-Wet	70° C water for 14 days	70	5
Wet Lay-up Repaired	Dry	None	25	5
	Hot-Wet	70° C water for 14 days	70	5

4.3 Experimental Results and Discussion

Table 4.2 summarizes the results for each type of specimen in terms of the average tensile strength, maximum tensile strength, coefficient of variation (CoV), and recovery rate. The strength values correspond to the maximum load divided by the initial cross-sectional area of each specimen, that is, the 150 mm × 2.4 mm area defined in Figure 4.1 (a). Recovery rate is the ratio of the repaired part's strength to that of the undamaged part (600 MPa), which quantifies the success of the repair process at recovering the original strength of the undamaged part.

First of all, the recovery rates of the specimens are somewhat lower compared to the results of the stepped specimens presented in Chapter 3 due to the higher scarf angle in the present case. Any scarf angle above 2.8° will lead to premature adhesive failure for prepreg and wet lay-up repairs as described through Eqn. (3.1).

When it comes to the effect of conditioning, the results show that the combined effect of temperature and moisture does not affect the tensile strength of the prepreg repairs significantly. In contrast, it reduces the strength of the wet lay-up case dramatically. The findings can be attributed to the high susceptibility of the low-temperature cure resins to moisture. This demonstrates the low durability of wet lay-up repairs and limits wet lay-up repairs as permanent repairs in practice.

Figure 4.2 shows the same results, normalized concerning the maximum strength of dry prepreg repaired specimens. For the wet lay-up repairs, the average repair strength of the hot-wet case is lower by nearly 30% concerning the repair strength of the as-received specimens. This strength is almost as low as the damaged hole strength reported in Table 3.3.

Table 4.2 Summary of the tensile testing results for the dry and hot-wet specimens.

Specimen Type	# Of Specimens Tested	Average Tensile Strength (MPa)	Maximum Tensile Strength (MPa)	CoV (%)	Recovery Rate (%)
Prepreg Repaired / Dry	5	381	410	5.0	68.0
Prepreg Repaired / Hot-Wet	5	388	417	6.0	65.0
Wet Lay-up Repaired / Dry	5	338	352	3.4	58.7
Wet Lay-up Repaired / Hot-Wet	5	235	265	7.8	44.1

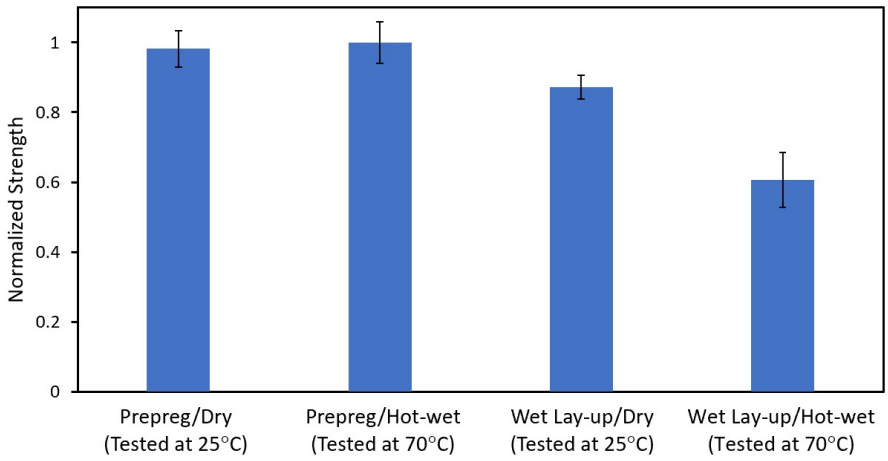

Figure 4.2. Normalized strength values of prepreg and wet lay-up repairs for dry and hot-wet conditions.

The photographs of representative specimens upon fracture are shown in Figure 4.3. By investigating the fracture surfaces, it can be concluded that the failure begins from the adhesive and then continues with the laminate until fracture of the part for both types of repairs

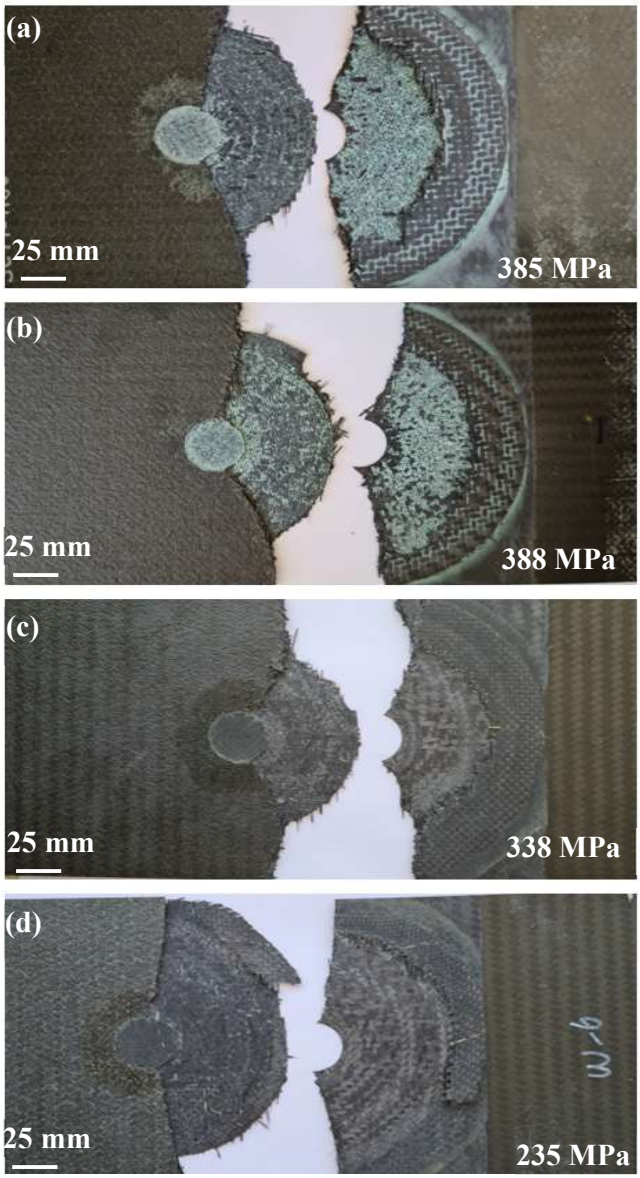

Figure 4.3. Photographs of the fracture surfaces of representative test specimens. The values at the bottom right indicate the average strength for each case. (a) prepreg repaired specimen in dry condition, (b) prepreg repaired specimen in hot-wet condition, (c) wet lay-up repaired specimen in dry condition, (b) wet lay-up repaired specimen in hot-wet condition. Right-hand sides are flipped for revealing the failure surfaces more clearly.

The failure strength and the fracture plane are the same for dry and hot-wet specimens for the prepreg repairs, as shown in Figure 4.3 (a) and (b). Adhesive residues are observed on both surfaces of the parts, which is indicative of good surface preparation. The wet lay-up repairs show a considerable variation in the failure load and the fracture plane for dry and hot-wet specimens, as shown in Figures (c) and (d). The fracture plane for the conditioned wet lay-up repairs is nearly perpendicular to the loading direction, which is expected due to very low repair strength, just as the damaged specimen shown in Figure 3.5.

Like in the step repaired specimens in Chapter 3, there is no debond between the outermost layer and the reinforcement layer since they are in the same direction, having similar stiffness values.

4.4 Defect Evaluation

After the mechanical testing, 35 X 15 mm slices were cut out from the repair zone, as shown in Figure 4.1. These slices were first ultrasonically and then microscopically evaluated in terms of porosity.

Ultrasonic Inspection: As described in Chapter 2, before the repair processes, all the panels were inspected with AUTT (Automatic Ultrasonics Through Transmission) and verified by comparing the parts with an inspection reference panel (IRP) having a porosity level below % 0.5. So, it is assumed that the regions away from the repair zone have a negligible porosity level on the repaired specimens.

For the inspection of the slices, the contact MUPE (Manual Ultrasonic Pulse-Echo) method was used using a 5 MHz frequency and 6.35 mm diameter probe. On all MUPE inspections, an ultrasonic gel is applied on the surface to enhance the sound transmission to the part.

To evaluate the porosity level in the specimens, the first step is to make the sensitivity calibration. For this purpose, the probe is placed in a region on the specimen known to be sound, and the obtained back wall echo is set to 80 % screen

height, and the corresponding decibel (dB) value is recorded. Then, slices from 6 prepreg repaired and 6 wet lay-up repaired specimens were inspected. After applying the gel couplant, the probe is placed on the surface of the slices and scanned the area. The appearance of a clear intermediate echo (any echo before the back wall echo) and a reduction or loss of the back-wall echo indicate delamination. Likewise, any debond is detected by an increase in the bond-line echo and a corresponding decrease in the back-wall echo. These types of echoes were not detected during the inspections, which ensured no delamination or de-bond.

To evaluate the volume porosity of the repaired section, the back-wall signal coming from the repair is set to 80 % of the screen height, and the corresponding decibel value is recorded. The difference between this dB value and the previous dB value obtained from the sensitivity calibration is calculated and named the attenuation value (ΔdB). This value is directly related to the porosity content of the inspected zone.

Porosity Evaluation: The slices are prepared and microscopically examined according to ASTM E3-11 [175] after the ultrasonic inspection. After a diamond-coated cutting blade cut the specimen, the surfaces were cleaned thoroughly. Then the samples were mounted in cold-curing epoxy resin and ground with different grit SiC papers to remove the scratches and surface defects. At last, the surfaces were polished with 3 μm and 1 μm diamond paste. Finally, an Olympus GX53 Inverted Microscope imaged the cross-sections, and the Olympus Stream Essentials software package [176] measured the patch porosity through image processing.

During the evaluation, fractured surfaces are excluded from the measurements to get the pre-test porosity values. The threshold value for the porosity area is selected as 0.01 $mm^{2,}$ and the porosity content is evaluated according to Eqn. (3.2).

Figure 4.4 and Figure 4.5 show representative views of the cross-sectional morphology of prepreg and wet lay-up repairs, respectively. P1, P2, P3, W1, W2, and W3 are the dry specimens, and P4, P5, P6, W4, W5, and W6 are the hot-wet specimens. By looking at the microscopic views, it can be easily seen that the parent

laminate is free of porosity, whereas the repair patch and the adhesive include various porosities. The porosities are mainly located in adhesive-rich zones and inter-fiber regions of the repair patch. The porosity levels for the prepreg repairs are found to be higher than the wet lay-up repairs. The area of the porosities varies between 0.01 mm^2 to 1 mm^2 for the prepreg repairs and 0.01 mm^2 to 0.7 mm^2 for the wet lay-up repairs.

The results of the ultrasonic inspection, microscopic porosity evaluation, and the related tensile experimental test results are summarized in Table 4.3. Also, in Figure 4.6, the correlation between the ultrasonic attenuation value and the microscopically found volume porosity percent is given. By looking at Table 4.3 and Figure 4.6, it is clear that as the porosity percent increases, ΔdB value also increases and can be as high as 20 dB for a porosity percentage of 5.25 %.

It is not easy to establish a direct correlation between the strength value and the porosity percent by looking at these experimental results for these very close porosity levels. Also, there is no significant strength reduction for these relatively low porosity levels (less than approximately 5 %) in parallel with the numerical findings of Chapter 2 and the experimental findings of Chapter 4.

The porosity amount, distribution, or sizes show no significant difference between the hot-wet and dry specimens.

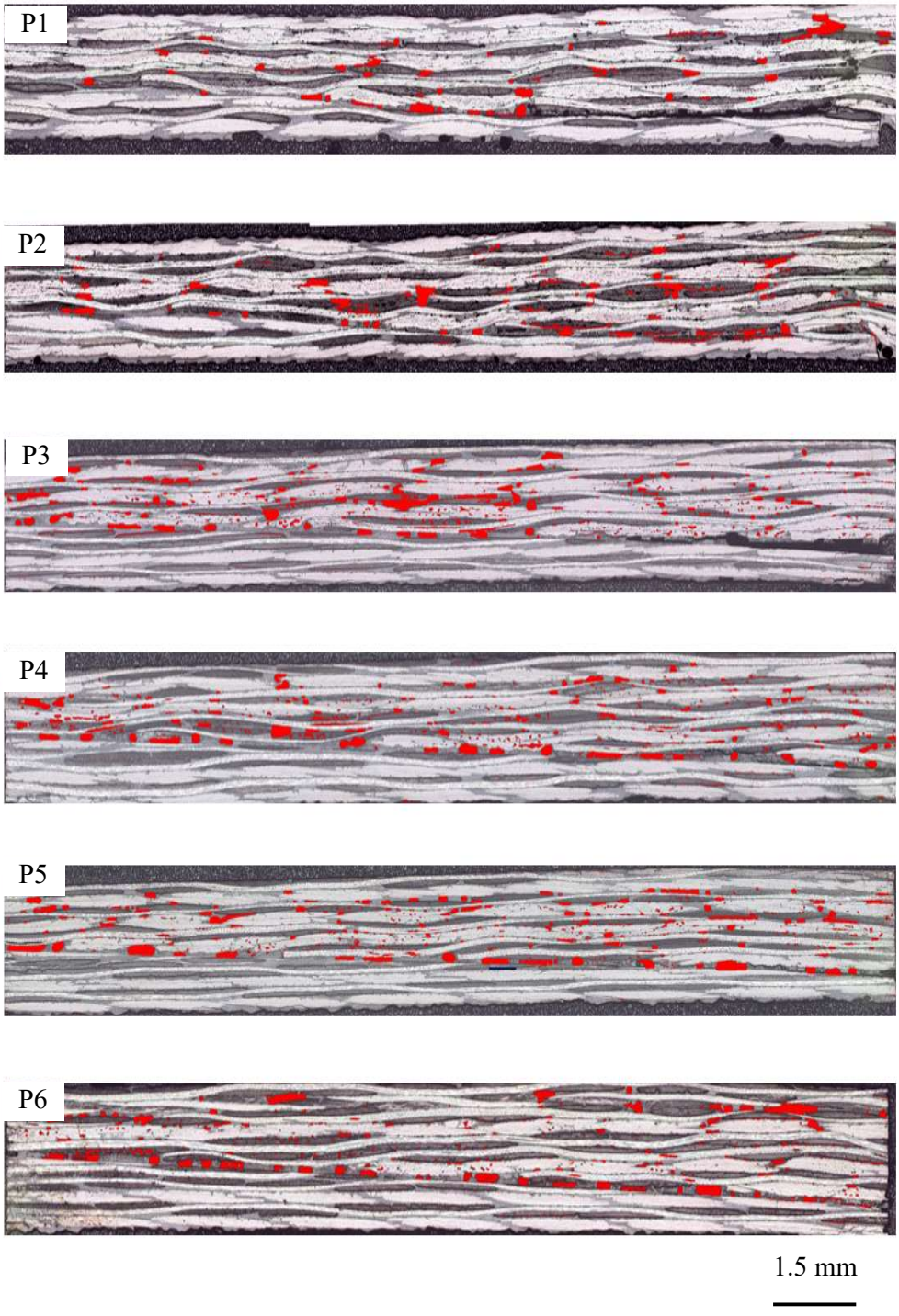

Figure 4.4. Optical micrographs of the prepreg repaired specimens. Red regions mark the porosities.

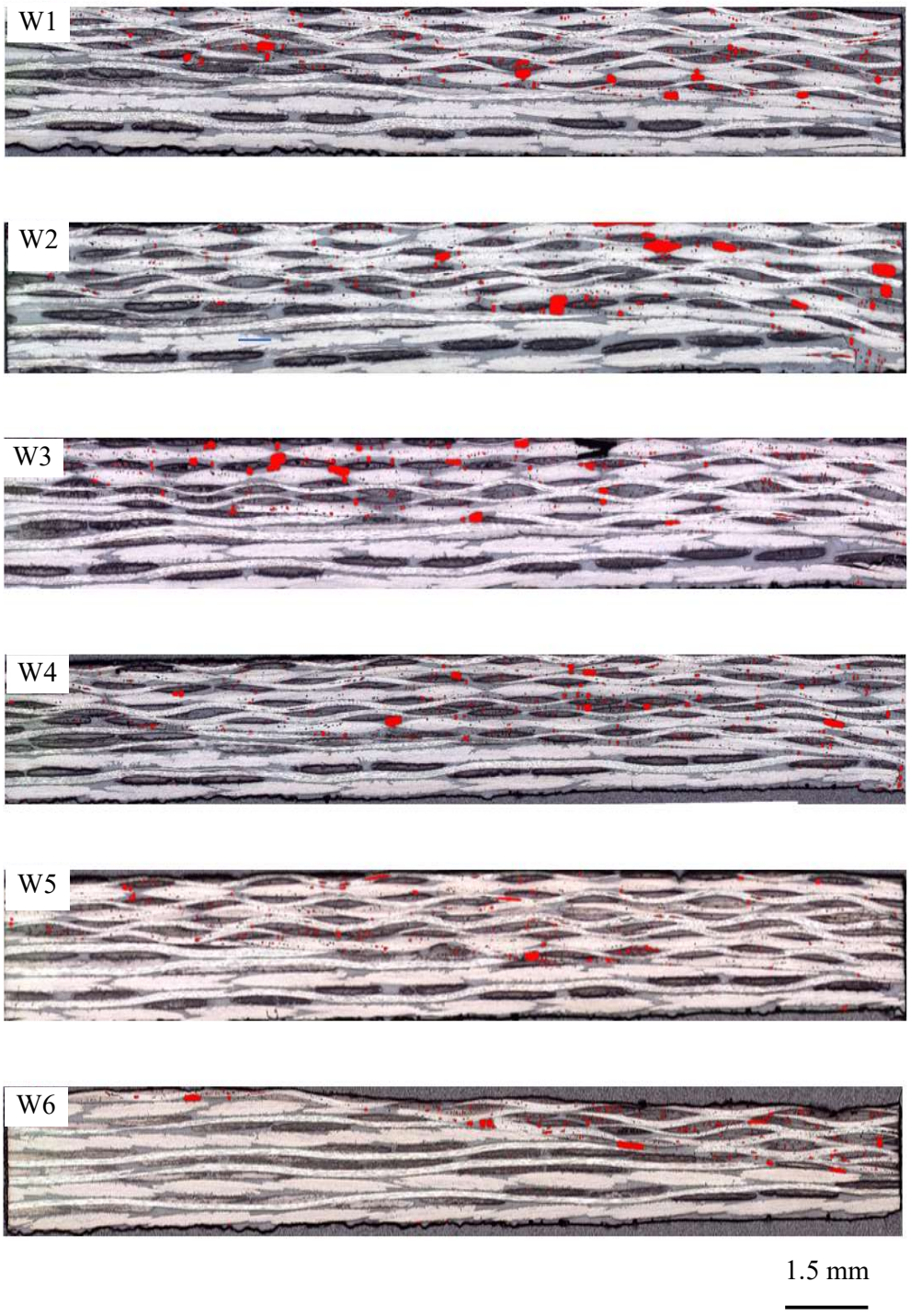

Figure 4.5. Optical micrographs of the wet lay-up repaired specimens. Red regions mark the porosities.

Table 4.3. Results of the ultrasonic inspection, microscopic porosity evaluation, and mechanical testing.

Specimen #	ΔdB (±1)	% Porosity	Strength (MPa)
Prepreg 1 (P1)	14	3.75	393
Prepreg 2 (P2)	12	3.57	408
Prepreg 3 (P3)	20	5.25	365
Prepreg 4 (P4)	16	4.67	390
Prepreg 5 (P5)	18	5.05	385
Prepreg 6 (P6)	16	4	417
Wet lay-up 1(W1)	8	1.66	335
Wet lay-up 2(W2)	8	2	321
Wet lay-up 3(W3)	6	1.5	344
Wet lay-up 4(W4)	5	1.41	235
Wet lay-up 5(W5)	4	0.98	230
Wet lay-up 6(W6)	4	1.03	232

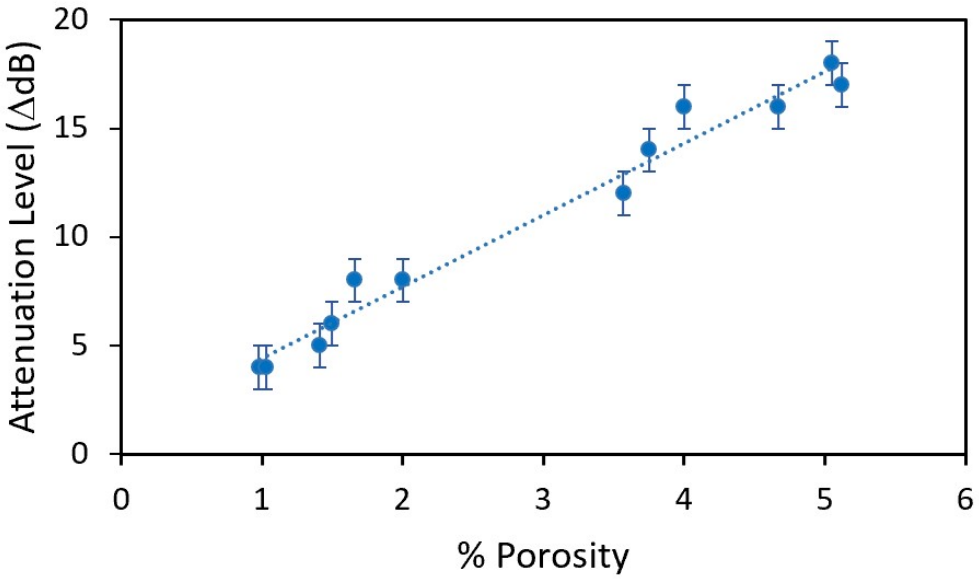

Figure 4.6. The measured ultrasonic attenuation values for specimens with different porosity levels.

4.5 Conclusion

To evaluate the combined effect of the moisture and temperature on the repair strength, mechanical tensile tests have been performed for unconditioned and hot-wet specimens. In addition, all repairs were cured with an out-of-autoclave process to simulate the on-site repair scenarios. The experimental measurements on scarf repaired laminates with a 3.8° scarf angle showed that the strength recovery could be as high as 68% for the prepreg repairs and 59 % for the wet lay-up repairs for unconditioned specimens.

The repair strength for the hot-wet specimens was also evaluated with mechanical tests. It is found that, although the strength of the prepreg repairs did not show any reduction, the wet lay-up repair systems were significantly affected by the combined effect of the post-bond moisture intake and the test temperature. As a result, their strength was as low as the damaged specimen strength, which shows the inefficiency

of the wet lay-up repairs under hot-wet conditions. Therefore, it can be concluded that the wet lay-up repairs should be used temporarily.

The porosity levels of the selected prepreg and wet lay-up specimens are investigated with ultrasonic inspection and microscopical evaluation methods. A porosity-attenuation curve was constructed for the used repair material-process couple regarding the ultrasonic inspection and microscopical evaluation results. It is evident that the ultrasonic attenuation value increases as the porosity level increases. By looking at the strength-porosity percent data, no relation could be established since the values are very close to each other.

There is no significant strength reduction for the relatively low porosity levels (less than approximately 5 %) in parallel with the numerical findings of Chapter 2 and the experimental findings of Chapter 4. In addition, the porosity amount, distribution, or sizes show no significant difference between the hot-wet and dry specimens.

CHAPTER 5

CONCLUSIONS AND FUTURE WORK

Experimental and numerical methods for adhesively bonded scarf joints and scarf/ stepped repairs were reviewed, applied, and evaluated. The experimental outputs of the study can be summarized as follows:

- The repair process is greatly dependent on process and workmanship. Any deviation from the standardized rules leads to unsuccessful repairs.
- All repair systems were implemented on panels manufactured from a new generation composite M21/AS4C by an autoclave process under 180°C and 7 bars during the study. The reason beneath the use of M21/AS4C as a base material is its extensive usage in civil and military aircraft due to its high strength and toughness values.
- To characterize the behavior of scarf bonded joints under tension, tensile tests have been performed on secondary bonded CFRP laminates with different scarf angles. FM-300K film adhesive, cured at 180°C and 3.1 bars at autoclave, gave efficient bonding strength as far as the proper repair geometry is selected. It is found that the joint strength increases as the scarf angle decrease. Strength recovery may be as high as 88 %, with a scarf angle of 1.9. For an angle of 5.7°, cohesive failure occurs within the adhesive, whereas for 1.9°, the laminate structure fails without considerable damage in the bond area. The scarf angle of 2.8° exhibited a mixed response – a combination of laminate failure and cohesive failure.
- To characterize the behavior of stepped repaired panels under tension, tests have been performed on two different co-bonded repair systems: prepreg repair and wet lay-up repair. For the prepreg repairs, M21/AS4C

prepregs are used as repair plies, and they were bonded to pre-manufactured panels with FM300-K film adhesive. FM300-K film adhesive is selected since its high strength and compatible cure cycle with M21/AS4C's. The repaired panels were cured out-of-autoclave at 180°C and under vacuum pressure only.

For the wet lay-up repairs, Hexforce G0904 D 1070 TCT plain weave dry carbon fabric impregnated with HYSOL EA 9396 two-part adhesive is selected as the repair plies. The impregnated layers were bonded to the panels with HYSOL EA 9396 two-part adhesive and cured with an out-of-autoclave process at 65°C and under vacuum pressure only. These repair materials are selected due to their widespread usage in the aerospace industry.

Both repair systems were satisfactory for repairing M21/AS4C composite laminates based on the test results. The strength recovery rate for the stepped repairs with 6.25 mm step lengths can be as high as 76 % for the prepreg repairs and 66 % for the wet lay-up repairs. In addition, the laminate structure fails from outside of the repair in the prepreg repairs, indicating high bond strength. In contrast, failure occurred at the repair region in the wet lay-up repairs and then spread to the parent laminate, leading to a complete failure. These results indicate that prepreg repairs are more effective than wet lay-up repairs for step repairs under normal environmental conditions.

- To investigate the durability of the repairs under severe environmental conditions, mechanical tensile tests have been performed for unconditioned and hot-wet specimens. For this purpose, 3.8 ° scarfed repaired panels are selected. The repaired specimens were conditioned and tested at 70°C to simulate the environmental conditions.

  It is found that, although the strength of the prepreg repairs did not show any reduction, the wet lay-up repair systems were significantly affected by the combined effect of post-bond moisture and the temperature. As a

result, the strength of the wet lay-up repairs was as low as the damaged specimen strength, which shows the inefficiency of the wet lay-up repairs under hot-wet conditions. Therefore, it can be concluded that wet lay-up systems shall be used as temporary repairs only as they cannot withstand severe environmental conditions.

- The porosity levels of the selected prepreg and wet lay-up specimens are investigated with ultrasonic inspection and microscopical evaluation methods. A porosity-attenuation curve was constructed for the used repair material-process couple regarding the ultrasonic inspection and microscopical evaluation results. It is evident that the ultrasonic attenuation value increases as the porosity level increases, but by looking at the strength-porosity percent data, no direct relationship could be established since the values are very close to each other. However, it can be concluded that, up to 5 % porosity content, the tensile strength of the repairs is not affected significantly.
- Due to the closed geometry of the scarf or stepped repairs, it is challenging to evacuate the volatiles and gaseous during the cure cycle for out-of-autoclave repairs. In addition, the geometry makes the pulse-echo ultrasonic inspection very challenging. Therefore, well-experienced inspectors technicians should do the repair and inspection
- DCB and ENF tests have been performed to find the fracture toughness values of FM-300K and HYSOL EA-9396 to implement numerical modeling. Although tests have been performed according to ASTM and EN specifications, results from EN tests were used in the numerical modeling since they are more conservative and consistent. In addition, test specimens were prepared in the same way with the repairs, different from the conventional methods given in the literature.

The numerical outputs of the study can be summarized as follows:

- The developed numerical simulation very well predicted the experimental behavior with a slight overprediction in the failure loads and a similar failure mode obtained for both 2-D scarf joints and 3-D stepped repairs.
- To model progressive failure of the woven fabric composites using the FEM, Abaqus requires modifications. The development and implementation of the USDFLD subroutine in Abaqus enabled the analysis of the simulation of the woven fabric composite by using solid elements. This helped to simulate the stresses in 3 directions.
- The detailed stress distribution analysis on the 2-D scarf joints provided further insight into the problem. It showed that stress concentration plays an essential role in the failure behavior of the specimens. The most critical region of the bond area corresponds to the 0°-plies, where the adhesive-adherent stiffness mismatch is highest.
- Analysis of the bond-line defects showed that a defect density of about 10% reduces the tensile strength by almost 20%, demonstrating the importance of the repair quality in achieving desirable mechanical performance.
- The effect of shear strength and fracture toughness values of the CZM modeling is investigated numerically for the stepped repairs. It is found that, up to a certain level of cohesive strength, the failure load directly increases with the increasing strength of the adhesive. However, after the bond strength is equal to the laminate strength, increasing the adhesive strength has no beneficial effect on the repair strength.

- The benefit of using an extra reinforcement layer on the repair strength is evaluated numerically considering different ply orientations. Using an extra layer decreases the peak stress on the adhesive but choosing a differently oriented layer than the uppermost layer of the parent laminate creates undesired peel stresses on the edge of the repair.

The following research problems can be considered as possible extensions of the current work.

- The fatigue performance of the repairs may be investigated.
- Enhanced methods for out-of-autoclave cures may be studied to decrease the porosity content.
- Structural Health Monitoring (SHM) of the repaired parts may be investigated to overcome the difficulties encountered in the ultrasonic inspection.

REFERENCES

[1] Hale J. Boeing 787 from the Ground Up .Aero Magazine Boeing; 24. 2020.

[2] Anon."A350 XWB Intelligent and aerodynamic airframe", Airbus International 2012.

[3] Boeing 787-8 Structural Repair Manual. Boeing Co 2012.

[4] Airbus A320 Structural Repair Manual 2019.

[5] Baker AL. Joining and repair of aircraft composite structures 1996.

[6] Hinton M, Kaddour AS, Soden P. Failure Criteria in Fibre-Reinforced-Polymer Composites: The World-Wide Failure Exercise. 2004.

[7] Soden PD, Hinton MJ, Kaddour AS. A comparison of the predictive capabilities of current failure theories for composite laminates. Composites Science and Technology 1998; 58:1225–54.

[8] Soden PD, Hinton MJ, Kaddour AS. Lamina properties, lay-up configurations and loading conditions for a range of fibre-reinforced composite laminates. Composites Science and Technology 1998; 58:1011–22.

[9] Soden PD, Kaddour AS, Hinton MJ. Recommendations for designers and researchers resulting from the world-wide failure exercise. Composites Science and Technology 2004; 64:589–604.

[10] Kaddour AS, Hinton MJ, Soden PD. A comparison of the predictive capabilities of current failure theories for composite laminates: additional contributions. Composites Science and Technology 2004; 64:449–76.

[11] Tsai SW, Wu EM. A General Theory of Strength for Anisotropic Materials. Journal of Composite Materials 1971; 5:58–80.

[12] Cuntze RG, Freund A. The predictive capability of failure mode concept-based strength criteria for multidirectional laminates. Composites Science and Technology 2004; 64:343–77.

[13] Puck A, Schürmann H. Failure analysis of FRP laminates by means of physically based phenomenological models. Composites Science and Technology 1998; 58:1045–67.

[14] Bogetti TA, Hoppel CPR, Harik VM, Newill JF, Burns BP. Chapter 5.12 - Predicting the nonlinear response and failure of composite laminates: Correlation with experimental results. Oxford: Elsevier; 2004, p. 961–75.

[15] Davila C, Jaunky N, Goswami S. Failure criteria for FRP laminates in plane stress. 44th AIAA/ASME/ASCE/AHS/ASC Structures, Structural Dynamics, and Materials Conference, 2003, p. 1991.

[16] C.G. Davila, P.P. Camanho, C.A. Rose. Failure criteria for FRP laminates. J. Compos. Materials 2005;4: 323-345. n.d.

[17] Pinho ST, Dávila CG, Camanho PP, Iannucci L, Robinson P. Failure Models and Criteria for FRP Under-In-Plane or Three-Dimensional Stress States Including Shear Non-Linearity 2005.

[18] Pinho ST, Darvizeh R, Robinson P. Material and structural response of polymer-matrix fibre-reinforced composites 2012; 46: 2313-2341.

[19] Sandhu RS. A Survey of Failure Theories of Isotropic and Anisotropic Materials, AFFDL-TR-72-71,1972. 1972. Journal of Composite Materials.

[20] Azzi VD, Tsai SW. Anisotropic strength of composites. Experimental Mechanics 1965; 5:283–8.

[21] Hashin Z. Failure Criteria for Unidirectional Fiber Composites. J Appl Mech 1980; 47:329–34.

[22] Yamada S, Sun C. Analysis of Laminate Strength and Its Distribution 1978.

[23] Hill R. A theory of the yielding and plastic flow of anisotropic metals. Proc R Soc Lond A 1948; 193:281–97. https://doi.org/10.1098/rspa.1948.0045.

[24] Tsai SW, Hahn HT. Introduction to composite materials 1980.

[25] Soden PD, Hinton MJ, Kaddour AS. Biaxial test results for strength and deformation of a range of E-glass and carbon fibre reinforced composite laminates: failure exercise benchmark data. Composites Science and Technology 2002; 62:1489–514.

[26] Knigth NF. Factors Influencing Progressive Failure Analysis Predictions for Laminated Composite Structure. 10.2514/6.2008-2108

[27] Talreja R. A continuum mechanics characterization of damage in composite materials. Proceedings of the Royal Society of London Mathematical and Physical Sciences 1985; 399:195–216.

[28] Talreja R. Continuum modelling of damage in ceramic matrix composites. Mechanics of Materials 1991; 12: 165–80.

[29] Talreja R. Damage development in composites: mechanisms and modelling. The Journal of Strain Analysis for Engineering Design 1989; 24:215–22.

[30] Chang, FK, Chang, KY. A Progressive Damage Model for Laminated Composites Containing Stress Concentrations, Journal of Composite Materials, Vol. 21, No. 9, 1987, pp. 834-855. n.d.

[31] Shahid I, Chang F-K. An accumulative damage model for tensile and shear failures of laminated composite plates. Journal of Composite Materials 1995; 29:926–81.

[32] Barbero EJ, Lonetti P. An inelastic damage model for fiber reinforced laminates. Journal of Composite Materials 2002; 36:941–62.

[33] Ladeveze P, LeDantec E. Damage modelling of the elementary ply for laminated composites. Composites Science and Technology 1992; 43:257–67.

[34] Matzenmiller A, Lubliner J, Taylor RL. A constitutive model for anisotropic damage in fiber-composites. Mechanics of Materials 1995; 20:125–52.

[35] Abaqus Unified FEA - SIMULIA™ by Dassault Systèmes® 2019.

[36] Sleight W. Sleight DW. Progressive Failure Analysis Methodology for laminated Composite Structures. M.S. Thesis, Old Dominion University,1996. n.d.:92.

[37] Gul Apalak Z, Kemal Apalak M, Serdar Genc M. Progressive damage modeling of an adhesively bonded composite single lap joint under flexural loads at the mesoscale level. Journal of Reinforced Plastics and Composites 2007; 26:903–53.

[38] Tserpes KI, Labeas G, Papanikos P, Kermanidis T. Strength prediction of bolted joints in graphite/epoxy composite laminates. Composites Part B: Engineering 2002; 33:521–9.

[39] Tan P, Tong L, Steven GP. Modelling for predicting the mechanical properties of textile composites—A review. Composites Part A: Applied Science and Manufacturing 1997; 28:903–22.

[40] Reddy YSN, Moorthy CD, Reddy JN. Non-linear progressive failure analysis of laminated composite plates. International Journal of Non-Linear Mechanics 1995; 30:629–49.

[41] Petit PH, Waddoups ME. A method of predicting the nonlinear behavior of laminated composites. Journal of Composite Materials 1969; 3:2–19.

[42] Sandhu RS. Nonlinear behavior of unidirectional and angle ply laminates. Journal of Aircraft 1976; 13:104–11.

[43] Hahn HT, Tsai SW. On the behavior of composite laminates after initial failures. Journal of Composite Materials 1974; 8:288–305.

[44] Raju IS, Wang JT. Classical laminate theory models for woven fabric composites. Journal of Composites, 1994;16:289–303.

[45] Jebri L, Abbassi F, Demiral M, Soula M, Ahmad F. Experimental and numerical analysis of progressive damage and failure behavior of carbon Woven-PPS. Composite Structures 2020;243.

[46] Cai D, Zhou G, Wang X, Li C, Deng J. Experimental investigation on mechanical properties of unidirectional and woven fabric glass/epoxy composites under off-axis tensile loading. Polymer Testing 2017; 58:142–52.

[47] Cai D, Tang J, Zhou G, Wang X, Li C, Silberschmidt VV. Failure analysis of plain-woven glass/epoxy laminates: Comparison of off-axis and biaxial tension loadings. Polymer Testing 2017; 60:307–20.

[48] Wang L, Wu J, Chen C, Zheng C, Li B, Joshi SC, et al. Progressive failure analysis of 2D woven composites at the meso-micro scale. Composite Structures 2017; 178:395–405.

[49] Ishikawa T, Chou T-W. Stiffness and strength behaviour of woven fabric composites. Journal of Materials Science 1982; 17:3211–20.

[50] Cox B. Failure Models for Textile Composites. NASA Report no:4686,1995.

[51] Poe Jr CC, Dexter HB, Raju IS. Review of the NASA textile composites research. Journal of Aircraft 1999; 36:876–84.

[52] Johnson W, Masters J, Lagace P, Naik N, Shembekar P, Hosur M. Failure Behavior of Woven Fabric Composites. J Compos Technol Res 1991; 13:107.

[53] Naik NK, Ganesh VK. An analytical method for plain weave fabric composites. Composites 1995; 26:281–9.

[54] ASTM D5573-99 Standard Practice for Classifying Failure Modes in Fiber-Reinforced-Plastic (FRP) Joints. ASTM International.

[55] Volkersen. Die Niektraftverteilung in Zugbeanspruchten mit Konstanten Laschenquerschritten. Luftfahrtforschung 15, 1938, pp. 41-47.

[56] Da Silva LF, Lima RF, Teixeira RM, Puga A. Closed-form solutions for adhesively bonded joints. " Development of the Software for the Design of Adhesive Joints"] University of Porto, Portugal 2008.

[57] Goland M, Reissner E. “The Stresses in Cemented Joints,” Journal of Applied Mechanics 11, 1944, pp. A17-A27.

[58] Hart-Smith LJ. NASA-CR-112235: Adhesive-bonded double-lap joints. 1973.

[59] Hart-Smith LJ. NASA-CR-112236 Adhesive Bonded Single Lap Joints. 1973.

[60] Hart-Smith LJ. NASA-CR-112237: Adhesive-bonded scarf and stepped-lap joints. 1973.

[61] Tsai MY, Oplinger DW, Morton J. Improved theoretical solutions for adhesive lap joints. International Journal of Solids and Structures 1998; 35:1163–85.

[62] Mortensen F, Thomsen OT. Simplified linear and non-linear analysis of stepped and scarfed adhesive-bonded lap-joints between composite laminates. Composite Structures 1997; 38:281–94.

[63] Gleich DM, Van Tooren MJL, De Haan PAJ. Shear and peel stress analysis of an adhesively bonded scarf joint. Journal of Adhesion Science and Technology 2000; 14:879–93.

[64] Gleich DM, Van Tooren MJL, Beukers A. Analysis and evaluation of bondline thickness effects on failure load in adhesively bonded structures. Journal of Adhesion Science and Technology 2001; 15:1091–101.

[65] Ahn S-H, Springer GS. Repair of Composite Laminates-II: Models. Journal of Composite Materials 1998; 32:1076–114.

[66] Harman AB, Wang CH. Improved design methods for scarf repairs to highly strained composite aircraft structure. Composite Structures 2006; 75:132–44.

[67] Gunnion AJ, Herszberg I. Parametric study of scarf joints in composite structures. Composite Structures 2006; 75:364–76.

[68] Wang CH, Duong CN. Chapter 4 - Design of scarf and doubler-scarf joints. Bonded Joints and Repairs to Composite Airframe Structures, Oxford: Academic Press; 2016, p. 83–112.

[69] Adams RD, Comyn J, Wake WC. Structural Adhesive Joints in Engineering. 2nd ed. Springer Netherlands; 1997.

[70] Greenwood L, Boag TG, McLaren AS. Stress distribution in lap joints. Adhes Fundam Pract 1969; 10:273–9.

[71] Banea MD, da Silva LFM. Adhesively bonded joints in composite materials: An overview. Proceedings of the Institution of Mechanical Engineers, Part L: Journal of Materials: Design and Applications 2009;223:1–18.

[72] Harris JA, Adams RA. Strength prediction of bonded single lap joints by non-linear finite element methods. International Journal of Adhesion and Adhesives 1984; 4:65–78. https://doi.org/10.1016/0143-7496(84)90103-9.

[73] da Silva LFM, das Neves PJC, Adams RD, Wang A, Spelt JK. Analytical models of adhesively bonded joints—Part II: Comparative study. International Journal of Adhesion and Adhesives 2009; 29:331–41.

[74] Wang CH, Chalkley P. Plastic yielding of a film adhesive under multiaxial stresses. International Journal of Adhesion and Adhesives 2000; 20:155–64.

[75] Bowden PB, Jukes JA. The plastic flow of isotropic polymers. Journal of Materials Science 1972; 7:52–63.

[76] Dean G, Crocker LE. Comparison of the measured and predicted deformation of an adhesively bonded lap-joint specimen. 2000.

[77] Campilho RDSG. Strength Prediction of Adhesively-Bonded Joints. CRC Press; 2017.

[78] Charalambides M, Kinloch AJ, Wang Y, Williams JG. On the analysis of mixed-mode failure. International Journal of Fracture 1992; 54:269–91.

[79] Kin Loch AJ, Shaw SJ. The fracture resistance of a toughened epoxy adhesive. The Journal of Adhesion 1981; 12:59–77.

[80] Dugdale D. Yielding of steel sheets containing slits. J Mech Phys Solids,1960 8(2):100–104 n.d.

[81] Heide-Jørgensen S, Teixeira de Freitas S, Budzik MK. On the fracture behaviour of CFRP bonded joints under mode I loading: Effect of supporting carrier and interface contamination. Composites Science and Technology 2018; 160:97–110. https://doi.org/10.1016/j.compscitech.2018.03.024.

[82] Sørensen BF, Jacobsen TK. Characterizing delamination of fibre composites by mixed mode cohesive laws. Composites Science and Technology 2009; 69:445–56.

[83] Khoramishad H, Crocombe AD, Katnam KB, Ashcroft IA. Predicting fatigue damage in adhesively bonded joints using a cohesive zone model. International Journal of Fatigue 2010; 32:1146–58.

[84] Barenblatt G. The mathematical theory of equilibrium cracks in brittle fracture. In: HL Dryden GKFvdD Thvon K´arm´an, Howarth L (eds) Advances in Applied Mechanics,1962, vol Volume 7, Elsevier, pp 55–129 n.d.

[85] Hillerborg A, Modéer M, Petersson P-E. Analysis of crack formation and crack growth in concrete by means of fracture mechanics and finite elements. Cement and Concrete Research 1976; 6:773–81.

[86] Alves DL, Campilho RDSG, Moreira RDF, Silva FJG, da Silva LFM. Experimental and numerical analysis of hybrid adhesively-bonded scarf joints. International Journal of Adhesion and Adhesives 2018; 83:87–95.

[87] Balzani C, Wagner W, Wilckens D, Degenhardt R, Büsing S, Reimerdes H-G. Adhesive joints in composite laminates— A combined numerical/experimental estimate of critical energy release rates. International Journal of Adhesion and Adhesives 2012; 32:23–38.

[88] Cabello M, Turon A, Zurbitu J, Renart J, Sarrado C, Martínez F. Progressive failure analysis of DCB bonded joints using a new elastic foundation coupled with a cohesive damage model. European Journal of Mechanics - Solids 2017; 63:22–35.

[89] Camanho P. Mixed-Mode Decohesion Finite Elements for the Simulation of Delamination in Composite Materials. Composite Materials 2002:42.

[90] Camanho PP, Davila CG, de Moura MF. Numerical Simulation of Mixed-Mode Progressive Delamination in Composite Materials. Journal of Composite Materials 2003; 37:1415–38.

[91] Campilho RDSG, Banea MD, Neto JABP, da Silva LFM. Modelling adhesive joints with cohesive zone models: effect of the cohesive law shape of the adhesive layer. International Journal of Adh. and Adhes. 2013; 44:48–56.

[92] Campilho RDSG, de Moura MFSF, Pinto AMG, Morais JJL, Domingues JJMS. Modelling the tensile fracture behaviour of CFRP scarf repairs. Composites Part B: Engineering 2009; 40:149–57.

[93] Campilho RDSG, Fernandes TAB. Comparative Evaluation of Single-lap Joints Bonded with Different Adhesives by Cohesive Zone Modelling. Procedia Engineering 2015; 114:102–9.

[94] Campilho R, Moura M, Domingues J. Using a cohesive damage model to predict the tensile behaviour of CFRP single-strap repairs. Int J Solids Struct 2008; 45:1497–512. n.d.

[95] Cheng X, Zhang Q, Zhang J, Guo X, Niu Z. Parameters prediction of cohesive zone model for simulating composite/adhesive delamination in hygrothermal environments. Composites Part B: Engineering 2019; 166:710–21.

[96] Floros IS, Tserpes KI, Löbel T. Mode-I, mode-II and mixed-mode I+II fracture behavior of composite bonded joints: Experimental characterization and numerical simulation. Composites Part B: Engineering 2015; 78:459–68.

[97] Girolamo D, Davila CG, Leone FA, Lin S-Y. Cohesive Laws and Progressive Damage Analysis of Composite Bonded Joints, a Combined Numerical/Experimental Approach. 56th AIAA/ASCE/AHS/ASC Structures, Structural Dynamics, and Materials Conference 2015.

[98] Truong V-H, Kwak B-S, Roy R, Kweon J-H. Cohesive zone method for failure analysis of scarf patch-repaired composite laminates under bending load. Composite Structures 2019; 222:110895.

[99] Turon A, Costa J, Camanho PP, Dávila CG. Simulation of delamination in composites under high-cycle fatigue. Composites Part A: Applied Science and Manufacturing 2007; 38:2270–82.

[100] Benzeggagh ML, Kenane M. Measurement of mixed-mode delamination fracture toughness of unidirectional glass/epoxy composites with mixed-mode bending apparatus. Composites Science and Technology 1996; 56:439–49.

[101] ASTM D5528-13 Standard test method for mode I interlaminar fracture toughness of unidirectional fiber-reinforced polymer matrix composites. ASTM 2013. ASTM D5528-94a 1994.

[102] DIN EN 6033 - Aerospace series - Carbon fibre reinforced plastics - Test method; determination of interlaminar fracture toughness energy; mode I, G_{IC}

[103] ASTM D7905/D7905M, Standard test method for determination of the mode II interlaminar fracture toughness of unidirectional fiber-reinforced polymer matrix composites. ASTM 2014.

[104] DIN EN 6034 - Aerospace series - Carbon fibre reinforced plastics - Test method - Determination of interlaminar fracture toughness energy - Mode II - G[IIC]; German and English version EN 6034:2015.

[105] Bendemra H, Compston P, Crothers P. Optimisation study of tapered scarf and stepped-lap joints in composite repair patches. Composite Structures 2015;130.

[106] Kumar SB, Sridhar I, Sivashanker S, Osiyemi SO, Bag A. Tensile failure of adhesively bonded CFRP composite scarf joints. Materials Science and Engineering: B 2006; 132:113–20.

[107] Li J, Yan Y, Zhang T, Liang Z. Experimental study of adhesively bonded CFRP joints subjected to tensile loads. International Journal of Adhesion and Adhesives 2015; 57:95–104. https://doi.org/10.1016/j.ijadhadh.2014.11.001.

[108] Wang CH, Gunnion AJ. On the design methodology of scarf repairs to composite laminates. Composites Science and Technology 2008; 68:35–46.

[109] Yoo J-S, Truong V-H, Park M-Y, Choi J-H, Kweon J-H. Parametric study on static and fatigue strength recovery of scarf-patch-repaired composite laminates. Composite Structures 2016; 140:417–32.

[110] Xiaoquan C, Baig Y, Renwei H, Yujian G, Jikui Z. Study of tensile failure mechanisms in scarf repaired CFRP laminates. International Journal of Adhesion and Adhesives 2013; 41:177–85.

[111] Sui L, Zhidong G, Guo X, Jianhua C, Guofen X, Jing C. Tensile Behavior of Hybrid Plain Woven Fabric Laminate Repaired by Scarfing Method. Polymers and Polymer Composites 2013; 21:599–606.

[112] Darwish FH, Shivakumar KN. Experimental and Analytical Modeling of Scarf Repaired Composite Panels. Mechanics of Advanced Materials and Structures 2014; 21:207–12.

[113] Pinto AMG, Campilho RDSG, de Moura MFSF, Mendes IR. Numerical evaluation of three-dimensional scarf repairs in carbon-epoxy structures. International Journal of Adhesion and Adhesives 2010; 30:329–37.

[114] Soutis C, Hu FZ. Strength Analysis of Adhesively Bonded Repairs. In: Tong L, Soutis C, editors. Recent Advances in Structural Joints and Repairs for Composite Materials, Dordrecht: Springer Netherlands; 2003, p. 141–72.

[115] Boerio FJ, Roby B, Dillingham RG, Bossi RH, Crane RL. Effect of Grit-Blasting on the Surface Energy of Graphite/Epoxy Composites. The Journal of Adhesion 2006; 82:19–37. https://doi.org/10.1080/00218460500418516.

[116] Gude MR, Prolongo SG, Ureña A. Adhesive bonding of carbon fibre/epoxy laminates: Correlation between surface and mechanical properties. Surface and Coatings Technology 2012; 207:602–7.

[117] Yang G, Yang T, Yuan W, Du Y. The influence of surface treatment on the tensile properties of carbon fiber-reinforced epoxy composites-bonded joints. Composites Part B: Engineering 2019; 160:446–56.

[118] Jölly I, Schlögl S, Wolfahrt M, Pinter G, Fleischmann M, Kern W. Chemical functionalization of composite surfaces for improved structural bonded repairs. Composites Part B: Engineering 2015; 69:296–303.

[119] Sánchez Serrano J, Ureña A, Lazcano Ureña S, Blanco Varela T. New approach to surface preparation for adhesive bonding of aeronautical composites: atmospheric pressure plasma. Studies on the pretreatment lifetime and durability of the bondline. Composite Interfaces 2015; 22:731–42.

[120] Encinas N, Oakley BR, Belcher MA,, Abenojar J, et al. Surface modification of aircraft used composites for adhesive bonding. International Journal of Adhesion and Adhesives 2014; 50:157–63.

[121] Harder S, Schmutzler H, Hergoss P, de Freese J, Holtmannspoetter J, Fiedler B. Effect of infrared laser surface treatment on the morphology and adhesive properties of scarfed CFRP surfaces. Composites Part A Applied Science and Manufacturing 2019; 121:299–307.

[122] Reitz V, Meinhard D, Ruck S, Riegel H, Knoblauch V. A comparison of IR- and UV-laser pretreatment to increase the bonding strength of adhesively joined aluminum/CFRP components. Composites Part A: Applied Science and Manufacturing 2017; 96:18–27.

[123] Palmieri FL, Belcher MA, Wohl CJ, Blohowiak KY, Connell JW. Laser ablation surface preparation for adhesive bonding of carbon fiber reinforced

epoxy composites. International Journal of Adhesion and Adhesives 2016; 68:95–101.

[124] Kim K-S, Yoo J-S, Yi Y-M, Kim C-G. Failure mode and strength of uni-directional composite single lap bonded joints with different bonding methods. Composite Structures 2006; 72:477–85.

[125] Erdogan F, Ratwani M. Stress distribution in bonded joints. Journal of Composite Materials 1971; 5:378–93.

[126] Breitzman TD, Iarve EV, Cook BM, Schoeppner GA, Lipton RP. Optimization of a composite scarf repair patch under tensile loading. Composites Part A 2009; 12:1921–30.

[127] Feng W, Xu F, Yuan J, Zang Y, Zhang X. Focusing on in-service repair to composite laminates of different thicknesses via scarf-repaired method. Composite Structures 2019; 207:826–35.

[128] Ahn S-H, Springer GS. Repair of Composite Laminates, DOT/FAA/AR-00/46,2000 n.d.:85.

[129] Liao L, Huang C, Sawa T. Effect of adhesive thickness, adhesive type and scarf angle on the mechanical properties of scarf adhesive joints. International Journal of Solids and Structures 2013; 50:4333–40.

[130] Afendi M, Teramoto T, Bakri HB. Strength prediction of epoxy adhesively bonded scarf joints of dissimilar adherends. International Journal of Adhesion and Adhesives 2011; 31:402–11.

[131] Banea MD, da Silva LFM. Adhesively bonded joints in composite materials: An overview. Proceedings of the IMechE 2009; 223:1–18.

[132] Campilho RD, Moura DC, Banea MD, da Silva LFM. Adhesive thickness effects of a ductile adhesive by optical measurement techniques. International Journal of Adhesion and Adhesives 2015; 57:125–32.

[133] Banea MD, da Silva LFM. Mechanical Characterization of Flexible Adhesives. The Journal of Adhesion 2009; 85:261–85.

[134] Banea MD, da Silva LFM, Campilho RD. The effect of adhesive thickness on the mechanical behavior of a structural polyurethane adhesive. The Journal of Adhesion 2015; 91:331–46.

[135] da Silva LFM, Rodrigues TNSS, Figueiredo MAV, de Moura MFSF, Chousal JAG. Effect of Adhesive Type and Thickness on the Lap Shear Strength. The Journal of Adhesion 2006; 82:1091–115.

[136] da Silva LucasFM, Carbas RJC, Critchlow GW, Figueiredo MAV, Brown K. Effect of material, geometry, surface treatment and environment on the shear strength of single lap joints. International Journal of Adhesion and Adhesives 2009; 29:621–32.

[137] Feng W, Xu F, Yuan J, Zang Y, Zhang X. Focusing on in-service repair to composite laminates of different thicknesses via scarf-repaired method. Composite Structures 2019; 207:826–35.

[138] Dong C. Effects of Process-Induced Voids on the Properties of Fibre Reinforced Composites. Journal of Mat Science & Tech. 2016; 32:597–604

[139] Chong HM, Liu SL, Subramanian AS, Ng SP, Tay SW, Wang SQ, et al. Out-of-autoclave scarf repair of interlayer toughened carbon fibre composites using double vacuum debulking of patch. Composites Part A: Applied Science and Manufacturing 2018; 107:224–34.

[140] Tang J-M, Lee WI, Springer GS. Effects of Cure Pressure on Resin Flow, Voids, and Mechanical Properties. Journ. of Comp. Mat. 1987; 21:421–40.

[141] Préau M, Hubert P. Processing of co-bonded scarf repairs: Void reduction strategies and influence on strength recovery. Composites Part A: Applied Science and Manufacturing 2016; 84:236–45.

[142] MacLean A, Casari D, Hubert P. Wet layup composite bonded scarf repairs: effect of processing variables on porosity. SAMPE 2016.

[143] Salah L. Weak Interfacial Bonds and the Long-Term Durability of Bonded Repairs to Polymer Matrix Composites n.d.:188.

[144] ASTM E2533. Guide for Nondestructive Testing of Polymer Matrix Composites Used in Aerospace Applications. ASTM International.

[145] Howell PA. Nondestructive Evaluation (NDE) Methods and Capabilities Handbook. Nondestructive Evaluation 2020:216.

[146] Towsyfyan H, Biguri A, Boardman R, Blumensath T. Successes and challenges in non-destructive testing of aircraft composite structures. Chinese Journal of Aeronautics 2020; 33:771–91.

[147] Armstrong K, Cole W, Bevan G. Care and Repair of Advanced Composites. Care and Repair of Advanced Composites, SAE; 2005, p. i–xxviii.

[148] Sohn H, Farrar CR, Hemez FM, Shunk DD, Stinemates DW, Nadler BR, et al. A review of structural health monitoring literature: 1996–2001. Los Alamos National Laboratory, USA 2003;1.

[149] Farrar CR, Worden K. An introduction to structural health monitoring. New Trends in Vibration Based Structural Health Monitoring 2010:1–17.

[150] Baker A, Jones, editors. Bonded Repair of Aircraft Structures. Springer Netherlands; 1988. https://doi.org/10.1007/978-94-009-2752-0.

[151] Adams DE. Health Monitoring of Structural Materials and Components. Chichester, UK: John Wiley & Sons, Ltd; 2007.

[152] Baker A, Gunnion AJ, Wang J, Chang P. Advances in the proof test for certification of bonded repairs – Increasing the Technology Readiness Level. International Journal of Adhesion and Adhesives 2016; 64:128–41.

[153] Hempe DW. Bonded Repair Size Limits. 2014.

[154] Bonded Repair Size Limits in accordance with CS-23, CS-25, CS-27, CS-29 and AMC 20-29.

[155] Warren KC, Lopez-Anido RA, Vel SS, Bayraktar HH. Progressive failure analysis of three-dimensional woven carbon composites in single-bolt, double-shear bearing. Composites Part B: Engineering 2016; 84:266–76.

[156] Key CT, Schumacher SC, Hansen AC. Progressive failure modeling of woven fabric composite materials using multicontinuum theory. Composites Part B: Engineering 2007; 38:247–57.

[157] Bhatia GS, Arockiarajan A. Fatigue studies on patch repaired carbon/epoxy woven composites. Composites Part B: Engineering 2019; 175:107121.

[158] Ghazali E, Dano M-L, Gakwaya A, Amyot C-O. Experimental and numerical studies of stepped-scarf circular repairs in composite sandwich panels. International Journal of Adhesion and Adhesives 2018; 82:41–9.

[159] Hayes-Griss JM, Gunnion AJ, Afaghi Khatibi A. Damage tolerance investigation of high-performance scarf joints with bondline flaws under various environmental, geometrical and support conditions. Composites Part A: Applied Science and Manufacturing 2016; 84:246–55.

[160] Hayes-Griss JM, Orifici AC, Khatibi AA. An improved progressive failure modelling and damage tolerant design methodology for composite scarf joints with bondline flaws. Composites Part A: Applied Science and Manufacturing 2020; 131:105776.

[161] Goh JY, Georgiadis S, Orifici AC, Wang CH. Effects of bondline flaws on the damage tolerance of composite scarf joints. Composites Part A: Applied Science and Manufacturing 2013; 55:110–9.

[162] Wu C, Chen C, He L, Yan W. Comparison on damage tolerance of scarf and stepped-lap bonded composite joints under quasi-static loading. Composites Part B: Engineering 2018; 155:19–30.

[163] Hexcel Composite Materials and Structures https://www.hexcel.com/ (accessed November 30, 2019). 2019.

[164] ASTM D3039, Standard test method for tensile properties of polymer matrix composite materials 2008

[165] ASTM F22-13, Standard test method for hydrophobic surface films by the water-break test ASTM International,2013.

[166] FM 300. https://www.solvay.com/en/product/fm-300 (accessed November 30, 2019). Solvay 2019.

[167] Jones J, Graves S. Repair Techniques for Celion/LARC-160 Graphite/Polyimide Composite Structures. NASA-CR-3794 1984. n.d.

[168] Turon A, Dávila CG, Camanho PP, Costa J. An engineering solution for mesh size effects in the simulation of delamination using cohesive zone models. Engineering Fracture Mechanics 2007; 74:1665–82.

[169] Girolamo D, Dávila C, Leone F, Lin S-Y. Cohesive Laws and Progressive Damage Analysis of Composite Bonded Joints, a Combined Numerical/Experimental Approach, 2015.

[170] Lee M, Yeo E, Blacklock M, Janardhana M, Feih S, Wang CH. Predicting the strength of adhesively bonded joints of variable thickness using a cohesive element approach. International Journal of Adhesion and Adhesives 2015; 58:44–52.

[171] Yarrington P, Zhang J, Collier C, Bednarcyk B. Failure analysis of adhesively bonded composite joints. 46th AIAA/ASME/ASCE/AHS/ASC Structures, Structural Dynamics and Materials Conference, 2005, p. 2376.

[172] X5000 Industrial 3D X-Ray Inspection System | North Star Imaging n.d.

[173] LOCTITE EA 9396 AERO https://www.henkel-adhesives.com/vn/en/product/adhesives/loctite_ea_9396_aero.html (accessed April 11, 2021).

[174] Tomblin J, Seneviratne W, Escobar P, Yoon-Khian Y. Shear stress-strain data for structural adhesives. Report No. DOT/FAA/AR-02/97 2002.

[175] ASTM E3-11 Guide for Preparation of Metallographic Specimens. ASTM International; 2017.

[176] Microscope Image Analysis Software | OLYMPUS Stream https:// www. olympus -ims.com/en/ microscope/stream2/ (accessed October 29, 2021).

[177] Sonat E, Özerinç S. Failure behavior of scarf-bonded woven fabric CFRP laminates. Composite Structures 2021;258:113205.

[178] Turon A, Camanho PP, Costa J, Renart J. Accurate simulation of delamination growth under mixed-mode loading using cohesive elements:Composite Structures 2010; 92:1857–64.

[179] Hart-Smith LJ. Bonded-bolted composite joints. Journal of Aircraft 1985; 22:993–1000.

[180] Tomblin J, Seneviratne W, Escobar P, Yoon-Khian Y. Shear Stress-Strain Data for Structural Adhesives. 2002.

[181] Henkel Aero Structural Adhesives Products_TAI0-4-23272.pdf n.d.

[182] Blackman B, Johnsen B, Kinloch A, Teo W s. The Effects of Pre-Bond Moisture on the Fracture Behaviour of Adhesively-Bonded Composite Joints. The Journal of Adhesion 2008; 84:256–76.

[183] Parker BM. The effect of composite prebond moisture on adhesive-bonded CFRP-CFRP joints. Composites 1983; 14:226–32.

[184] Robson JE, Matthews FL, Kinloch AJ. The bonded repair of fibre composites: Effect com of composite moisture content. Composites Science and Technology 1994; 52:235–46.

[185] Charalambides MN, Hardouin R, Kinloch AJ, Matthews FL. Adhesively-bonded repairs to fibre-composite materials I. Experimental. Composites Part A: Applied Science and Manufacturing 1998; 29:1371–81.

[186] Sugiman S, Crocombe AD, Ashcroft I. Experimental and numerical investigation of the static response of environmentally aged adhesively bonded joints. International Journal of Adhesion and Adhesives 2013; 40:224.

[187] Selzer R, Friedrich K. Mechanical properties and failure behaviour of carbon fibre-reinforced polymer composites under the influence of moisture. Composites Part A: Applied Science and Manufacturing 1997; 28:595–604.

[188] Park Y-B, Song M-G, Kim J-J, Kweon J-H, Choi J-H. Strength of carbon/epoxy composite single-lap bonded joints in various environmental conditions. Composite Structures 2010; 92:2173–80.

APPENDICES

A. DCB and ENF Testing

G_{IC} and G_{IIC} values for the FM-300K and HYSOL EA 9396 are based on double cantilever beam (DCB) tests performed according to ASTM D5528-13 [101] and DIN EN 6033[102] and notched flexure tests (ENF) performed according to ASTM D7905/D7905M [103] and DIN EN 6034[104]. It is aimed to simulate the repair process exactly cause fracture toughness may vary with the bonding process (co-bonding or secondary bonding), adhesive thickness, and adherend configuration. Since most conservative and consistent results are obtained from EN tests, only the details of those tests will be covered in the following section.

The base plate, representing the parent structure, consists of hand-laid eight M21/AS4C prepreg plies with a quasi-isotropic lay-up of $[45/0/-45/90]_s$. According to the manufacturer's requirements, panels were cured in an autoclave at 180°C & 7 bar for 9 hours (including the heating and cooling periods). After completing the cure cycle, A MATEC ultrasonic tester (MA, USA) inspected the panels to verify their integrity using the Automatic Ultrasonics Through Transmission Method (AUTT). Then a sawing machine cut the panels into specimens of 250 mm length and 25 mm width. The thickness of the panels is measured as 2.5 mm. Before laying down the repair section, an insert (release film with a thickness of 0.06 mm) is inserted at a distance of 25 mm from one end to create an initial crack. The remaining bonding surfaces are sanded with 120 grit sandpaper and wiped with acetone.

To find the fracture toughness values for FM-300K, eight plies of M21/AS4C prepreg with a quasi-isotropic lay-up of $[45/0/-45/90]_s$ is co-bonded to the base plate with a 0.2 mm thickness FM-300K film adhesive. Then, according to the manufacturer's cure cycle requirements, the co-bonded structure is vacuum-bagged and cured with a heat blanket; 180°C (+/- 5°C) for 9 hours. The out-of-autoclave cure cycle is selected on purpose to simulate the on-site repair process correctly.

To find the fracture toughness values of the two-part adhesive HYSOL EA 9396, eight plies of Hexforce G0904 dry fabric impregnated with HYSOL EA 9396 (with a 1/3 weight ratio) having a quasi-isotropic lay-up of $[45/0/-45/90]_s$, is co-bonded to the base plate with HYSOL EA 9396. Then, according to the manufacturer's cure cycle requirements, the co-bonded structure is vacuum-bagged and cured with a heat blanket; 66°C (+/- 5°C) for 1 hour. The repair schematic of the specimen is shown in Figure A.1.

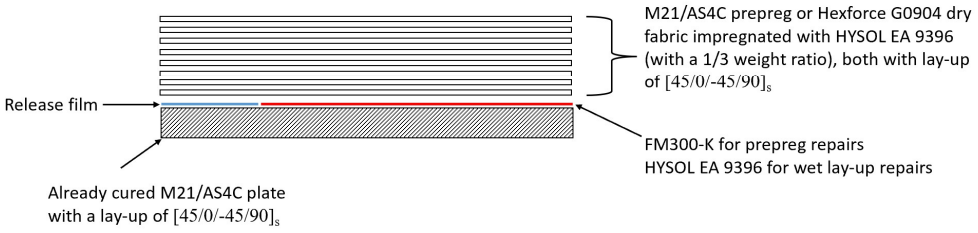

Figure A.1. Schematical representation of the specimen for the DCB and ENF tests.

Double Cantilever Beam (DCB) Testing of the Adhesives

The DCB test specimen for the evaluation of G_{IC} the value was prepared with co-bonding repair prepregs to the pre-cured laminate with either FM300-K or HYSOL EA 9396 and tested per DIN EN 6033 “Determination of interlaminar fracture toughness energy - Mode I - GIC”. The test set-up is shown in Figure A-2.

Two piano hinges mechanically clamped to the specimens. Then the specimens are loaded from the hinges on the opening direction with a test speed of 10 mm/min, and the corresponding crack length and propagation are measured with a ruler and recorded. The test was continued until 100 mm crack length was achieved. For the ease of visualization of the crack tip, a thin white layer of ink was applied to the longitudinal side faces of the specimen. Force-cross head displacement is recorded during the test; the graph is shown in Figure A-3.

Figure A.2. Test set-up for DCB testing

The fracture toughness energy, G_{IC} (J/m^2) is calculated as follows:

$$G_{IC} = \frac{A}{a \times w} \times 10^6 \quad \text{(A.1)}$$

Where;

A (in Joules) is the energy to achieve the total propagated crack length (the area under load-head displacement graph),

a (in mm) is the propagated crack length (final crack length-initial crack length),

w (in mm) is the width of the specimen.

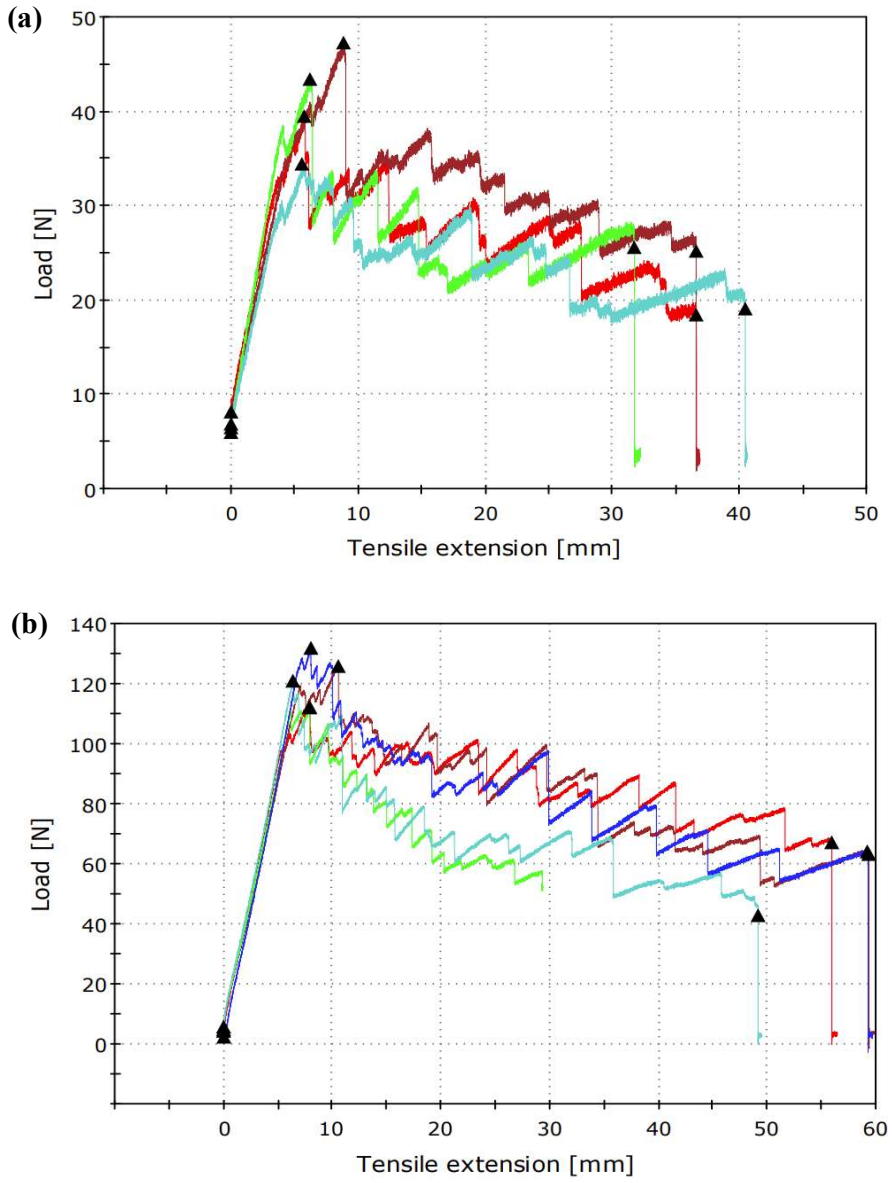

Figure A.3. Force- Crosshead displacement graph of DCB tests, (a) Specimen bonded with HYSOL EA 9396 (b) Specimen bonded with FM 300-K.

End Notched Flexure (ENF) Testing of the Adhesives

The ENF test specimen for the evaluation of G_{IIC} was prepared with co-bonding repair prepregs to the pre-cured laminate with either FM300-K or HYSOL EA 9396 and tested per DIN EN 6034 "Determination of interlaminar fracture toughness energy - Mode II - GIIC. The test set-up is shown in Figure A.4

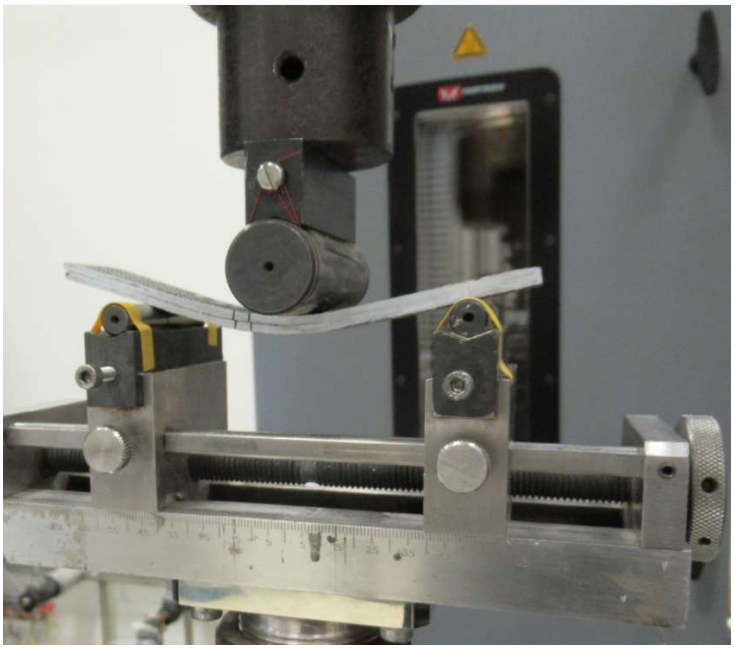

Figure A.4. Test set-up for ENF testing

The test is performed with the remaining portions of the G_{IC} specimen where the initial crack has been introduced. 40 mm pre-cracked specimens having a total length of 120 mm are used for the testing. As shown in Figure A.4, a perpendicular load is applied on the middle of the specimen by a roller (having a diameter of 25 mm and made of steel) with a speed of 1 mm/min. The span is selected to be as 100 mm as the testing specification suggests. The support rollers (having a diameter of 10 mm and made of steel) are located 50 mm apart from the loading support.

The critical load at debond onset is recorded during the test, and part is unloaded as soon as a small drop confirms the crack propagation. In addition, force-cross head displacement is recorded during the test; the graphs for both tests are shown in Figure A-5.

The fracture toughness energy, G_{IIC} (J/m^2) is calculated as follows:

$$G_{IIC} = \frac{9 \times P \times a^2 \times d \times 1000}{2 \times w\left(\frac{1}{4}L^3 + 3a^3\right)} \times 10^6 \qquad 7(A.2)$$

Where;

P (in N) is the critical load to start the crack,

an (in mm) is the initial crack length,

d (mm) is the crosshead displacement at crack delamination onset,

w (in mm) is the width of the specimen,

L (in mm) is the span length.

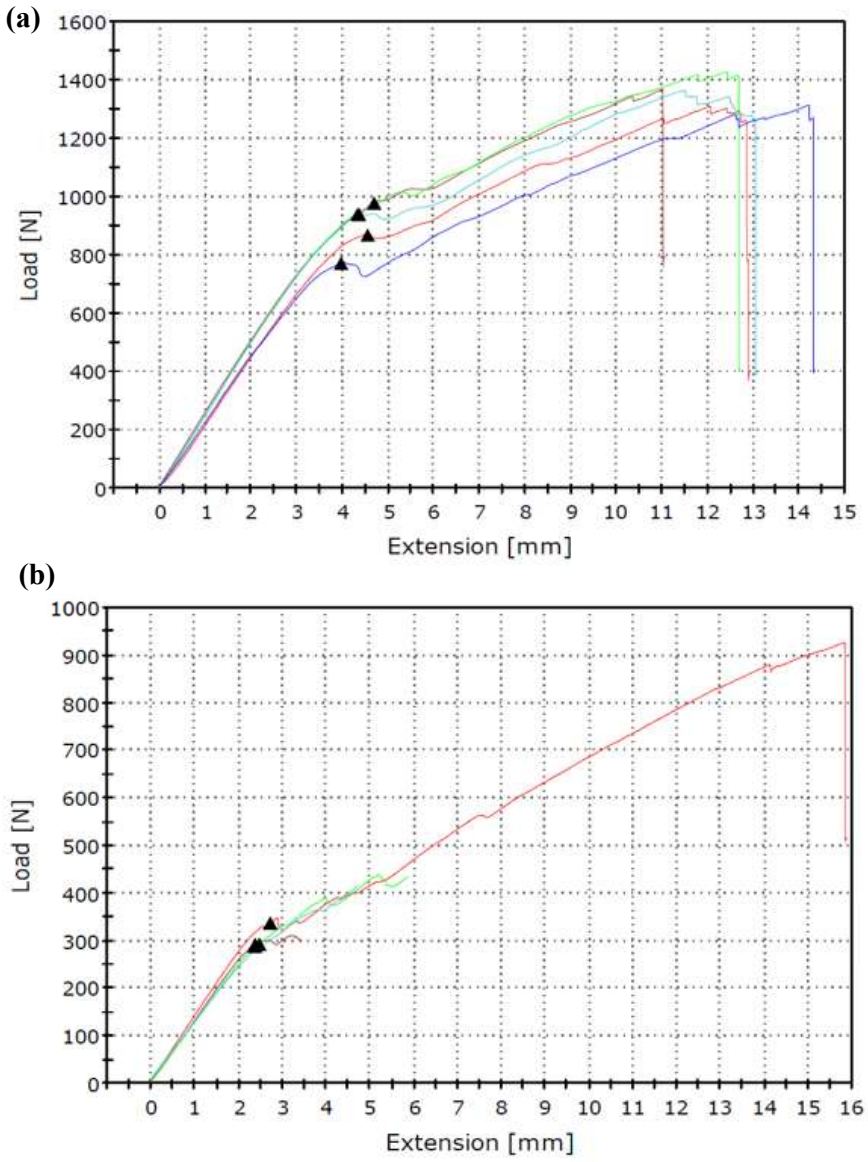

Figure A.5. Force- Crosshead displacement graph of ENF test. (a) Specimen bonded with HYSOL EA 9396 (b) Specimen bonded with FM 300-K.

B. USDFLD Code

```
C ************************************************************
C ************************************************************
C USDFLD FOR  THE DAMAGE MODELLING OF M21/AS4C WOVEN FABRICS
C USDLD_WOVEN FABRICS
C User Material Subroutine
C************************************************************
C Applications:
C 3-D STRESS STATE
C APPLICABLE FOR 3-D SOLID ELEMENTS
C DAMAGE INITIATION IS MODELLED WITH HASHIN FAILURE THEOREM
C DAMAGE PROGRESSION IS MODELLED WITH INSTANTANEOUS DEGRADATION MODEL
C WITH A FACTOR OF (α = 10-4)
C ************************************************************
C Author:
C E. Evren Sonat
C
C NOVEMBER, 2021
C Version 1.1
C ************************************************************

      SUBROUTINE USDFLD(FIELD,STATEV,PNEWDT,DIRECT,T,CELENT,TIME,DTIME,
     1 CMNAME,ORNAME,NFIELD,NSTATV,NOEL,NPT,LAYER,KSPT,KSTEP,KINC,
     2 NDI,nshr,coord,jmac,jmtyp,matlayo,laccflg)
C
      INCLUDE 'ABA_PARAM.INC'
C
C MATERIAL AND STRENGTH PARAMETERS OF M21/AS4C
      PARAMETER(XT=930.D0,XC=818.D0,YC=799.D0,YT=940.D0,SL=96.D0,ST1=64.D0,ST2=64.D0)
C
C
      CHARACTER*80 CMNAME,ORNAME
      CHARACTER*3  FLGRAY(15)
      DIMENSION FIELD(NFIELD),STATEV(NSTATV),DIRECT(3,3),T(3,3),TIME(2),
     * coord(*),jmac(*),jmtyp(*)
      DIMENSION ARRAY(15),JARRAY(15)
C
C INITIALIZE FAILURE FLAGS FROM STATEV.
C FLAG FOR THE FAILURE ON THE WARP DIRECTION ( PARALLEL TO THE LOAD DIRECTION)
       WARPF    = STATEV(1)
C FLAG FOR THE FAILURE ON THE WEFT DIRECTION ( PERPENDICULAR TO THE LOAD DIRECTION)
       WEFTF    = STATEV(2)
C
C GET STRESSES IN 3 DIRECTIONS FROM PREVIOUS INCREMENT
      CALL GETVRM('S',ARRAY,JARRAY,FLGRAY,jrcd,
     $     jmac, jmtyp, matlayo, laccflg)
      S11 = ARRAY(1)
      S22 = ARRAY(2)
      S33=  ARRAY(3)
      S12 = ARRAY(4)
      S13 = ARRAY(5)
      S23=  ARRAY(6)
C
```

```
C ************************************************************
C DAMAGE INITIATION WITH HASHIN FAILURE THEOREM
C ************************************************************
C
C WARP TENSILE/COMPRESSIVE FAILURE ACCORDING TO THE HASHIN FAILURE THEOREM
      IF (WARPF .LT. 1.D0) THEN
         IF (S11 .LT. 0.D0) THEN
           WARPF = (S11/XC)**2
         ELSE
            WARPF = (S11/XT)**2 + (S12/SL)**2 +(S13/ST1)**2
         ENDIF
         STATEV(1) = WARPF
      ENDIF
C
C WEFT TENSILE/COMPRESSIVE FAILURE ACCORDING TO THE HASHIN FAILURE THEOREM
      IF (WEFTF .LT. 1.D0) THEN
         IF (S22 .LT. 0.D0) THEN
            WEFTF = (S22/YC)**2
         ELSE
            WEFTF = (S22/YT)**2 + (S12/SL)**2 +(S23/ST2)**2
         ENDIF
         STATEV(2) = WEFTF
      ENDIF
C
C ************************************************************
C DAMAGE PROGRESSION WITH INSTANTANEOUS DEGRADATION MODEL
C      (DEGRADED PROPERTIES C ARE GIVEN IN ABAQUS)
C ************************************************************

C     FV1: FILL TENSILE/COMPRESSIVE FAILURE
C     FV2: WARP TENSILE/COMPRESSIVE FAILURE

C ************************************************************
```

	FV1	FV2	E1	E2	E3	NU12	NU13	N23	G12	G13	G23
NO FAILURE	0	0	E1	E2	E3	NU12	NU13	N23	G12	G13	G23
FILL DIRECTION FIBER FAILURE	1	0	10^{-4}	E2	E3	10^{-4}	10^{-4}	N23	10^{-4}	10^{-4}	G23
WARP DIRECTION FIBER FAILURE	0	1	E1	10^{-4}	E3	10^{-4}	NU13	10^{-4}	10^{-4}	G13	10^{-4}
TOTAL FAILURE	1	1	10^{-4}	10^{-4}	10^{-4}	10^{-4}	10^{-4}	10^{-4}	10^{-4}	10^{-4}	10^{-4}

```
C ************************************************************
C     UPDATE FIELD VARIABLES
C
      FIELD(1) = 0.D0
      FIELD(2) = 0.D0
      IF (WARPF .GT. 1.D0)  FIELD(1) = 1.D0
      IF (WEFTF .GT. 1.D0)  FIELD(2) = 1.D0
C
      RETURN
      END
```

C. Selective Test Results

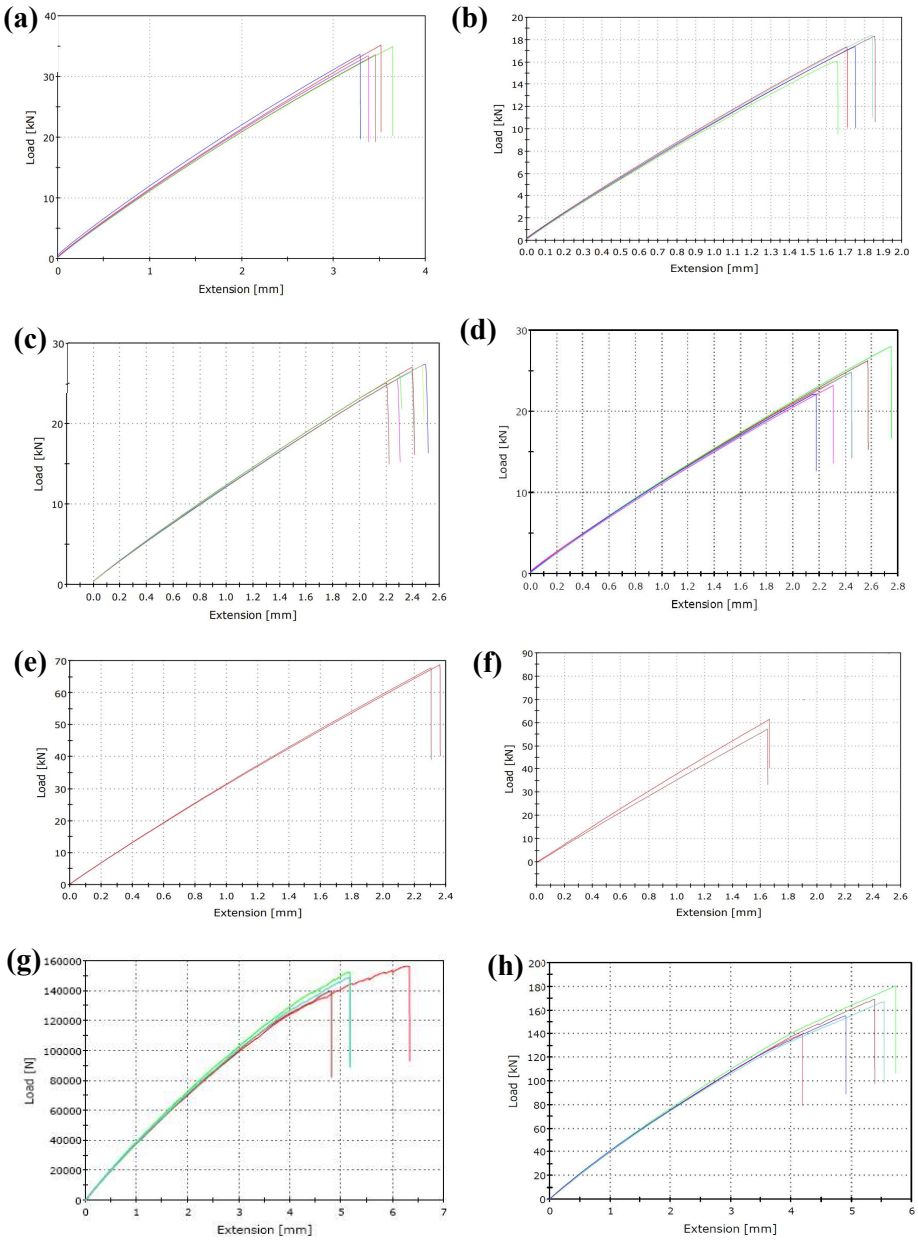

Figure C.1. Force-Displacement curves for (a) intact, (b) 5.7° scarf-bonded specimen, (c)2.8° scarf-bonded specimen, (d) 1.9° scarf-bonded specimen, (e) open hole panel, (f) scarfed panel, (g) 2.8° wet lay-up repaired, (h) 2.8° prepreg repaired

D. Prepreg and Wet lay-up Repair Steps

PREPREG REPAIRS

Surface Preparation: sanding and cleaning

Lay-up of the film adhesive and the repair plies

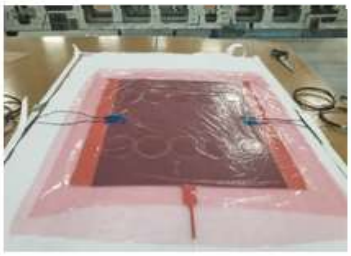

Bagging of the repair

Curing with the HEATCON (heat blanket)

WET LAY-UP REPAIRS


Weighing and preparation of the adhesive

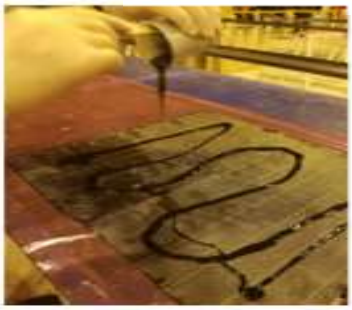
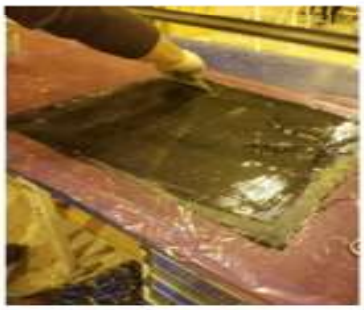

Wetting of the dry fabrics with the adhesive


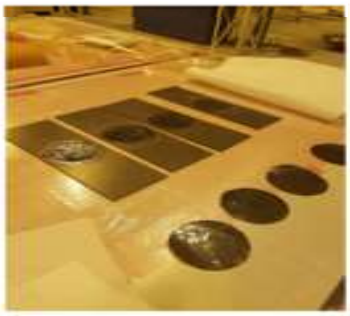

Preparation of the repair plies and lay-up


Bagging and curing with the HEATCON (heat blanket)

CURRICULUM VITAE

Personal Information

Surname, Name: Sonat, E. Evren

Date of Birth: 05.08.1979

Nationality: Turkish Republic

Marital Status: Married

Skills

Composite and Metallic part design, Assembly design, Composite and metallic repair design, Fastener types, applications and selection, Corrosion, sealants & finishes, Non-destructive inspection, Nonconformity handling, Flight line experience, Stress Analysis (Basic, Composite, and Metallic Repairs).

Work Experience

- 05.2021–Present Structural Design Chief Engineer- TAI/ Turkish Aerospace Industries,
- 2008 – 05.2021 MRB Specialist Engineer- TAI / Turkish Aerospace Industries,
- 2001 – 2008 Research Assistant / Instructor – Welding Technology and Non-Destructive Testing Research Center - Middle East Technical University,

Educational Background

2018 – Present Ph.D.- Mechanical Engineering - Middle East Technical University (3.81 /4.0)

2001 – 2004 MS- Mechanical Engineering - Middle East Technical University (3.29 /4.0)

1997 – 2001 BS- Mechanical Engineering - Middle East Technical University (3.04 /4.0)

1990 – 1997 Gazi Anatolian High School

Ms. Thesis

Computerized Test Procedure for Radiographic Examination of Metallic Welded Joints

Ph.D. Thesis

Mechanical Properties of Repaired Carbon Fiber Reinforced Polymer Composites

Conferences and Papers

- "Computerized Test Procedure for Radiographic Examination of Metallic Welded Joints", Proceedings of 6th National Welding Technology Conference, 2007, Pp. 89-94.
- "Effect of Repair Processes on the Mechanical Properties of Composites used in Aerospace Applications", 1st International Workshop on Plasticity, Damage and Fracture of Engineering Materials (IWPDF), 2019, poster presentation
- "Failure behavior of scarf-bonded woven fabric CFRP laminates", Composite Structures 2021; 258:113205.